COMPUTATIONAL DISCOVERY AND DESIGN OF NOVEL SINGLE-LAYER MATERIALS FOR ELECTRONIC AND ENERGY APPLICATIONS

A Dissertation

Presented to the Faculty of the Graduate School

of Cornell University

in Partial Fulfillment of the Requirements for the Degree of

Doctor of Philosophy

by

Houlong Zhuang

January 2014

COMPUTATIONAL DISCOVERY AND DESIGN OF NOVEL SINGLE-LAYER MATERIALS FOR ELECTRONIC AND ENERGY APPLICATIONS

Houlong Zhuang, Ph.D.

Cornell University 2014

The last decade has seen an explosion of interest in two-dimensional materials, which now can be synthesized in either single or a few atomic layer forms. The discovery of novel fabrication methods for creating single-layer materials such as graphene, zinc oxide, silicon carbide, boron nitride, and molybdenum disulfide has opened a new field of materials research with promising applications for energy technologies. Single-layer materials not only represent the ultimate scaling in the vertical direction, but also show a variety of novel and useful electronic, optical, and mechanical properties.

Using a data-mining and first-principles design approach we identify several previously unrecognized families of single-layer materials. We determine their energetic and dynamical stability, study their electronic and optical properties, and determine their suitability for electronic and energy applications using a combination of density-functional calculations with semi-local and hybrid density functionals, the many-body G_0W_0 method, and the Bethe-Salpeter equation. To determine their suitability for photocatalytic water splitting we also determine their solubility in water.

We discover several single-layer materials with promising properties for electronic devices such as for dielectric barriers in graphene field-effect tunneling transistors and for photocatalytic water splitting. Our results provide guidance for experimental synthesis efforts and future searches of materials suitable

for applications in electronic device and energy technologies.

BIOGRAPHICAL SKETCH

Houlong Zhuang was born in Lianjiang, Fuzhou, China. He was admitted into Lianjiang First Middle school and then Hunan University majoring in mechanical engineering and later in materials science and engineering. During his bachelor period, Houlong gained some research experience in performing experiments on aluminum-based alloys. He then moved to the University of Hong Kong for a master study with a recommendation letter written by Alan Mark Russell at the Iowa State University. At HKU, Houlong was co-advised by Dr. Guangping Zheng and Prof. Ai-Kah Soh with the master thesis on simulations of carbon nanotubes. During his master study, Houlong accumulated significant experience on computational simulations. In Hong Kong, Houlong met and married with his lovely wife, Li Cai. After the Master study, Houlong worked as a research assistant for several months, and then came to USA with his wife for the PhD study. Influenced by his advisor, Richard Hennig, Houlong loves doing research and exploring unfamiliar research topics. At Cornell, Houlong also enjoys his family time with his wife and two kids, Garrett and Claire, who were born in 2010 and 2012, respectively.

After obtaining the PhD, Houlong will start a postdoc position and then keep pursuing an academic career.

This thesis is dedicated to my father and grandfather.

ACKNOWLEDGEMENTS

I am truly grateful to my advisor Richard Hennig, for offering me the opportunity to conduct research with him and providing me with valuable guidance. His passion for research was an invaluable inspiration throughout my PhD career. His expert guidance and constant encouragements are essential to make this dissertation possible.

I also thank Darrell Schlom and David Muller for not only being my special committee members but also for teaching me several very useful classes.

I would also like to thank Michelle Johannes, who is visiting professor from the Naval Research Laboratory, for her assistance and guidance of Chapters 9 and 10.

I am grateful to the other graduate students in Prof. Hennig's group, Michael Blonsky, Changju Lee, Kent Liu, Kiran Mathew, Hilda Mera, Benjamin Revard, Arunima Singh, and Will Tipton. I would also like to acknowledge my experimental collaborators at Cornell for many useful and stimulating discussions. They are David Muller, Jiwoong Park, Paul McEuen and their students, Pinshane Huang, Robin Havener, Carlos Ruiz-Vargas, and Arend van der Zande.

Chapters 3 to 8 in this dissertation have been peer-reviewed and published. The comments and suggestions from the anonymous reviewers are greatly appreciated.

Last but most importantly, I would like to thank my family, particularly my wife Li Cai and my two kids, Garrett and Claire, for their endless love and support.

TABLE OF CONTENTS

Biographical Sketch . . . iii
Dedication . . . iv
Acknowledgements . . . v
Table of Contents . . . vi
List of Tables . . . ix
List of Figures . . . xii

1 Introduction 1
1.1 Materials Science Tetrahedron of Single-Layer Materials . . . 1
1.1.1 Structure . . . 2
1.1.2 Properties . . . 5
1.1.3 Processing . . . 6
1.1.4 Performance . . . 8

2 Computational Methods for Characterization of Single-Layer Materials 11

3 Electronic Structures of Single-Layer Boron Pnictides 19
3.1 Abstract . . . 19
3.2 Introduction . . . 19
3.3 Methods . . . 20
3.4 Results . . . 22
3.5 Summary . . . 29

4 Computational Discovery of Single-Layer III-V Materials 30
4.1 Abstract . . . 30
4.2 Introduction . . . 30
4.3 Methods . . . 32
4.4 Results . . . 33
4.4.1 Single-Layer Hexagonal III-V Materials . . . 33
4.4.2 Single-Layer Tetragonal III-V Materials . . . 38
4.4.3 Electronic Structure of Single-Layer III-V Materials . . . 40
4.5 Summary . . . 42

5 Computational Discovery of Single-Layer Oxide Semiconductors 49
5.1 Abstract . . . 49
5.2 Introduction . . . 49
5.3 Methods . . . 51
5.4 Results . . . 52
5.4.1 Structure and Formation Energies . . . 52
5.4.2 Electronic Band Structure . . . 54
5.4.3 Phonon Spectrum and Dynamical Stability . . . 55
5.4.4 Optical Properties . . . 56

5.4.5 Single-Layer Oxides as a Dielectric Barrier 58
5.5 Summary 60

6 Single-Layer Group-III Monochalcogenide Photocatalysts for Water Splitting 62
6.1 Abstract 62
6.2 Introduction 63
6.3 Methods 65
6.4 Results 68
6.4.1 Structural Properties 68
6.4.2 Electronic Properties 69
6.4.3 Photocatalytic Water Splitting 73
6.4.4 Band Edge Tuning by Strain 75
6.4.5 Stability in Water 77
6.5 Summary 78

7 Computational Search for Single-Layer Transition-Metal Dichalcogenide Photocatalysts 83
7.1 Abstract 83
7.2 Introduction 84
7.3 Simulation Methods 85
7.4 Results and Discussion 88
7.4.1 Structure and Stability of Single-Layer MX_2 Compounds . 88
7.4.2 Band Alignment of Single-Layer MX_2 Compounds with Water Redox Potentials 90
7.4.3 Tuning of Band Edge Positions 94
7.4.4 Stability of MX_2 Compounds in Water 96
7.5 Summary 97

8 Theoretical Perspective of Photocatalytic Properties of Single-Layer SnS_2 102
8.1 Abstract 102
8.2 Introduction 102
8.3 Methods 104
8.4 Results 106
8.4.1 Stability 106
8.4.2 Electronic Structures 109
8.4.3 Optical Properties 110
8.4.4 Band Alignments 112
8.5 Summary 116

9 Charge-Density Wave Driven Phase Transitions in Single-Layer MoS_2 117
9.1 Abstract 117
9.2 Introduction 118

9.3 Methods . . . 121
9.4 Results . . . 121
9.5 Summary . . . 129

10 Computational Prediction and Characterization of Single-Layer CrS_2 131
10.1 Abstract . . . 131
10.2 Introduction . . . 131
10.3 Methods . . . 133
10.4 Results . . . 134
10.4.1 Stability . . . 134
10.4.2 Electronic Properties . . . 138
10.4.3 Optical Properties . . . 140
10.4.4 Piezoelectric Properties . . . 144
10.5 Summary . . . 145

11 Outlook 146

A Appendix of Chapter 5 148

B Appendix of Chapter 6 153

C Appendix of Chapter 8 157

D Appendix of Chapter 9 162

Bibliography 168

LIST OF TABLES

3.1 Structural properties of single-layer boron pnictides. The bond length b_0 in Å, cohesive energy E_{coh} in eV/atom, and elastic modulus C in N/m are calculated for the LDA and PBE functional. The cohesive energies are calculated in reference to the spin-polarized B and X atoms. The energy differences ΔE_{tot} between single layered and bulk zinc-blende structures in eV/atom are calculated with the LDA functional. 22

3.2 Electronic properties of single-layer boron pnictides. The band gap E_g in eV are calculated with the local LDA, semilocal PBE, and hybrid HSE06 functionals. The VBOs are calculated with the PBE functional and CBOs are determined by adding the HSE06 band gaps to the VBOs. 24

4.1 Structural parameters and energy differences ΔE of the 2D hexagonal and tetragonal group III-V materials relative to the known 3D crystal structures. The structural parameters include the lattice constants a and the buckling z. 34

4.2 Electronic and phonon properties of the 2D hexagonal group III-V materials. Shown are the band gaps E_g^{HSE} and the electron and hole effective masses m_e^*/m_e and m_h^*/m_e, respectively, obtained from HSE06 calculations, the quasiparticle band gaps from G_0W_0 calculations, the Bader charges Q_{Bader} transferred from the group III to the group V atoms, the Born effective charges Z^*, the macroscopic dielectric constant ϵ_∞, the phonon frequencies ω_{LO} and ω_{TO} at the Γ point, and the frequency splitting $\Delta\omega$. 44

5.1 Properties of single-layer oxides, including formation energies ΔE_{f} relative to the bulk phases in eV/atom, lattice parameters a_0 in Å, Bader charges Q in units of electrons, and the band gap sizes E_{g} in eV and types. HgO reconstructd to a *Pbam* structure, denoted as HgO (*Pbam*) (see Appendix A) 53

6.1 Structural parameters and elastic modulus of single-layer MX and MoS_2 calculated with the PBE and HSE06 functionals. The parameters include the lattice parameter a_0, the M-M bond length $b_{\text{M–X}}$, X-X bond length $b_{\text{X–X}}$ in units of Å, and the X-M-M bond angle $\theta_{\text{X–M–M}}$ in units of degrees. The elastic modulus C is in units of N/m. 79

6.2 band gaps E_{g}, band gap centers E_{BGC}, and band edge positions E_{VBM} and E_{CBM} of single-layer MX obtained from different methods. All energies are in units of eV. Data of single-layer MoS_2 are shown for comparison. 80

7.1 Structural parameters and formation energies E_f of $2H$ single-layer transition-metal dichalcogenides MX_2 calculated with the PBE functional. The structural parameters include lattice constant a_0 (Å), M-X bond length b_{M-X} (Å), X-X bond length b_{X-X} (Å), X-M-X bond angle θ_{X-M-X} (degrees). ΔE refers to the energy difference between the $1T$ and the $2H$ structures. All energies are in units of eV/atom. 98
7.2 Structural parameters and formation energies E_f of $1T$ single-layer transition-metal dichalcogenides MX_2 calculated with the PBE functional. The structural parameters include lattice constant a_0 (Å), M-X bond length b_{M-X} (Å), X-X bond length b_{X-X} (Å), X-M-X bond angle θ_{X-M-X} (degrees). ΔE refers to the energy difference between the $1T$ and the $2H$ structures. All energies are in units of eV/atom. 99
7.3 Bandgaps E_g, bandgap center energies E_{BGC}, and band edge positions E_{CBM} and E_{VBM} of single-layer semiconducting transition-metal dichalcogenides. The bandgaps are calculated with two approaches, with DFT using the PBE functional yielding E_g^{PBE} and the many-body G_0W_0 approximation yielding the quasiparticle bandgaps E_g^{QP}. All energies are in units of eV. 100
7.4 Bandgaps E_g, bandgap center E_{BGC}, and band edge positions E_{CBM} and E_{VBM} of the 3D bulk structures of semiconducting MoS_2, WS_2 and PtS_2. The bandgaps are calculated with two approaches, with DFT using the PBE functional yielding E_g^{PBE} and the many-body G_0W_0 approximation yielding the quasiparticle bandgaps E_g^{QP}. All energies are in units of eV. 101

8.1 Structural parameters and elastic modulus of single-layer and bulk SnS_2. The parameters include the lattice parameter a_0, the Sn-S bond length b_{Sn-S}, S-S bond length b_{S-S} in units of Å, and the Sn-S-Sn bond angle $\theta_{Sn-S-Sn}$ in units of degrees. The elastic modulus C is in units of N/m. 105
8.2 Fundamental indirect and direct band gaps (in eV) of single-layer SnS_2 obtained from three different approaches. Experimental optical band gaps from Ref. [1] are shown for comparison. . . 109

9.1 Structural parameters, energies, and fundamental bandgaps of single-layer MoS_2 with various structures. The parameters a_0 and b_0 for each structure are denoted in Fig.9.1. All energies E_{ref} are with reference to the energy of MoS_2 with the $2H$ structure and are in units of eV/atom. The bandgaps E_g with and without spin-orbit coupling are calculated with the PBE functional. 120

10.1 Structural parameters and formation energies of single-layer CrS_2 in the 2*H* and 1*T* structure. The structural parameters are calculated with the HSE06 functional and the formation energies with the HSE06, PBE, and opt-B88 van der Waals functionals. The structural parameters, in units of Å, include the lattice parameter a_0 and the spacing Δz between the Cr and the S atom layers. The formation energies are in units of eV/atom. 135
10.2 Elastic constants and piezoelectric coefficients of single-layer CrS_2. The elastic constants C_{11} and C_{12} are in units of N/m. The piezoelectric coefficients e_{111} and d_{111} are in units of 10^{-10} C/m and pm/V, respectively. 144

A.1 Crystal structure and energy of various reported structures of HgO. The optimized lattice parameters are given in units of Å and the energy is given relative to the lowest energy structure with space group *Pnma* in units of eV per molecular unit of HgO. 149
A.2 Conduction band minimum and valence band maximums (CBM and VBM) in units of eV) with reference to graphene's Fermi level.150

LIST OF FIGURES

1.1 Materials science tetrahedron symbolizing the interplay of materials structure, properties, processing, and performance. One snapshot is adopted from Ref. [2]. 2
1.2 Structures of single-layer materials with hexagonal Bravais lattices: (a) planar and (b) buckled hexagonal group IV or III-V materials, (c-e) single-layer metal chalcogenides with the number of sublayers ranging from three to five. M denotes the metal sublayers, while X represents the chalcogen sublayers. 3
1.3 Top view and side view of the atomic structures of single-layer (a) SnSe and (b) InP. 5
1.4 Cross-sectional view of the structure of a monolayer MoS_2 field effect transistor. Reprinted with permission from Ref. [3]. Copyright 2011 Nature Publishing Group. 8
1.5 Graphene-based supercapacitor device, (a) schematic diagram and (b) optical image of an coin-shaped graphene-based supercapacitor device. Reprinted with permission from Ref. [4]. Copyright 2009 American Chemical Society. 10

2.1 Computational approach for the discovery, characterization, and design of novel single-layer materials. 12
2.2 Atomic structure of bulk ZnO and the corresponding single-layer (111) surface. 13

3.1 Band structures of (a) BN, (b) BP, (c) BAs, (d) BSb and (e) graphene. These band structures are in similar shapes, and one notable difference is the energy gap that occurs in BX at the K point. 21
3.2 Change of the band gap with strain for (a) BN and (b) BP, BAs and BSb layered structures. 26
3.3 Band structure of BSb near the K point at strains of (a) -7% (b) 0% and (c) 7%. 27
3.4 (a) Band alignment of the single-layer boron pnictides and graphene calculated from (b) the local density of states of graphene (left) and BN (right) layers in a supercell heterostructure. 28

4.1 Energy differences ΔE between the 2D and bulk structures as a function of lattice parameter for 2D group III-V materials with (a) hexagonal and (b) tetragonal structure. The diamond and square symbols denote the energy differences with respect to the hexagonal wurtzite and cubic zincblende structure, respectively. Black indicates that the hexagonal structure is planar, while red means that the hexagonal structure is buckled. 35

4.2 (a) Energy difference between hexagonal planar and hexagonal buckled geometries as a function of Q^2/a^2. (b) Energy difference between the hexagonal and tetragonal geometries as a function of Q^2/a^2. 43
4.3 Phonon spectra of hexagonal (black labels) and tetragonal (red labels) 2D group III-V materials. The insets show the sketches of the first Brillouin Zones of the 2D hexagonal and tetragonal structures. 45
4.4 Band structures of hexagonal (black labels) and tetragonal (red labels) 2D group III-V materials calculated with the HSE06 hybrid functional. 46
4.5 The relationship between fundamental band gaps and lattice constants of the semiconducting 2D group III-V materials. A sketch of the light spectrum is overlaid to aid visualization of the band gap size. The center of the two concentric circles or squares determines the band gap size of hexagonal and tetragonal structures, respectively. Additionally, the inner and outer radii or side length represent the electron and hole effective mass, respectively. The data of single-layer MoS_2 from Ref. [5] is shown for comparison 47
4.6 Total density of states (DOS) and projected DOS of (a) hexagonal and (b) tetragonal GaSb. 48

5.1 (a) Band structure of single-layer CdO calculated with the HSE06 functional. The valence-band maximum is set to zero. (b) Phonon spectrum of single-layer CdO. The lack of imaginary modes confirms the dynamical stability. The band structures and phonon spectra of single-layer BeO, MgO, ZnO, and HgO are shown in Appendix A. 54
5.2 Optical properties of single-layer CdO, (a) imaginary dielectric constant ϵ_2 and (b) optical absorbance spectrum A(ω), both calculated using the PBE functional. 57
5.3 (a) An illustration of graphene/CdO/graphene heterostructure. (b) Band alignment of single-layer oxides and BN with reference to the Fermi level of graphene, which is set to zero. 59

6.1 (a) Top and side views of the single-layer MX structure. (b) Illustration of photocatalytic water splitting. The band edge positions of a photocatalyst must be aligned with reference to the redox potentials for water splitting. 64
6.2 Formation energies of single-layer MX and MoS_2. The low formation energies indicate that the MX, similar to MoS_2, could be synthesized by mechanical exfoliation. 67

6.3 Band structures of single-layer MX calculated with the HSE06 functional. The valence band maximum is set to zero. The inset illustrates the first Brillouin zone of the single-layer hexagonal MX structures. 70
6.4 (a) Total and (b) projected density of states of GaSe. 71
6.5 Band edge positions of single-layer MX relative to the vacuum level at zero strain calculated with the HSE06 functional. The band edge positions of single-layer MoS_2 and the standard redox potentials for water splitting at pH = 0 are shown for comparison. 73
6.6 Optical absorbance spectrum $A(\omega)$ of single-layer GaSe at the strains of 0% and 4%. $A(\omega)$ is calculated using the PBE functional followed by a rigid energy shift to take into account of the band gap underestimation of the PBE functional. 74
6.7 Strain effects on band edge positions of single-layer (a) GaX and (b) InX. Following the convention, positive strains indicate tension while negative strains denote compression. The discontinuity in slope of the band edges with strain for some MX arises from changes of the band edge positions to different k points. . . 81
6.8 Stability of single-layer GaX and InX in water. (a) Experimental solubility of three silver halides and two sulfides as a function of calculated and experimental enthalpy of solvation ΔH. (b) Predicted enthalpy of solvation ΔH of the single-layer monochalcogenides. The high solvation enthalpies indicate that the single-layer monochalcogenides are insoluble in water. 82

7.1 Two crystal structures of single-layer MX_2. (a) $2H$ structure and (b) $1T$ structure. 87
7.2 Formation energies of single-layer transition-metal dichalcogenides. The similarity of the formation energies for the MX_2 to the value for MoS_2, indicated by the red dashed line, suggests the ease of mechanical exfoliation of the single-layer materials from bulk crystals. 89
7.3 Band structures of single-layer WS_2, ZrS_2, PtS_2, and $PtTe_2$ calculated with the PBE functional (solid blue lines) and the G_0W_0 method (red circles). The valence band maximum is set to zero. . 90
7.4 Band edge positions of single-layer transition-metal dichalcogenides relative to the vacuum level. The redox potentials of water splitting at pH = 0 (red dotted line) and pH = 7 (green dashed line) are shown for comparison. 92
7.5 Density of states of (a) bulk PtS_2 calculated with the G_0W_0 method and the HSE06 functional and (b) single-layer PtS_2 obtained from the G_0W_0 method. 94
7.6 G_0W_0 band structures of single-layer $ZrSe_2$ at the strains of 0% (red) and 4% (blue). Valence band maximum is set to zero. 95

7.7 Solvation enthalpies of single-layer MoS_2, WS_2, PtS_2, and $PtSe_2$. The enthalpy of insoluble HgS is also shown for comparison. . . 96

8.1 Crystal structure of single-layer SnS_2. Each sulfur atoms (red ball) has three nearest neighboring tin atoms, while each tin atom (blue ball) has six nearest neighboring sulfur atoms. 104
8.2 Phonon spectrum of single-layer SnS_2. The Raman-active modes at Γ are denoted as A_{1g} and the E_g, respectively. 107
8.3 Band structure of single-layer SnS_2 calculated with the PBE (red dashed line) and HSE06 (blue solid line) functionals and the G_0W_0 method (black dots). 108
8.4 Total and projected density of states of single-layer SnS_2. 111
8.5 Imaginary part of the permittivity calculated with the BSE and RPA scheme. The inset shows a close-up of the first three BSE peaks. To compensate for the band gap underestimation using the PBE functional in the RPA calculation, we have shifted the spectra by 1.0 eV, which is the difference between the HSE06 and PBE band gaps. 113
8.6 Energy diagram of single-layer SnS_2 with respect to normal hydrogen electrode level in electrolyte of pH = 6.6. The CBM and VBM energy levels are obtained from the HSE06 band gap center in combination with the band gaps from three different approaches including the PBE functional (1.57 eV) and the HSE06 functional (2.52 eV), and the G_0W_0 method (2.88 eV). 115

9.1 Atomic structures of single-layer MoS_2.The unit cells are enclosed by dashed lines. Molybdenum and sulfur atoms are represented by blue and red balls, respectively. 119
9.2 Energy difference between the $1T$ and the $2H$ structure as a function of reaction coordinates and number of doped electrons per unit cell. 123
9.3 (a) Band structure and (b) Fermi surface of $1T$ single-layer MoS_2. Phonon spectra of intrinsic and n-type doped $1T$ MoS_2 are shown in panel (c), while the panel (d) shows the phonon spectrum of p-type doped $1T$ MoS_2. The real part of the electric susceptibility of intrinsic and p-type doped $1T$ MoS_2 are shown in panels (e) and (f), respectively. 124
9.4 (a)-(c) Band structures of $1T$ single-layer MoS_2 with three reconstructed CDW structures. The corresponding band structures with spin-orbit coupling are shown in panels (d)-(e). Valence band maximum is set to zero. Common notations for the high symmetry k points are used. 126
9.5 Local density of states of one unit of $2H$ single-layer MoS_2 which is far away from the interface of the $2H/1T'$ heterostructure. . . . 130

10.1 Ball-and-stick model of single-layer CrS_2 with the 2H (top) and 1T (bottom) structures. Chromium and sulfur are represented by the blue and yellow balls, respectively. 132
10.2 Phonon spectrum of single-layer 2H CrS_2. 137
10.3 Band structures of single-layer CrS_2 for the (a) 2H and (b) 1T structure calculated with the HSE06 functional. 139
10.4 Total and projected electronic density of states of single-layer CrS_2 calculated with the HSE06 functional. 139
10.5 Degree of circular optical polarization $\eta(\mathbf{k})$ of single-layer CrS_2. . 142
10.6 Optical absorbance for unstrained and compressively strained single-layer CrS_2 calculated using the BSE scheme. 142

A.1 Band structures of single-layer BeO, MgO, CaO, ZnO, and HgO. 148
A.2 Phonon spectra of single-layer BeO, MgO, CaO, ZnO, and HgO. 151
A.3 Reconstructed structure of single-layer HgO. The structure has space group *Pbam* (55) with 8 atoms in the unit cell, and the structural parameters are a = 7.02 Å, b = 6.62 Å, r = 2.03 Å and θ = 109.2°. 152

B.1 Average electrostatic potential (red curve) of single-layer GaSe along the direction perpendicular to the layer calculated with the HSE06 functional. The vacuum energy level is set to zero. The conduction band minimum and valence band maximum (CBM and VBM) are shown, along with the band gap center (BGC) energy. All these three energy levels are with reference to the vacuum level. 154
B.2 Band alignments of single-layer MX and MoS_2 with reference to water's redox potential calculated using the G_0W_0 approximation. 155
B.3 Band structures of single-layer GaSe at the strains of −4% and +4%.156

D.1 Band structures of single-layer MoS_2 with the 2H structure calculated (a) with and (b) without the spin-orbit coupling. 163
D.2 Density of states of single-layer MoS_2 with the 1T structure. . . . 164
D.3 Phonon spectrum of single-layer MoS_2 with the 2H structure. . . 164
D.4 Total density of states of single-layer MoS_2 with different reconstructed structures. 165
D.5 The imaginary part of susceptibility of 1T single-layer MoS_2. . . 166
D.6 Top view and side view of the 2H/1T' heterostructure after geometry optimizations. Rectangular cells of 2H and 1T' structures are illustrated by enclosed dashed lines. 167

CHAPTER 1

INTRODUCTION

1.1 Materials Science Tetrahedron of Single-Layer Materials

In this chapter, we use the concept of the materials science tetrahedron (MST) to structure our review of the single-layer materials. The MST shown in Fig. 1.1 illustrated the four interdependent aspects of materials: structure, properties, processing, and performance that forming the basis of materials science research. As such the MST provides an important tool that helps our understanding and design of materials [6]. A traditional materials science tool, the MST has in fact been extensively applied to engineering single-layer materials over the last decade, although the terminology is rarely used in the literature.

We start out with a brief overview of the structure, properties, processing, and performance of single-layer materials focusing on the experimental results. Since there have been several reviews of the experimental aspects of single-layer materials [7, 8, 9, 10, 11, 12]. We provide in the next chapter a theoretical perspective. The whole review focuses on the contribution computational methods provides for the discovery, characterization, and design of single-layer materials. In particular, we describe general procedure to efficiently search for novel single-layer materials with useful properties for applications in electronic devices and energy technologies.

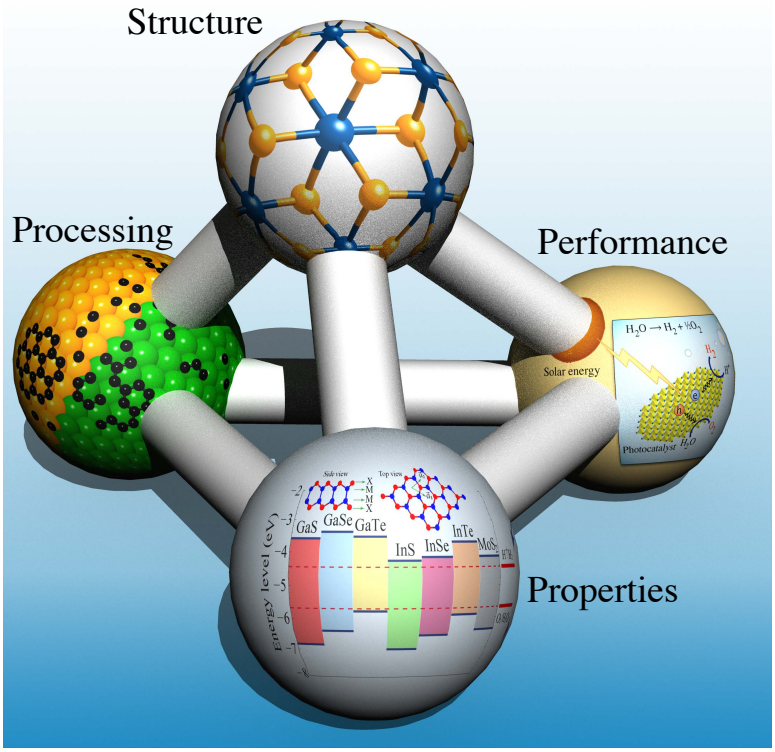

Figure 1.1: Materials science tetrahedron symbolizing the interplay of materials structure, properties, processing, and performance. One snapshot is adopted from Ref. [2].

1.1.1 Structure

With a wealth of attractive properties, single-layer materials are generally defined as individual sheets of atomic-scale thickness that are either extracted from bulk materials such as graphite, boron nitride and transition-metal dichalcogenides or directly synthesized in single-layer form using chemical-vapor deposition or molecular-beam epitaxy. Most single-layer materials occur in structures with a hexagonal Bravais lattice. Figure 1.2 shows several common single-layer hexagonal structures, which can be further categorized based on the number of sublayers in the structure. Single-layer graphene [13], BN [14], and ZnO [15] shown in Fig. 1.2(a) have only one sublayer, while silicene, buckled

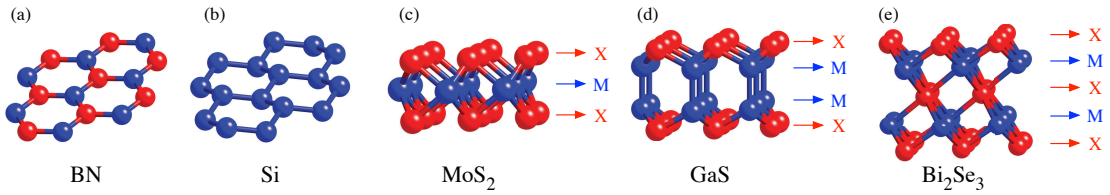

Figure 1.2: Structures of single-layer materials with hexagonal Bravais lattices: (a) planar and (b) buckled hexagonal group IV or III-V materials, (c-e) single-layer metal chalcogenides with the number of sublayers ranging from three to five. M denotes the metal sublayers, while X represents the chalcogen sublayers.

sheets of silicon [16], can be regarded as consisting of two sublayers as shown in Fig. 1.2(b). Single-layer metal chalcogenide (M-X) compounds display structures with a range of sublayers. Figures 1.2(c)-(e) illustrate structures of several typical M-X compounds with their number of sublayers ranging from three to five.

Several single-layer materials occur in less well-known structures with square Bravais lattices. The examples include single-layer SnSe and FeSe, which have been recently synthesized [17, 18] and single-layer group III-V materials, which have recently been predicted [19]. Figure 1.3 illustrates the atomic structure of single-layer SnSe and InP.

Due to their two-dimensional nature, single-layer materials exhibit a modified vibrational mode in their phonon spectra that displays a different dispersion relation than in 3D materials. Acoustic phonons with an out of plane atomic displacements, also known as ZA or flexural phonons, have a quadratic dispersion relationship near the zone center Γ. The flexural phonon mode is responsible for many of the unusual thermal and structural properties of graphene and other single-layer materials. For example, the presence of these low-energy

flexural phonons leads to the occurrence of dynamic and static ripples of single-layer materials at finite temperatures and under small strains [20, 21]. Intrinsic ripples have extensively been studied for the single-layer materials graphene and MoS_2 [22, 23].

Like any material, single-layer materials exhibit microstructures with defects occurring either thermodynamically or due to processing [24, 25, 26]. Similarly to 3D materials, the presence of defects can be either detrimental for the materials' properties or can be used to tune and enhance them. Due to their two-dimensional nature, the classification of defects in 3D materials, needs to be modified for single-layer materials and the defects are categorized into (i) point defects including vacancies, substitutions, and dopant atoms; (ii) line defects such as grain boundaries, interface boundaries, and edges in, e.g., nanoflakes and nanoribbons; and (iii) area defects like voids.

Single-layer materials are dominated by their intrinsic large surface area. As a result, defects are interacting with the surface environment rather than with the bulk environment as in 3D materials. Among microstructural defects, grain boundaries are commonly observed in experimental samples grown by chemical-vapor deposition and molecular-beam epitaxy techniques [24, 25]. Unlike usually undesirable grain boundary defects, introduction of point defects for doping and functionalization of single-layer materials by adsorbing atoms or molecules on the surface provides an effective strategy to tailor various properties of single-layer materials [26]. Although dislocations in single-layer materials such as graphene have been theoretically predicted [27] and experimentally confirmed [28], single-layer materials are not known to plastically deform, instead strain usually leads to brittle failure [29].

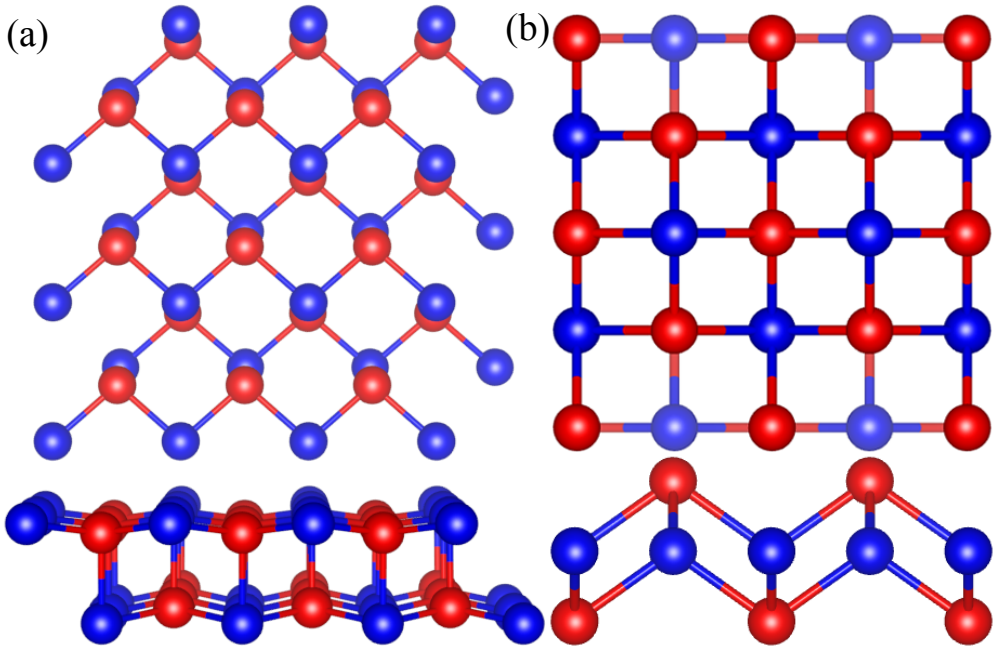

Figure 1.3: Top view and side view of the atomic structures of single-layer (a) SnSe and (b) InP.

1.1.2 Properties

Properties of single-layer materials are generally different from their bulk counterparts due to reduced dimension and decreased symmetry. For example, graphene is the strongest material in the world [30], while graphite is brittle. In addition, electrons in graphene behave like massless Dirac particles and exhibit remarkably high mobilities [31].

Attractive electrical and optical properties are the two main reasons that single-layer materials receive so intense attention. Important parameters of these properties are bandgaps and optical absorption. Many of the known single-layer materials possess bandgaps lying within the range of visible light, which is extremely beneficial for electronic devices and energy-conversion applications. For example, single-layers transition metal dichalcogenides MX_2 (M

= Mo, W; X = S, Se) exhibit direct bandgaps ranging from 1.5 to 2.0 eV [32], wider than the bandgaps of bulk MX_2 due to the quantum confinement effect. Additionally, because of the two-dimensional nature, the density of states of single-layer materials, e.g., MoS_2 are dominated by van Hove singularities, leading to a significant increase in the joint density of states and consequently enhanced optical absorption [33].

In addition to the electrical and optical properties, single-layer materials such as graphene exhibits remarkable thermal conductivity. For example, the experimental thermal conductivity of graphene at room temperature can reach as high as 5300 W/mK [34].

Furthermore, recent studies have shown that single-layer transition-metal dichalcogenides MX_2 like $MoSe_2$ possess sizable piezoelectric coefficients comparable to bulk materials including GaN and AlN with the wurtzite structure [35]. Interestingly, such a piezoelectric coupling effect is absent in the bulk counterparts of MX_2 due to the existence of inversion symmetry.

Finally, single-layer materials could also be promising catalysts. For instance, using single-layer SnS_2 as a photocatalyst leads to a high photocurrent density partly because of the rapid carrier transport in the 2D system [36].

1.1.3 Processing

Over the last decade, a variety of methods have been developed to obtain single-layer materials [37]. Typical methods include mechanical exfoliation, chemical vapor deposition (CVD), liquid exfoliation, and molecular beam epitaxy

(MBE) [38, 39, 40, 18].

The pioneering work of preparing single-layer graphene sheets employed the mechanical exfoliation method [38], in which scotch tape is used to cleave bulk materials with layered structures materials into single-layer sheets. As this method preserves the quality of the bulk material, it typically leads to high-quality sheets with few defects. As such the method is well suited for research purposes. However, one fundamental limit of the mechanical exfoliation technique is its scalability for large scale production [37]. Mechanical exfoliation takes advantage of the presence of weak van der Waals interlayer interactions and can be applied to convert many layered materials such as MoS_2 [38], BN [38], WSe_2 [41], and TaS_2 [41] into single-layer form.

The CVD method involves the vaporization of gaseous reactants and subsequent reactions of the gas molecules to form a thin film on various substrates. The method has been widely used to synthesize large-area single-layer materials such as graphene, BN, and MoS_2 sheets [39]. Common substrates for depositing these single-layer materials are transition metals such as Cu and Ni and thermal oxide on silicon. The CVD method has the advantage of scalability, however, single-layer materials synthesized using CVD typically contain higher densities of defects such as impurities and grain boundaries, compared to mechanical exfoliation [25].

In liquid exfoliation the exfoliation process takes place in a liquid environment through ion intercalation, ion exchange, or sonication techniques [40]. Due to its versatility and scalability, liquid exfoliation has become an important method to exfoliate layered materials characterized by weak interlayer van der Waals interactions. For example, single-layer bismuth selenide Bi_2Se_3 has

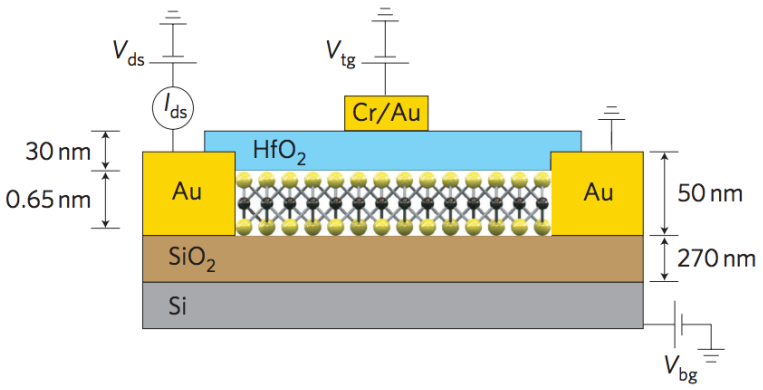

Figure 1.4: Cross-sectional view of the structure of a monolayer MoS_2 field effect transistor. Reprinted with permission from Ref. [3]. Copyright 2011 Nature Publishing Group.

been exfoliated via lithium intercalation [42]. A useful table of families of layered compounds that can be potentially liquid exfoliated into single-layer sheets is provided in Ref. [40].

MBE represents an alternative platform for synthesis of single-layer materials that can produce high-quality films. The elemental components, which make up a single-layer material can be deposited from either thermal or gaseous sources. Refractory elements, such as Mo, are typically obtained by electron-beam evaporation from an assembly that occupies a furnace port. Examples of single-layer materials that have recently been grown using MBE include superconducting single-layer FeSe on $SrTiO_3$ [18], and graphene on SiC [43].

1.1.4 Performance

The remarkable performance of single-layer materials is highlighted by many demonstrated applications, including graphene-based tunneling transistors with large on/off ratio [44], heterostructure-based photovoltaic devices with

high external quantum efficiency [33], and single-layer SnS_2 photocatalyst with excellent visible-light conversion efficiency [45]. These examples can be categorized into electronic devices or energy related applications. Here we describe two additional examples from both categories in some detail.

Figure 1.4 illustrates a field-effect transistor (FET) based on single-layer MoS_2 [3]. In this device, single-layer MoS_2 with a thickness about 6.5 Å deposited on a doped SiO_2 thin film functions as the channel material. With the presence of a high-k dielectric, HfO_2, the reported mobility of single-layer MoS_2 at room temperature can reach more than 200 $cm^2V^{-1}s^{-1}$. Additionally, the current on/off switching ratio can be as high as 1×10^8. Note, however, that a recent study claims that such high carrier mobilities in single-layer MoS_2 are merely experimental artefacts caused by ill-defined capacitance, leading to a drastic overestimate of the carrier mobilities [46]. In combination with its excellent mechanical properties, single-layer MoS_2 also provides promise for flexible electronics applications [47].

Supercapacitors are electrochemical devices that can rapidly and reversibly store and release electrical energy [48]. Graphene with its large specific surface area, excellent conductivity, and stability, is an ideal material for supercapacitor electrodes [11]. Figure 1.5 depicts the schematic of a supercapacitor device based on graphene [4]. These supercapacitors exhibit maximum specific capacitances of more than $2{\times}10^6$ F/kg at a power and energy densities of 10 kW/kg and 28.5 W h/kg, respectively. Moreover, about 90% of the initial capacitance is maintained even after 1200 cycles, indicating good cycle lifetimes [4].

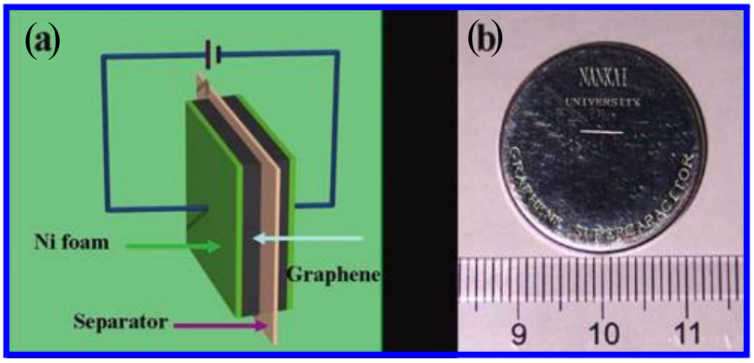

Figure 1.5: Graphene-based supercapacitor device, (a) schematic diagram and (b) optical image of an coin-shaped graphene-based supercapacitor device. Reprinted with permission from Ref. [4]. Copyright 2009 American Chemical Society.

CHAPTER 2

COMPUTATIONAL METHODS FOR CHARACTERIZATION OF SINGLE-LAYER MATERIALS

Materials characterization, often located in the center of the MST, involves using experimental and theoretical tools to analyze the four components of MST. Experimentally, various microscope techniques have been applied to characterize single-layer materials [8]. For example, atomic force microscopy (AFM) is frequently used to determine the thickness of a single-layer material and dark-field transmission electron microscopy (TEM) has been utilized to determine grain boundary angles of polycrystalline graphene sheets [25]. This chapter, instead of reviewing such experimental tools, emphasizes the roles of computational tools, particularly, the ones based on density-functional theory (DFT), in the discovery, characterization, and design of single-layer materials. Figure 2.1 illustrates how the computational tools connect with the four components of the MST.

Structure. The starting point of any DFT calculation is the atomic structure. For single-layer materials with experimentally-known structures, computational characterizations are straightforward. For hypothetical single-layer materials, two common strategies can be followed. The first strategy starts with the three-dimensional structure of a candidate material selected from the International Crystallographic Structural Database (ICSD), such as for example the zincblende and wurtzite structures [49]. The single-layer structure is then assumed to be a layer cut out of the three-dimensional structure, such as a single (111) or (0001) layer. Figure 2.2 illustrates as an example the atomic structure of cubic ZnO and a single (111) layer. This approach can provide a reasonable

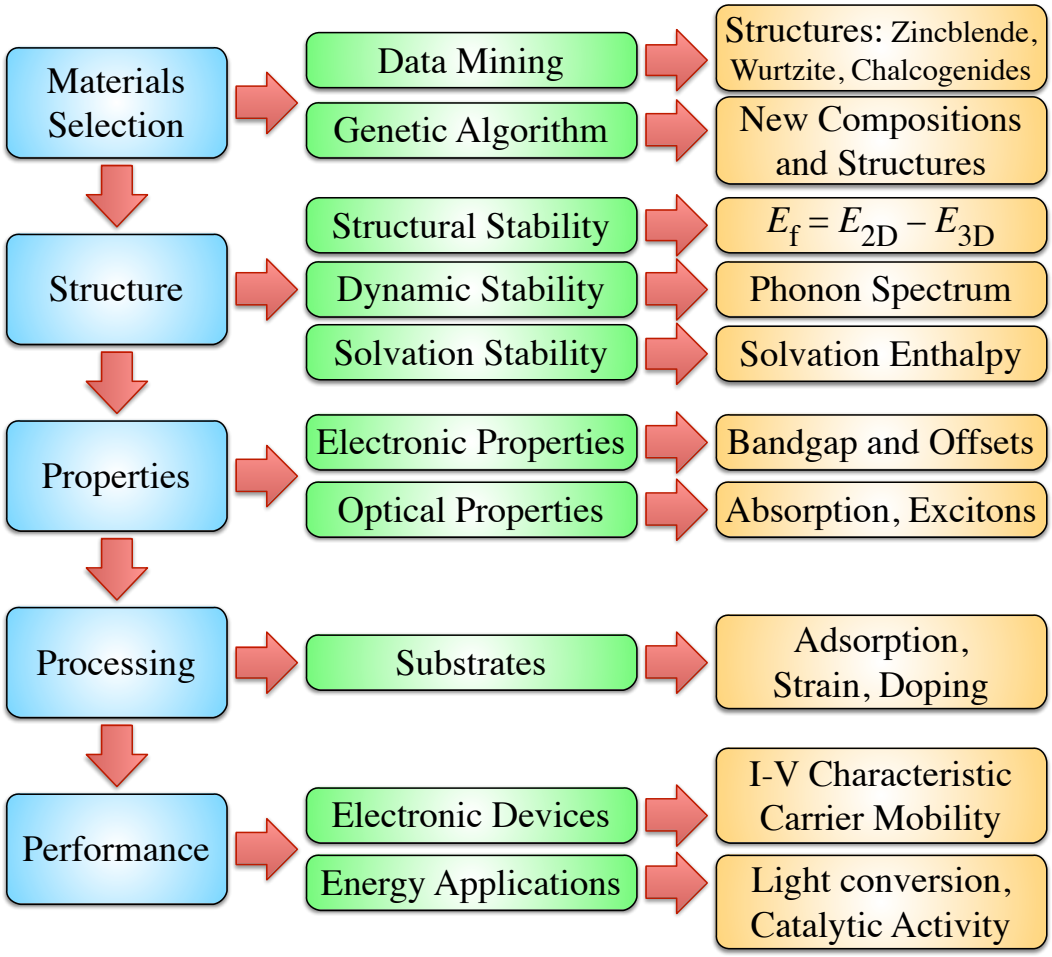

Figure 2.1: Computational approach for the discovery, characterization, and design of novel single-layer materials.

guess for the atomic structure of an unknown single-layer material. Relaxations of this structure with DFT will lead to a hypothetical ground-state structure.

The second approach systematically explores the periodic table and exploits chemical similarities of elements within a group in the periodic table [50, 51]. Replacing one element in an existing single-layer material with another one of the same group or of similar chemistry provides a useful guess for a novel single-layer material. This method has successfully predicted silicene and germanene [52].

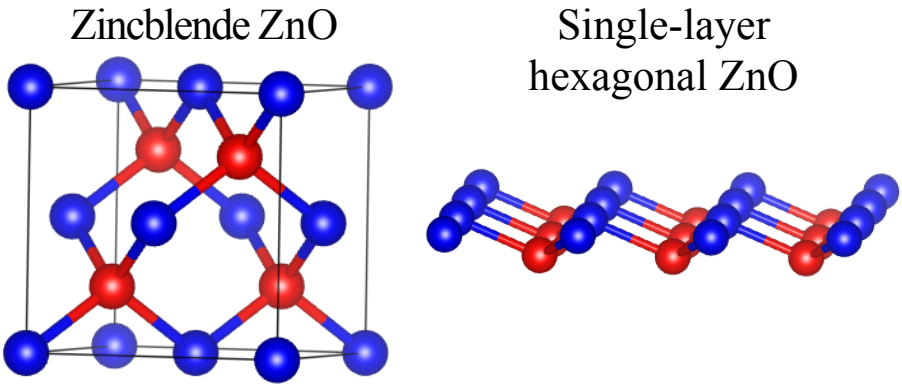

Figure 2.2: Atomic structure of bulk ZnO and the corresponding single-layer (111) surface.

Energetic stability. Once a candidate single-layer structures has been identified, its energetic and dynamical stability need to be evaluated. In general, there is an energy cost to synthesize single-layer materials from their three-dimensional bulk counterparts. This energy cost is given by the formation energy, $E_f = E_{2D}/N_{2D} - E_{3D}/N_{3D}$, where E_{2D} and E_{3D} are the energies of single-layer and bulk structures, respectively, and N_{2D} and N_{3D} denote the number of atoms in the corresponding unit cells. Note, that in some cases, a thermodynamically stable bulk compounds with the same composition as the single-layer material may not exist and the corresponding bulk energy is given by the mixture of competing phases [53].

A low formation energy, E_f indicates that the candidate single-layer material is metastable. Using this definition, we have identified several single-layer hexagonal group III-V materials with formation energies ranging from 0.38 to 0.52 eV/atom, and lying between the formation energies of single-layer ZnO (0.19 eV/atom) and silicene (0.76 eV/atom) [54, 55], both of which have been successfully synthesized [15, 16]. In addition, we found that most transition-metal dichalcogenides exhibit formation energies below 0.15 eV/atom, indicat-

ing the ease to mechanically cleave a sheet of single-layer MX_2 from bulk crystals [56].

Dynamic stability. In addition to determine the energetic stability, it is important to ensure that the candidate single-layer structure is at a local minimum of the potential energy surface rather than at a saddle point. In other words, the phonon modes must be real. Two methods are commonly used to calculate phonon spectra. One is based on density functional perturbation theory [57] and the other one is so-called force constant method. The former method, implemented in the Quantum Espresso package [58], is more efficient to obtain the phonon frequencies at arbitrary points in the Brillouin zone than the latter one, implemented in VASP [59], where a supercell and Fourier interpolation is used to obtain the full phonon dispersion.

As an example, in our work on the single-layer III-V materials we found that a few of the hexagonal III-V materials such as InP exhibit a dynamic instability reflected in imaginary phonon modes. We find that the hexagonal structure reconstruct to an unexpected low-energy tetragonal structure, which is illustrated in Fig. 1.3(b) [19]. Interestingly, this tetragonal structure is similar to that of single-layer FeSe, which is a high-temperature superconductor [18].

Solution stability. For the applications of single-layer materials in liquid environments, such as a photocatalyst, it is critical to consider the stability of these materials in the solution environment. Namely for photocatalysts, the candidate single-layer materials must be insoluble in water. Taking advantage of the fact that the solubility decreases exponentially with increasing solvation enthalpy, solubility can be quantitatively estimated from the calculated enthalpy of solvation. In Ref. [2], we describe a method of combining DFT calculations

with VASP and Gaussian09 [60] to efficiently calculate the solvation enthalpy. In short, we use VASP to calculate the cohesive energy of a compound, and Gaussian09 to obtain the hydration enthalpy of ions. The sum of these two energies gives the solvation enthalpy.

Properties. Electronic and optical properties of single-layer materials are extensively studied in the literature, as these two properties are arguably the most important for applications of single-layer materials. Two key parameters of electronic properties are the bandgaps of individual single-layer materials and the band alignments when contacting one single-layer material with a different material, which can be another single-layer material or a substrate or a liquid such as water.

The most important approximation for electronic structure calculations with DFT is the approximation of the exchange-correlation functional. Specifically, bandgaps from local and semi-local approximations to the exchange-correlation functional, such as the PBE functional [61], typically underestimate experimental bandgaps due to the lack of the derivative discontinuity [62]. Hybrid approximations on the other hand that include some fraction of exact exchange into the Hamiltonian, such as the HSE06 functional, provide bandgaps that agree well with experiment [63]. For example, we found that the HSE06 bandgap of single-layer BN is in excellent agreement with the experimental value [55]. Another approach to determine bandgaps is many-body perturbation theory such as the *GW* method [64], which calculates the quasiparticle energy bandgap that can directly be compared to photoemission/inverse photoemission experiments and hence has more physical meaning than the PBE and HSE06 Kohn-Sham eigenvalue bandgaps.

Another important electronic property is the band alignment for heterostructures. For single-layer materials, it is straightforward to calculate the band alignment, by aligning both the valence band maximum (VBM) and conduction band minimum (CBM) of the different materials that make up the heterostructure with reference to the vacuum energy level, which is typically set to zero [2]. The same method can also be applied to calculate the band edge positions of a single-layer semiconductor with respect to the redox potential energies of water splitting. This provides a critical criterion to examine whether the semiconductor is potentially useful for solar water splitting to generate hydrogen.

The optical properties of single-layer materials are important for their application in opto-electronic devices as well as for harvesting sunlight for energy-conversion. Calculations of the imaginary part of the permittivity and the corresponding optical absorption spectrum are two routine functions implemented in many DFT codes. However, to obtain accurate dielectric constant and optical absorption, one has to resort to solving the Bethe-Salpeter equation (BSE) based on *GW* quasi-particle energies and wavefunctions from standard DFT calculations [65, 66]. In addition, solving the BSE provides accurate optical bandgaps, which can directly be compared to the bandgaps measured with UV-vis transmission spectroscopy. For instance, recent calculations of the optical gap for single-layer SnS_2 using the BSE resulted in an optical bandgap of 2.75 eV [36], consistent with the measured optical bandgap of 2.55 eV [1].

Most synthesis method, such as CVD and MBE, require suitable substrates for the growth of single-layer materials. Therefore, the selection of a substrate material is of critical importance to the growth and further separation of a single-layer material. Similar to the generation of single-layer structures, the

starting point of substrate calculations is searching for candidate materials in the ICSD. For epitaxial growth, the goal is to choose candidate substrates with similar symmetry and surface lattice constants to minimize the mismatch strains between the single-layer and substrate materials. Then the adsorption energy for the single-layer material on the substrate can be calculated with the possible inclusion of van der Waals functional. The magnitude of the binding energy provides an indication about the bonding characteristics between the materials, i.e. if chemisorption and physisorption dominates. The determination of the bonding type provides guidance to experiment which substrate materials to select for the growth of targeted single-layer materials. For example, the (100) Pd facet should be suitable for the growth of single-layer tetragonal AlP, since this metal surface significantly reduces the formation energy of the single-layer material [19]. Non-epitaxial growth of single-layer materials provides an alternative synthesis approach that is expected to lead to somewhat lower absorption energies. An example is the growth of graphene on sapphire surfaces [67].

Only a few studies have yet used DFT-based tools to characterize the performance of single-layer materials, which are usually linked to transport properties of a electronic device. This is partly because of the intrinsic limitations of DFT being a ground-state theory. Recently, several studies have combined DFT methods with other numerical techniques such as non-equilibrium Green's functions (NEGF) to simulate transport properties of electronic devices based on single-layer materials [68]. In this study, e.g., the *I-V* characteristics of a single-layer MoS_2 transistor are determined. Additionally, tight-binding (TB) parameters fitted to the results of DFT calculations enable the calculation of the temperature-dependent carrier mobility. For instance, with such a combination of DFT and TB methods, the experimental dependence of electron and hole

mobility of crystalline naphthalene on temperature is perfectly reproduced in theoretical calculations [69]. The method could be applied to study the carrier mobility of single-layer materials, a quantity measured in experiments [70].

Figure 2.1 summarizes the above procedure of computational characterization for the discovery, characterization, and design of single-layer materials. Applying this theoretical recipe, we have discovered several families of previously unknown single-layer materials including group III-V materials [55, 19], oxides [54], and metal chalcogenides [36, 56, 2] with possible useful properties for electronic devices and as photocatalysts for water splitting.

CHAPTER 3

ELECTRONIC STRUCTURES OF SINGLE-LAYER BORON PNICTIDES

3.1 Abstract[1]

Single-layer materials such as graphene and boron nitride promise alternative routes to electronic devices. Hybrid density functional calculations for single-layer boron pnictides BN, BP, BAs and BSb show that these materials exhibit a direct band gap of 6.1, 1.4, 1.2 and 0.6 eV, respectively, that originates from the energy difference of the p_z orbitals of the species and is tunable by strain. The band gap linearly decreases with strain for BN, while it increases non-linearly for BP, BAs, and BSb. The calculated natural band offsets between the various boron pnictides are all of type I.

3.2 Introduction

Graphene [13] along with several other atomic membranes such as silicene [52] and graphynes [71] have attracted tremendous attention for their unique electronic properties like the massless Dirac fermions [72]. However, all these materials are semimetals and the lack of a band gap makes them currently unsuitable for logic applications in electronic devices [73]. Over the years, several methods have been suggested to open a gap in single-layer graphene. Among them, hydrogenation [74], fluorination [75], and the reduction of the dimensionality from 2D to 1D resulting in nanotubes or nanoribbons [76] are the most widely

[1]Reprinted with permission from: H. L. Zhuang and R. G. Hennig, *App. Phys. Lett.*, **101** (15), 153109 (2012). Copyright 2012 by American Institute of Physics.

used approaches. A recent theoretical study by Sahin *et al.* [51] explored another direction aiming at predicting single-layer materials with intrinsic band gaps instead of the above-mentioned functionalization methods. They found that single-layer boron pnictide compounds (BX) including boron nitride (BN), boron phosphide (BP), boron arsenide (BAs) and boron antimony (BSb) exhibit direct band gaps.

In this study, we perform density-functional theory (DFT) calculations to elucidate the mechanism of band gap formation in the boron pnictides, determine the effect of strain on the gap, and predict the natural band offsets between the various BX compounds and graphene. We find that the Heyd-Scuseria-Ernzerhof (HSE06) hybrid functional provides accurate band gaps. The application of biaxial strain reduces the band gap of BN and increases it for BP, BAs, and BSb. We calculate the natural valence and conduction band offsets (VBO and CBO) of graphene and the BX heterostructures. The VBOs between graphene and BX are 1.42, 0.83, 0.71, and 0.16 eV for X=N, B, P, As, and Sb,respectively. The corresponding conduction band offsets are 4.65, 0.53, 0.47, and 0.45 eV.

3.3 Methods

The DFT calculations are performed with the Vienna *Ab initio* Simulation Package (VASP) [59], a density-functional code using a plane-wave basis and the projector-augmented wave method [77, 78]. For the exchange-correlation functional, we compare results from the local density approximation (LDA) [79] and the Perdew-Burke-Ernzerhof (PBE) general gradient approximation [61]. To overcome the band gap problem of semi-local exchange-correlation function-

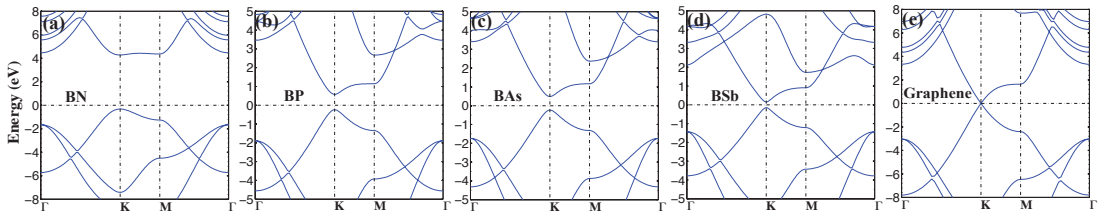

Figure 3.1: Band structures of (a) BN, (b) BP, (c) BAs, (d) BSb and (e) graphene. These band structures are in similar shapes, and one notable difference is the energy gap that occurs in BX at the K point.

als, we employ the HSE06 hybrid density functional [80]. A plane-wave cutoff energy of 800 eV ensures energy convergence to within 1 meV/atom.

Although only BN has yet been synthesized [14], we assume that all single layer boron pnictide structures occur in the same crystal structure as BN. Resembling graphene, BN exhibits a honeycomb lattice with two atoms per unit cell [14]. Each B atom is 3-fold coordinated to the neighboring pnictide atoms. In our calculations, we assume a slab geometry with a large vacuum spacing of 18 Å to reduce interactions between the layers. The sum of the covalent radii of B and X atoms provide an initial estimate of the B-X bond lengths. Four-atom rectangular cells are used to calculate the elastic modulus defined below. For the Brillouin zone integration, 120×120×1, 40×70×1 and 15×15×1 of Monkhorst-Pack [81] *k*-point grids are used for two-atom cells, four-atom cells and the HSE06 functional, respectively. All atomic configurations are relaxed until the Hellmann-Feynman forces are less than 1 meV/Å and the in-plane stresses are below 0.01 GPa. The HSE06 calculations used the relaxed PBE geometries. The electronic band structure and density of states are calculated starting from the fully relaxed configurations and self-consistent charge densities.

Table 3.1: Structural properties of single-layer boron pnictides. The bond length b_0 in Å, cohesive energy E_{coh} in eV/atom, and elastic modulus C in N/m are calculated for the LDA and PBE functional. The cohesive energies are calculated in reference to the spin-polarized B and X atoms. The energy differences ΔE_{tot} between single layered and bulk zinc-blende structures in eV/atom are calculated with the LDA functional.

Material	b_0^{LDA}	b_0^{PBE}	E_{coh}^{LDA}	E_{coh}^{PBE}	ΔE_{tot}^{LDA}	C^{LDA}	C^{PBE}
graphene	1.412	1.424	8.94	7.97	0.03	389	353
silicene	2.209	2.231	4.58	3.96	0.76	108	102
BN	1.437	1.451	8.05	7.10	0.09	329	300
BP	1.835	1.855	5.80	5.00	0.52	172	163
BAs	1.931	1.958	5.16	4.33	0.52	146	136
BSb	2.128	2.158	4.51	3.73	0.59	119	109

3.4 Results

Table 3.1 compares the bond lengths and cohesive energies of the boron pnictides with graphene and silicene. The cohesive energy and bond length agree well with previous LDA calculations [51]. As expected, the bond lengths increase with atomic number and covalent radii. The cohesive energies of the layered boron pnictides are all lower than for the bulk zinc blende structure. However, the energy difference between the layered and bulk structures of about 0.5 eV/atom are comparable in magnitude to the differences observed for graphene and silicene and their bulk diamond structure counterparts. The stability follows the order: graphene > BN > BAs > BP >BSb> silicene. Previous phonon calculations by Sahin *et al.* showed that the layered compounds

are mechanically stable [51]. The existence of silicene has been confirmed experimentally [16], indicating that the layered boron pnictides BP, BAs and BSb might be metastable as single-layer materials.

The elastic modulus C of the boron pnictides is calculated since it presents an important mechanical parameter,

$$C = \frac{1}{A_0} \cdot \frac{\partial^2 E}{\partial \epsilon^2}, \tag{3.1}$$

where A_0 is the equilibrium area of the rectangular cell, and E is the total energy at an elastic strain ϵ. No experimental data of the elastic modulus is available for the BX series. Our calculated values for graphene are in excellent agreement with the experimental value of 340±50 [30], indicating the accuracy of DFT for these layered materials.

Figures 3.1(a)-(f) compare the LDA band structure of the boron pnictides with the one of graphene. The band structures exhibit similar features. In particular, the σ-bands of BX around the Γ point are almost identical to that of graphene, indicating that the B and X atoms in the boron pnictides are strongly bonded via sp^2 covalent bonds. Despite the similarity, the band structures of the boron pnictides show a remarkable difference. For graphene, the valence and conduction bands are cone-shaped and degenerate at the Dirac K point. However, for BX, these two bands are separated by sizable band gaps.

Table 3.2 shows the band gaps of the boron pnictides for the LDA, PBE and HSE06 functional. The excellent agreement for BN of the HSE06 band gap with the experimental value of 5.97 eV indicates that the hybrid functional provides highly accurate band gaps for these layered systems [82]. A common trend is observed for all three functionals; the band gap decreases across the pnictide series from N to Sb. The LDA and PBE band gaps closely agree with each other

Table 3.2: Electronic properties of single-layer boron pnictides. The band gap E_g in eV are calculated with the local LDA, semilocal PBE, and hybrid HSE06 functionals. The VBOs are calculated with the PBE functional and CBOs are determined by adding the HSE06 band gaps to the VBOs.

Material	E_g^{LDA}	E_g^{PBE}	E_g^{HSE}	CBO	VBO
BN	4.48	4.64	6.07	4.65	1.42
BP	0.82	0.90	1.36	0.53	0.83
BAs	0.72	0.75	1.18	0.47	0.71
BSb	0.29	0.32	0.61	0.45	0.16

and the LDA band gaps of Ref. [51]. Our HSE band gaps differ from those calculated by GW_0 approximation in the same reference, since the GW_0 approximation often overestimates band gaps [83]. It is worth emphasizing that the band gap of the boron pnictides is a direct gap, quite different from their bulk counterparts, some of which are well-known indirect band gap semiconductors [84, 85]. The band gap type transition due to reducing the dimensions from 3D to 2D seems to be a common phenomenon [86] and may provide a general path to application of these layered materials in electronic devices [3].

To understand the origin of the band gaps in BX, we perform a tight binding (TB) analysis, considering the hopping matrix elements for the interaction between the p_z orbitals on nearest neighbor sites and neglecting any orbital overlaps. Following Ref. [87], the Hamiltonian is

$$H = \begin{pmatrix} \epsilon_B & t \cdot f(k) \\ t \cdot f(k)^* & \epsilon_X \end{pmatrix} \tag{3.2}$$

where ϵ_B and ϵ_X are the onsite p_z orbital energies of the B and X atoms, respec-

tively, t is the hopping integral, and $f(k)$ is defined as

$$f(k) = e^{ik_x a/\sqrt{3}} + 2e^{-ik_x a/\sqrt{3}} \cos\left(\frac{k_y a}{2}\right) \tag{3.3}$$

here, k_x and k_y are the components of the wavevector $\vec{k}$ and a is the lattice constant of BX. Solving the secular equation, $\det(H - E) = 0$ gives the eigenvalues for the conduction and valence π-bands

$$E(k) = \frac{\epsilon_B + \epsilon_X}{2} \pm \left(\left(\frac{\epsilon_B - \epsilon_X}{2}\right)^2 + (t \cdot f(k))^2\right)^{1/2} \tag{3.4}$$

At the Dirac K point, $f(k)^2 = 0$, resulting in the energy band gap

$$E_g = |\epsilon_B - \epsilon_X| \tag{3.5}$$

Equation (3.5) reveals that E_g depends on the energy difference between the p_z orbitals of B and X. For graphene and silicene $E_g = 0$, since the orbital energies on both lattice sites are identical. The difference in the LDA energy of the p_z orbitals for a pair of isolated B and X atoms are 4.3, 2.1, 1.8, and 1.2 eV for X=N, P, As, and Sb, respectively, following the same trend as the band gaps of the layered boron pnictides shown in Table 3.2. The bonding interaction between the B and X atoms alters the orbital energies in the layered compounds. The ionicity of the bonds are controlled by the electronegativity (EN) difference between the atoms. The Pauling EN values of B, N, P, As and Sb are 2.0, 3.0, 2.1, 1.9 and 1.9, respectively [88]. The Bader charge analysis [89] shows that the transferred charge in BN, BP, BAs and BSb are +2.1, +0.54, +0.34, −0.41 electrons from B to X, respectively. The orbital energies of the atoms and the ionicity of the bonds explain the order of the band gaps and why BN has a much larger gap than the other layered boron pnictide compounds.

The band structures of BX are significantly affected by biaxial strain, i.e. by expanding or shrinking of the crystal lattice. Figure 3.2 shows the value of the

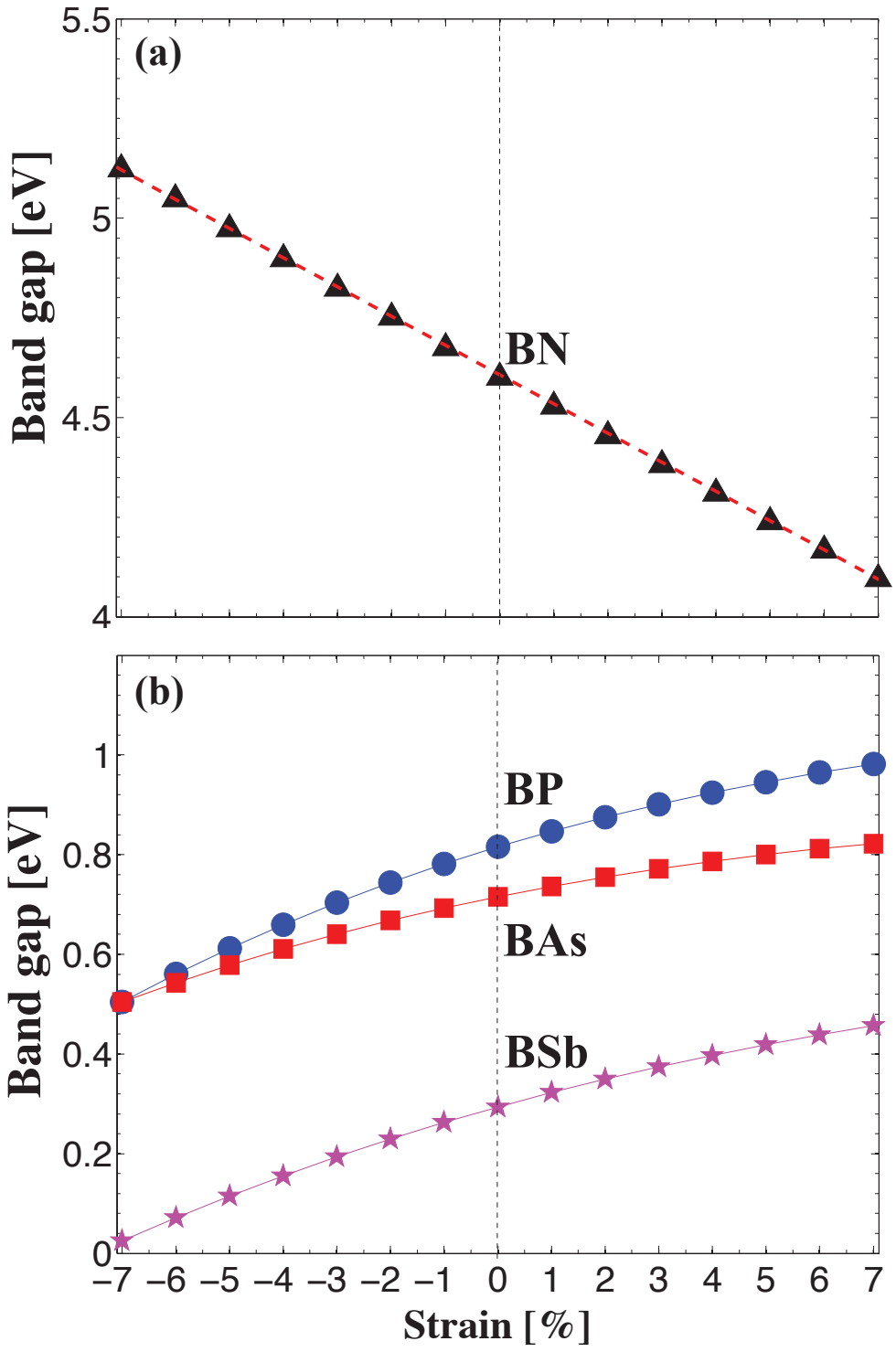

Figure 3.2: Change of the band gap with strain for (a) BN and (b) BP, BAs and BSb layered structures.

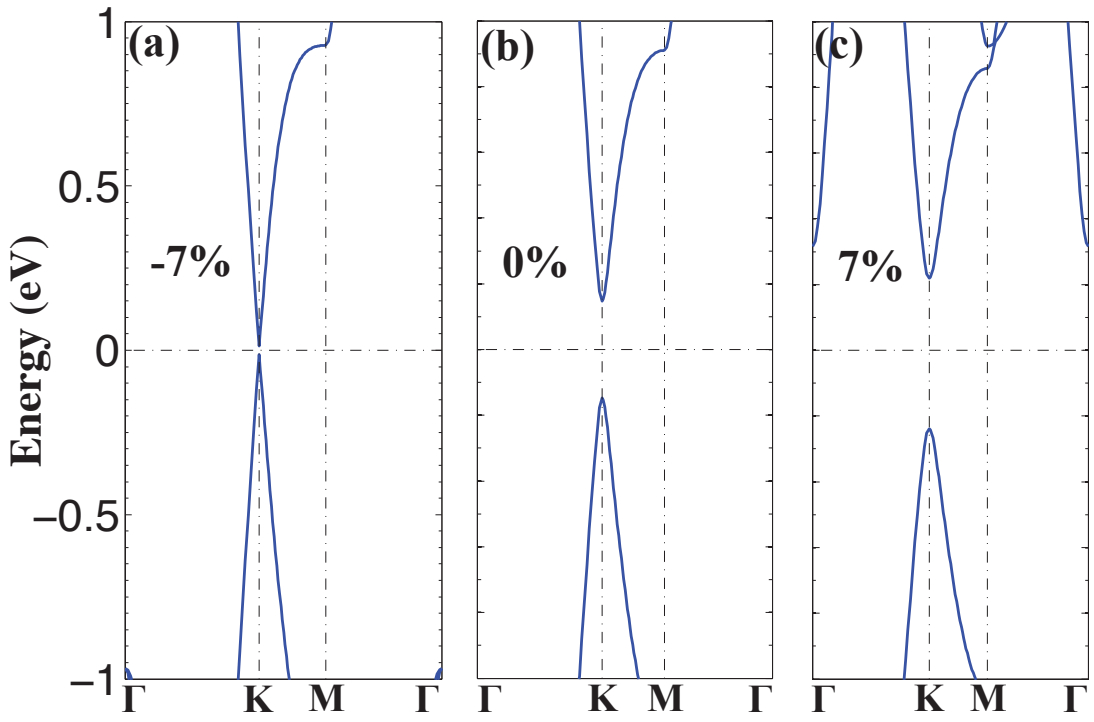

Figure 3.3: Band structure of BSb near the K point at strains of (a) -7% (b) 0% and (c) 7%.

band gaps as a function of applied strain in the range of −7% to +7%. For BN, the band gap is reduced with increased strain, closely following the linear relationship $E_g(eV) = -0.0733\epsilon + 4.6075$, shown as the red line in Fig. 3.2a. BP, BAs and BSb on the other hand, show the reverse trend that the band gap increases with increasing strains. Furthermore the dependence of the gap on strain is non-linear. For BP and BAs, at small strains around -7%, their band gaps are similar and for larger strains the difference between the band gaps increases.

Strains also affect the shape of the π and π^* bands near the K point. In general, their shapes approaches that of a Dirac cone with increasing compressive strain as seen in Fig. 3.3 for BSb. Interestingly, for BSb the band gap almost disappears at −7% compressive strain and the band dispersion shows a nearly

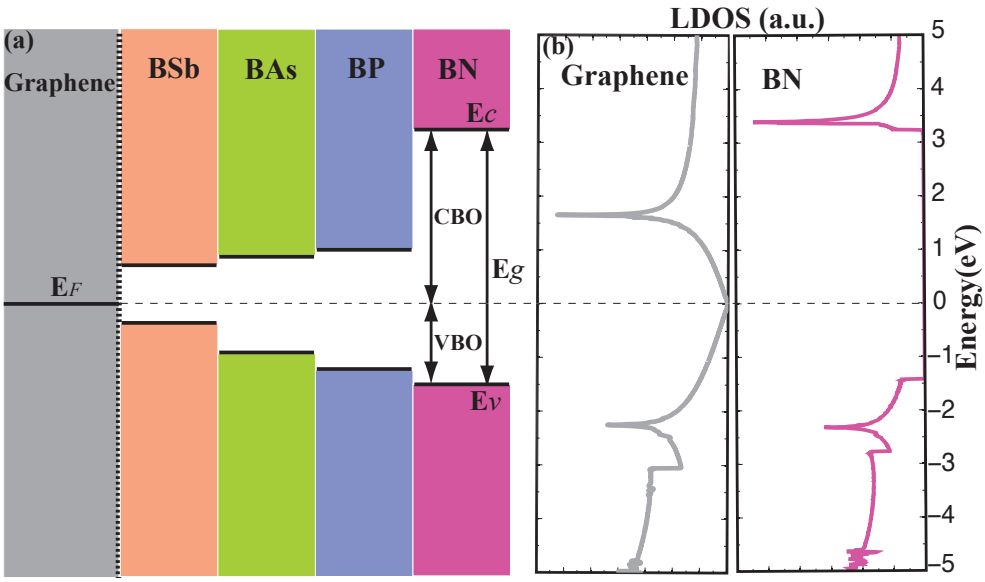

Figure 3.4: (a) Band alignment of the single-layer boron pnictides and graphene calculated from (b) the local density of states of graphene (left) and BN (right) layers in a supercell heterostructure.

linear relation, similar to graphene. A linear fit estimates the Fermi velocity $v_F = 1/\hbar \cdot \partial E/\partial k$ at the strain of -7% for BSb to be $0.66 \cdot 10^6$ m/s, which is more than half of the experimental value for graphene of $v_F = 1.1 \cdot 10^6$ m/s [72].

VBOs and CBOs are calculated based on the energy difference of valence and conduction band edges of BX relative to the common Fermi level E_F in the heterostructures [90]. We use supercell models for these calculations containing a single layer of BX and of graphene. Since standard DFT provides accurate ground state energies, the PBE functional is used to obtain the valence band edge energy. For the conduction band edge energy, however, we use the HSE06 functional instead, which accurately predicts the band gaps. In order to satisfy periodic boundary conditions, the supercells (e.g. the graphene/BSb heterostructure is constructed with $2 \times 2 \times 1$ BSb unit cells and $3 \times 3 \times 1$ graphene unit cells) exhibit small strains of less than 2% applied to the graphene layer

in order to match the lattice constants of both layers. Fig. 3.4 illustrates the band alignment of the graphene/BX heterostructures. The values of the CBOs and VBOs are listed in Table 3.1. Both the CBO and VBO decreases with increasing atomic number of the X elements in BX and the band offsets are all of type I. We expect that these data will provide valuable guidance in designing graphene/BX based electronic devices.

3.5 Summary

In summary, we have demonstrated that single-layer boron pnictide compounds have direct band gaps at the K point. Based on a simple tight binding analysis, we suggest that the origin of these band gaps are the different electronegativities of B and X atoms in BX. Furthermore, the band gaps of the boron pnictides can be tuned by mechanical strains. Finally, we determined the band offsets for the graphene/boron pnictide heterostructures and show them all to be of type I.

CHAPTER 4

COMPUTATIONAL DISCOVERY OF SINGLE-LAYER III-V MATERIALS

4.1 Abstract[1]

Single-layer materials open up tremendous opportunities for nanoelectronic devices. Using a first-principles design approach we identify a previously unrecognized family of single-layer III-V materials. We determine their energetic and dynamical stability, identify a surprising reconstruction, and calculate their electronic properties using a hybrid density functional and the G_0W_0 method. Our results provide guidance for experimental synthesis efforts and future searches of single-layer materials suitable for device applications.

4.2 Introduction

The last two decades have seen an explosion of interest in two-dimensional materials, which now can be synthesized in either single, or a few atomic layer form [91, 92, 93]. The discovery of novel fabrication methods for creating two-dimensional materials such as graphene [13], zinc oxide [15], silicon carbide [94], boron nitride [95], and molybdenum disulfide [86] has opened a new field of materials research with promising applications in nanoelectronic devices. Single-layer materials not only represent the ultimate scaling in the vertical direction, but also show a variety of novel and useful electronic, optical, and

[1]Reprinted with permission from: H. L. Zhuang, A. K. Singh and R. G. Hennig, *Phys. Rev. B*, **87** (16), 165415 (2013). Copyright 2013 by American Physics Society.

mechanical properties. However, the number of materials that have been synthesized in two-dimensional (2D) form is limited. There are potentially many more candidate materials awaiting discovery, which could have transformative properties in device applications [96, 55].

Density-functional theory (DFT) has the potential to predict the stability of proposed materials and has already played an important role in predicting the existence of single-layer materials. For example, metastable structures of silicene and graphyne have been predicted by DFT [52, 71], and experimental efforts have tried synthesizing these single-layer materials [16]. Searches for other 2D materials, especially semiconductors beyond those already fabricated, have continued [96, 55].

The two primary questions in this search are (i) what is the stability of these single-layer materials and (ii) how are their electronic structures altered due to reduced dimensionality. In this paper, we answer these two questions for the family of single-layer group III-V materials. We first identify all suitable candidate materials that exhibit the same 3D crystal structure types as occur in the systems with known 2D materials. To determine the stability of the 2D materials, we compare the formation energies to the corresponding bulk energies and calculate their phonon spectra. For 2D materials with unstable phonon modes, we investigate different reconstructions. Hybrid density-functional and G_0W_0 calculations that can accurately predict the band gap of materials [97, 98, 99] are used to determine the band structure of the 2D materials. Finally, we construct a diagram illustrating the relationship between band gaps and lattice constants which supplements current 3D materials selection diagrams, that are widely used for the design of electronic devices in the semiconductor technology.

4.3 Methods

All calculations are based on DFT using the projector augmented wave (PAW) method as implemented in the plane-wave code VASP [59, 77, 78]. For the structural relaxations and energy calculations we employ the generalized gradient approximation with the PBE parametrization [61]. To overcome the problem of band gap underestimation in semilocal exchange-correlation functionals, the Heyd-Scuseria-Ernzerhof (HSE06) hybrid functional and the G_0W_0 method are used for calculating the band structures [63, 97, 98, 99]. A cutoff energy of 400 eV for the plane wave basis set is used throughout all calculations and ensures an accuracy of the energy of 1 meV/atom. The k-point sampling uses the Monkhorst-Pack scheme [81] and employs for the 2D materials a 120×120×1 mesh for the PBE functional, a 12×12×1 mesh for the more expensive HSE06 functional, and a 32×32×32 mesh for the bulk systems resulting in a similar accuracy as the cutoff-energy convergence. For the G_0W_0 calculations, we employ 64 bands, 96 frequency points and a 18×18×1 k-point mesh. For the 2D materials a vacuum spacing of 18 Å ensures that the interactions between the layers are negligible.

We identify all materials that exhibit the same 3D crystal structure types as occur in the systems with the known 2D materials C, BN, ZnO, SiC [13, 95, 15, 94] using the Inorganic Crystal Structure Database [100]. For the group III-V systems, the relevant 3D crystal structures are wurtzite and zincblende. Initially, we assume that all binary group III-V 2D materials have the same hexagonal structure as single-layer boron nitride and then explore buckled hexagonal and other structures [14]. We fully optimize all structures until the forces and in-plane stresses are converged to within 1 meV/Å and 0.01 GPa, respectively.

The energetic stability of the proposed single-layer materials with respect to their bulk forms is determined by the energy difference $\Delta E = E_{2D}/N_{2D} - E_{3D}/N_{3D}$, where E_{2D} and E_{3D} denotes the energy of the 2D and 3D bulk (zincblende or wurtzite) system, respectively. N_{2D} and N_{3D} refer to the number of atoms in the respective unit cells.

To investigate the dynamical stability of all single-layer materials we calculate their phonon spectra, using density-functional perturbation theory [57, 101]. Due to the heteropolar characteristics of each material, it is important to include the long range Coulomb forces in the force constant matrix [57, 102]. The force constants consist of both analytic and non-analytic contributions, the latter of which depends on the Born effective charges Z^* and the macroscopic dielectric constant ϵ_∞ [57]. We calculate Z^* and ϵ_∞ and include the non-analytic contribution in our force constant matrix to determine the phonon spectra.

4.4 Results

4.4.1 Single-Layer Hexagonal III-V Materials

Figure 4.1(a) and Table 4.1 show the energy differences ΔE_{hex} and lattice parameters a_{hex} of the hexagonal 2D group III-V materials. The formation energies relative to the respective bulk phases range from 0.38 eV/atom for InSb to 0.52 eV/atom for AlP. While these formation energies are quite high, they are comparable to that of single-layer SiC (ΔE_{hex} = 0.50 eV/atom), which has indeed been fabricated successfully [94]. This indicates that it might be feasible to grow hexagonal single-layer III-V materials on suitable substrates that reduce

Table 4.1: Structural parameters and energy differences ΔE of the 2D hexagonal and tetragonal group III-V materials relative to the known 3D crystal structures. The structural parameters include the lattice constants a and the buckling z.

	AlN	AlP	AlAs	AlSb	GaN	GaP	GaAs	GaSb	InN	InP	InAs	InSb
						—— 2D hexagonal ——						
ΔE_{hex} (eV/atom)	0.51	0.52	0.50	0.48	0.42	0.45	0.41	0.39	0.45	0.44	0.41	0.38
a_{hex} (Å)	3.12	3.94	4.06	4.40	3.25	3.91	4.06	4.38	3.63	4.25	4.38	4.68
z_{hex} (Å)	0	0	0.45	0.63	0	0.43	0.59	0.70	0	0.52	0.67	0.76
						—— 2D tetragonal ——						
ΔE_{tetr} (eV)	0.58	0.31	0.22	0.16	0.76	0.44	0.32	0.22	0.60	0.43	0.32	0.23
a_{tetr} (Å)	3.61	3.95	4.03	4.22	3.78	3.97	4.06	4.28	4.28	4.43	4.48	4.66
z_{tetr} (Å)	0.58	1.41	1.56	1.80	0.68	1.50	1.61	1.80	0.63	1.55	1.69	1.88

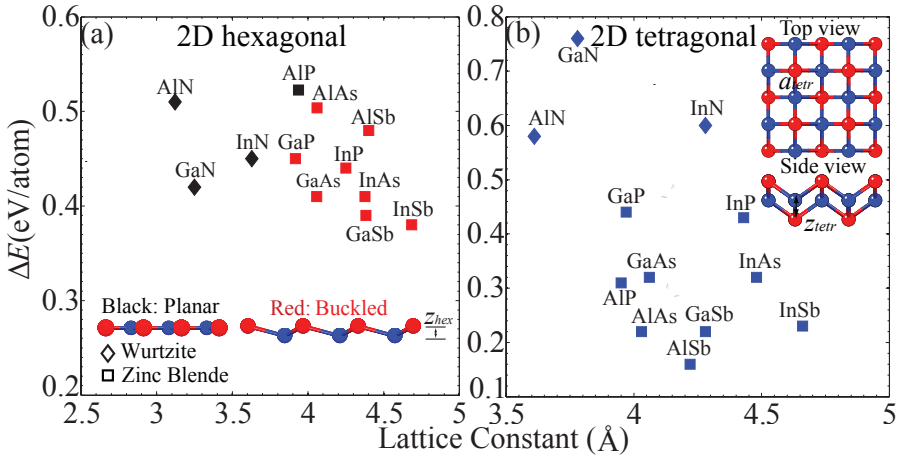

Figure 4.1: Energy differences ΔE between the 2D and bulk structures as a function of lattice parameter for 2D group III-V materials with (a) hexagonal and (b) tetragonal structure. The diamond and square symbols denote the energy differences with respect to the hexagonal wurtzite and cubic zincblende structure, respectively. Black indicates that the hexagonal structure is planar, while red means that the hexagonal structure is buckled.

the formation energies and stabilize the structures.

Two types of hexagonal structures, a planar and a buckled one, are obtained by relaxations [96]. The buckling is illustrated in Fig. 4.1(a) and the amount of buckling z_{hex} is shown in Tab. 4.1. We observe that the nitrides and AlP prefer planar structures, while all others exhibit buckled structures. This structure trend can be understood from the energy balance between (i) the electrostatic potential energy of the ions and (ii) the bonding energy of the sp^2 and sp^3 hybridization that is reflected in the preference of each ion for a trigonal planar or pyramidal configuration.

The alternating buckling of the layered hexagonal materials results in a dipole moment across the layer whose electrostatic energy is proportional to Q^2/a^2, where Q is the ionic charge of the species and a the lattice parameter.

Figure 4.2(a) shows that for each group in the III-V family, the energy difference $\Delta E_{\text{buckling}}$ between the hexagonal planar and buckled geometries decreases rapidly with increasing Q^2/a^2, illustrating the importance of the electrostatic interaction in the stabilization of the buckled and planar structures. The large electronegativity difference for the nitrides and AlP results in large ionic charges that is reflected in the Bader charges shown in Tab. 4.2. The large charges combined with their small lattice parameters make the buckling energetically unfavorable in the nitrides and AlP.

The ionic interactions alone, however, are not sufficient to completely explain the observed structural trends and the preference for each of the ions in the III-V compounds for sp^2 or sp^3 hybridization needs to be considered. The group III elements B, Al, Ga, and In can all form planar trigonal sp^2 bonded molecular structures with D_{3h} symmetry, *e.g.*, trihydrides and trihalides. For the group V elements, the most common configuration is pyramidal trigonal. For the case of the nitrogen atom, a trigonal planar configuration can form if the lone pair occupies a p orbital that can participate in an aromatic bond by forming π bonds. An example for such a system is indole, where the energetic stabilization from the aromatic system leads to the formation of sp^2 orbitals and a trigonal planar nitrogen configuration. The small energy difference between sp^2 and sp^3 bonded configurations of nitrogen is also reflected in the small activation energy for pyramidal inversion of trivalent nitrogen compounds such as in NH_3. In contrast, in phosphorous compounds and compounds of the heavier group V elements, Ga and In, this activation energy is considerably greater owing to the stronger energetic preference for sp^3 hybridization. In general, the heavier group V elements P, As, and Sb favor trigonal pyramidal sp^3 bonded configurations with C_{3v} symmetry, as seen in the trihydrides [103].

The combination of the trend to form sp^3-bonded trigonal pyramidal structures for the heavier group V elements and the lower electrostatic energy (Q^2/a^2) for the later group III-V compounds explains the observation that only the nitrides and AlP exhibit planar hexagonal configurations.

The dynamical stability of the hexagonal 2D materials is determined by the phonon spectra shown in Fig. 4.3. Out of the twelve III-V materials only AlP, AlAs and GaSb show imaginary frequencies, demonstrating that the other nine are dynamically stable. The phonon frequencies at high symmetry k points agree with previous studies [96]. However, one notable difference is that our calculations capture an important phonon feature of heteropolar materials, the splitting of longitudinal and transverse optical modes (denoted as the LO and TO branches in Fig. 4.3) at the Γ point.

Table 4.2 shows the Born effective charges Z^*, the macroscopic dielectric constants ϵ_∞, the phonon frequencies of the LO and TO branches (ω_{LO} and ω_{TO}), as well as the splitting magnitude $\Delta\omega = \omega_{LO} - \omega_{TO}$ for the 2D hexagonal III-V materials. As can be seen, the frequency splitting magnitude follows the same trend as the ionicity trend in each cation subgroup. For example, in the subgroup In pnictides, $\Delta\omega$ decreases from 55 cm^{-1} for InN to merely 11 cm^{-1} for InSb. AlN has the largest $\Delta\omega$ due to its high ionicity.

Table 4.2 also lists the Bader charges Q that describe how much charge is transferred from the group III to the group V atoms in the 2D hexagonal structures. We find that the charge transfer decreases in each subgroup following electronegativity trends. As a consequence of the decreased ionicity, the structures buckle and the orbital hybridization changes from sp^2 to sp^3. Noteworthy, while a static description of the charge, the Bader charge follows the frequency

splitting trend in each subgroup, namely, a larger Bader charge transfer corresponds to a larger LO-TO splitting magnitude.

4.4.2 Single-Layer Tetragonal III-V Materials

The phonon spectra of hexagonal AlP, AlAs, and GaSb shown in Fig. 4.3 indicate that they are dynamically unstable. A possible reason for the instability is the dipole moment in the direction perpendicular to the single-layer plane. Thus, a reconstruction that reduces the dipole moment could stabilize the structure. We start with a planar hexagonal configuration and displace neighboring cation-anion pairs perpendicular to the plane such that the net dipole moment is zero. Optimization of this structure results in a tetragonal structure illustrated in the insets of Fig. 4.1(b). This structure has space group 129 ($P4/nmm$), Schönflies symbol D_{4h}^{7}, and is characterized by the lattice constant a_{tetr} and the out-of-plane displacement z_{tetr}. Surprisingly, unlike the 3-fold coordinated planar or buckled hexagonal structure, each cation and anion in the tetragonal structure is bonded to four neighboring anions and cations, respectively. The 2D tetragonal AlP, AlAs, and GaSb structures are mechanically stable as illustrated by their phonon spectra in Fig. 4.3.

To further test the stability of the tetragonal 2D materials, we perform *ab-initio* molecular dynamics simulations for the tetragonal AlP system using a 5×5×1 supercell and the PBE functional. A Nosé thermostat sets the temperature to 600 K [104]. The simulation is performed for a total time of 2 ps using a timestep of 1.5 fs. Geometry optimizations of several molecular dynamics snapshots for the tetragonal AlP system result in the original tetragonal structure.

This suggests that 2D tetragonal AlP is stable at a temperature of 600 K.

Although most of the III-V materials are dynamically stable in the 2D hexagonal structure, we also calculate their energy in the tetragonal structures. Table 4.1 and Fig. 4.1(b) show their energy relative to the bulk phases and the structural parameters. Except for AlN, GaN, and InN, all other III-V materials have lower energies in the tetragonal structures than the hexagonal one. Therefore, the hexagonal structure is not the only possible metastable 2D structure for the group III-V materials. The energy ΔE_{tetr} decreases in each subgroup. Notably, some 2D tetragonal III-V materials have very low formation energies of the order of 0.2 eV/atom. For example, the formation energy of AlSb is 0.16 eV/atom which is close to the energy of the previously synthesized ZnO of 0.19 eV/atom. This indicates that it is more likely to grow AlSb in the 2D tetragonal structure than in the 2D hexagonal one.

To understand why tetragonal structures are favored over hexagonal structures in most group III-V materials, we plot the energy difference $\Delta E_{\text{hex}-\text{tetr}}$ between the hexagonal and tetragonal structures as a function of Q^2/a^2 of the hexagonal structures in Fig. 4.2(b). The energy difference $\Delta E_{\text{hex}-\text{tetr}}$ decreases with increasing importance of the electrostatic interactions measured by Q^2/a^2. This trend is consistent with the explanation that most 2D group III-V materials tend to form tetragonal structures in order to reduce their dipole moment perpendicular to the layered materials.

4.4.3 Electronic Structure of Single-Layer III-V Materials

Figure 4.4 shows the band structures obtained using the HSE06 hybrid functional and Tab. 4.2 compares the band gaps obtained with the HSE06 functional and the G_0W_0 method. The HSE06 and the G_0W_0 method predict similar band gaps with the G_0W_0 band gaps being slightly larger. Comparison with experimental data for the single-layer materials BN, fluorographene, and MoS_2 show that the GW method in these related systems overestimates the band gap [83, 96]. As expected, all the band structures of the 2D hexagonal structures exhibit similar shapes. One common feature of these band structures is the occurrence of the valence-band maximum (VBM) at the K point, whereas the conduction-band minimum (CBM) positions appears at the Γ point. In other words, all these hexagonal 2D materials have indirect band gaps, different from the corresponding 3D group III-V materials with mixed band gap types [105]. For example, InP has a direct band gap in 3D, and the band gap type changes to indirect due to dimension reduction.

Figure 4.5 shows the relationship between the size of the band gap of the 2D materials and their lattice constants. As illustrated by the color spectrum, most of the band gaps lie within the range of visible light, indicating that these 2D materials may be useful for optoelectronic or photocatalytic applications. Of all twelve materials, AlN has the largest band gap of 4.85 eV. However, this value is still small compared to its wurtzite bulk phase, which has a wide band gap of 6.2 eV [106].

An important parameter for semiconductor device materials is the electron/hole effective mass, denoted as m_h^* and m_e^*, respectively. This parameter affects carrier mobility. From the HSE06 band structure we calculate the av-

erage m_e^* for the CBM at the Γ point, and the m_h^* for the VBM at the K point. Table 4.2 lists the effective masses $m_{e/h}^*$ of the 2D hexagonal materials. The relative $m_{e/h}^*$ are illustrated in Figure 4.5. The m_e^* of most hexagonal 2D group III-V materials are comparable to silicon, which has an average $m_e^* = 0.26m_e$ [107]. In addition, these m_e^* are similar to or smaller than that of single-layer MoS_2 with a theoretical value of $m_e^*/m_e = 0.483$ [5]. Single-layer MoS_2 has recently been shown to work in transistor devices [3]. The similarity between the calculated electronic properties illustrates the potential of the predicted 2D hexagonal III-V materials for electronics applications.

With the HSE06 functional, we also calculate the band structures of the 2D tetragonal structures exhibiting lower energies than their hexagonal counterparts. Surprisingly, except AlP and AlAs, the other seven materials become metallic. The band structures of AlP, AlAs and GaSb are shown in Fig. 4.4. It can be seen that even the band gap types of AlP and AlAs are different. AlP has an indirect band gap of 1.89 eV, while AlAs has a direct band gap of 0.79 eV. Moreover, the m_e^* of tetragonal AlP and AlAs at the Γ point are 0.50 and 0.40 m_e, respectively.

To understand the origin of the metallic character of most tetragonal 2D materials, we analyze the density of states for 2D hexagonal and tetragonal GaSb shown in Fig. 4.6. For the semiconducting hexagonal GaSb, Fig. 4.6(a) shows that the valence band maximum is dominated by the Sb p states. The conduction band minimum (CBM) on the other hand is dominated by about equal contributions from the Sb s and Ga sp^3 states. In contrast, for metallic tetragonal GaSb, Fig. 4.6(b) shows that the density of states near the Fermi level is dominated by the p states of Sb with the sp^3 states of Ga being absent. The metallic

character of the 2D tetragonal GaSb originates from the partly filled band that is dominated by states of p character localized on the Sb sites. Although the semiconductor-to-metal transition may be less appealing for growing 2D semiconductors, stacking various tetragonal structures may lead to useful metal-semiconductor heterojunctions.

4.5 Summary

In summary, we identified a large number of metastable 2D materials in the group III-V family. We identified three different 2D structures that are dynamically stable in this family of materials, a planar honeycomb hexagonal structure, a buckled hexagonal structure, and a surprising low-energy tetragonal structure. Using the HSE06 functional, we obtained accurate energy band gaps and electron/hole effective masses. Our results provide valuable guidance to synthesis efforts and potential applications of 2D group III-V materials.

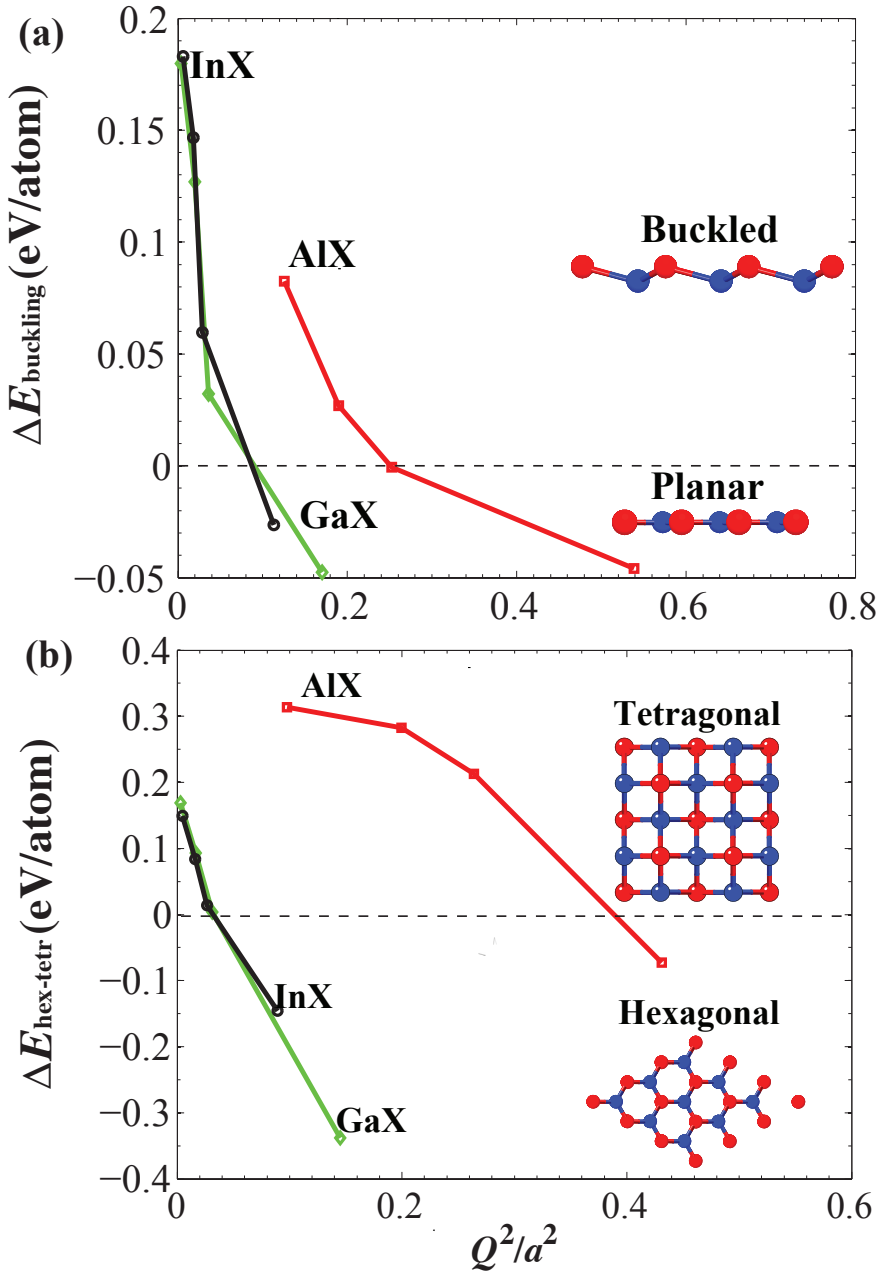

Figure 4.2: (a) Energy difference between hexagonal planar and hexagonal buckled geometries as a function of Q^2/a^2. (b) Energy difference between the hexagonal and tetragonal geometries as a function of Q^2/a^2.

Table 4.2: Electronic and phonon properties of the 2D hexagonal group III-V materials. Shown are the band gaps E_g^{HSE} and the electron and hole effective masses m_e^*/m_e and m_h^*/m_e, respectively, obtained from HSE06 calculations, the quasiparticle band gaps from G_0W_0 calculations, the Bader charges Q_{Bader} transferred from the group III to the group V atoms, the Born effective charges Z^*, the macroscopic dielectric constant ϵ_∞, the phonon frequencies ω_{LO} and ω_{TO} at the Γ point, and the frequency splitting $\Delta\omega$.

	AlN	AlP	AlAs	AlSb	GaN	GaP	GaAs	GaSb	InN	InP	InAs	InSb
E_g^{HSE} (eV)	4.85	3.24	2.49	2.07	3.23	2.51	1.83	1.43	1.52	1.80	1.41	1.25
$E_g^{G_0W_0}$ (eV)	5.03	3.93	3.08	2.17	4.00	3.21	2.39	1.88	1.57	2.32	1.81	1.62
m_e^*/m_e	1.24	0.59	0.48	0.38	0.69	0.41	0.33	0.28	0.43	0.37	0.32	0.28
m_h^*/m_e	2.33	1.37	1.20	1.01	1.97	1.16	1.06	0.91	2.26	1.39	1.27	1.09
Q (e)	2.29	1.98	1.77	1.56	1.34	0.74	0.57	0.27	1.22	0.72	0.59	0.36
Z^* (e)	2.71	3.02	2.92	2.79	3.23	3.12	3.06	2.85	3.83	3.44	3.39	3.20
ϵ_∞	1.64	2.57	3.11	4.11	1.98	3.24	4.16	5.64	4.08	3.64	4.74	5.80
ω_{LO} (cm^{-1})	903	569	434	355	809	442	302	237	647	369	332	190
ω_{TO} (cm^{-1})	812	524	403	335	722	409	282	226	592	335	306	179
$\Delta\omega$ (cm^{-1})	91	45	31	20	87	33	20	11	55	34	26	11

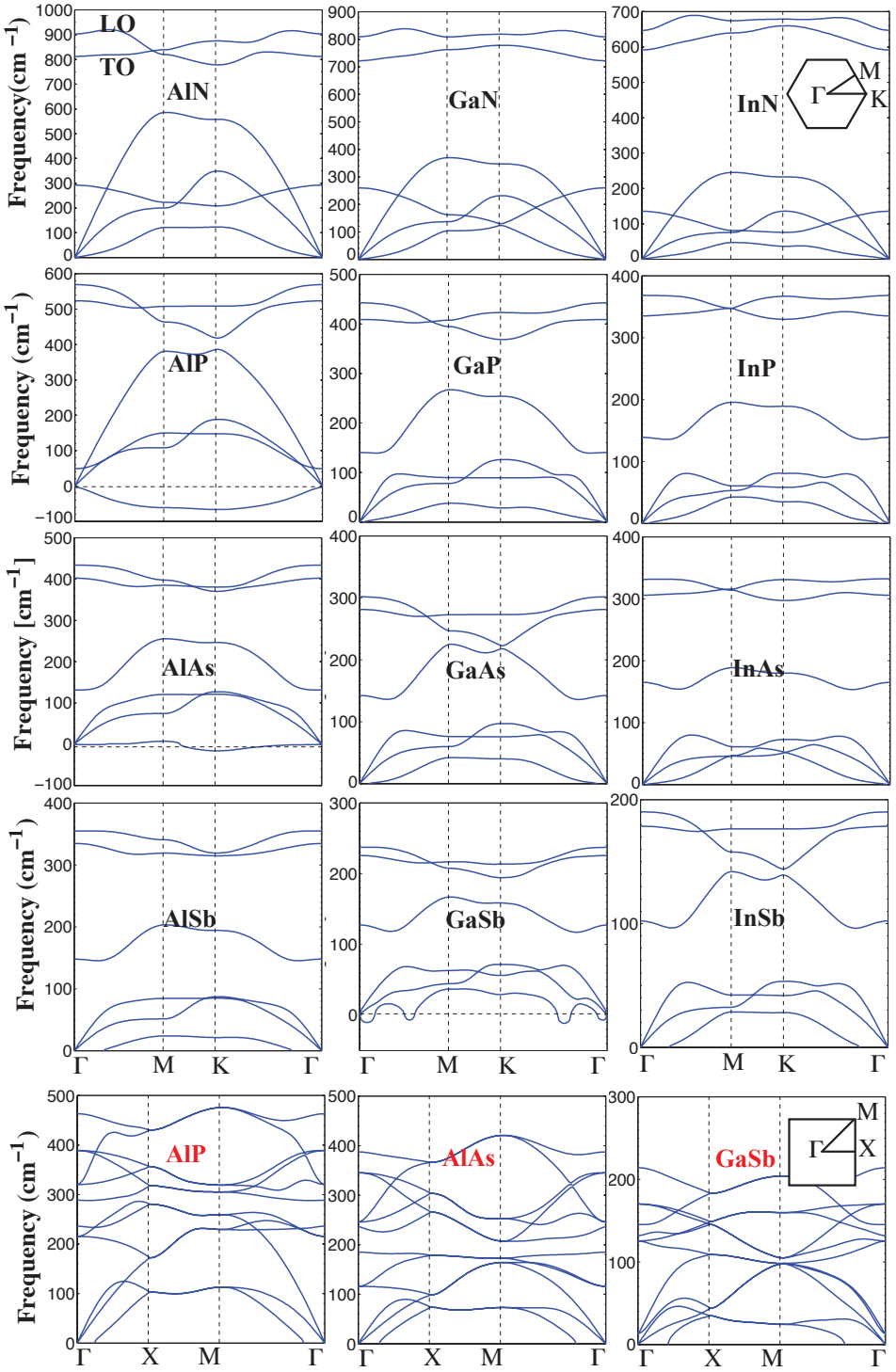

Figure 4.3: Phonon spectra of hexagonal (black labels) and tetragonal (red labels) 2D group III-V materials. The insets show the sketches of the first Brillouin Zones of the 2D hexagonal and tetragonal structures.

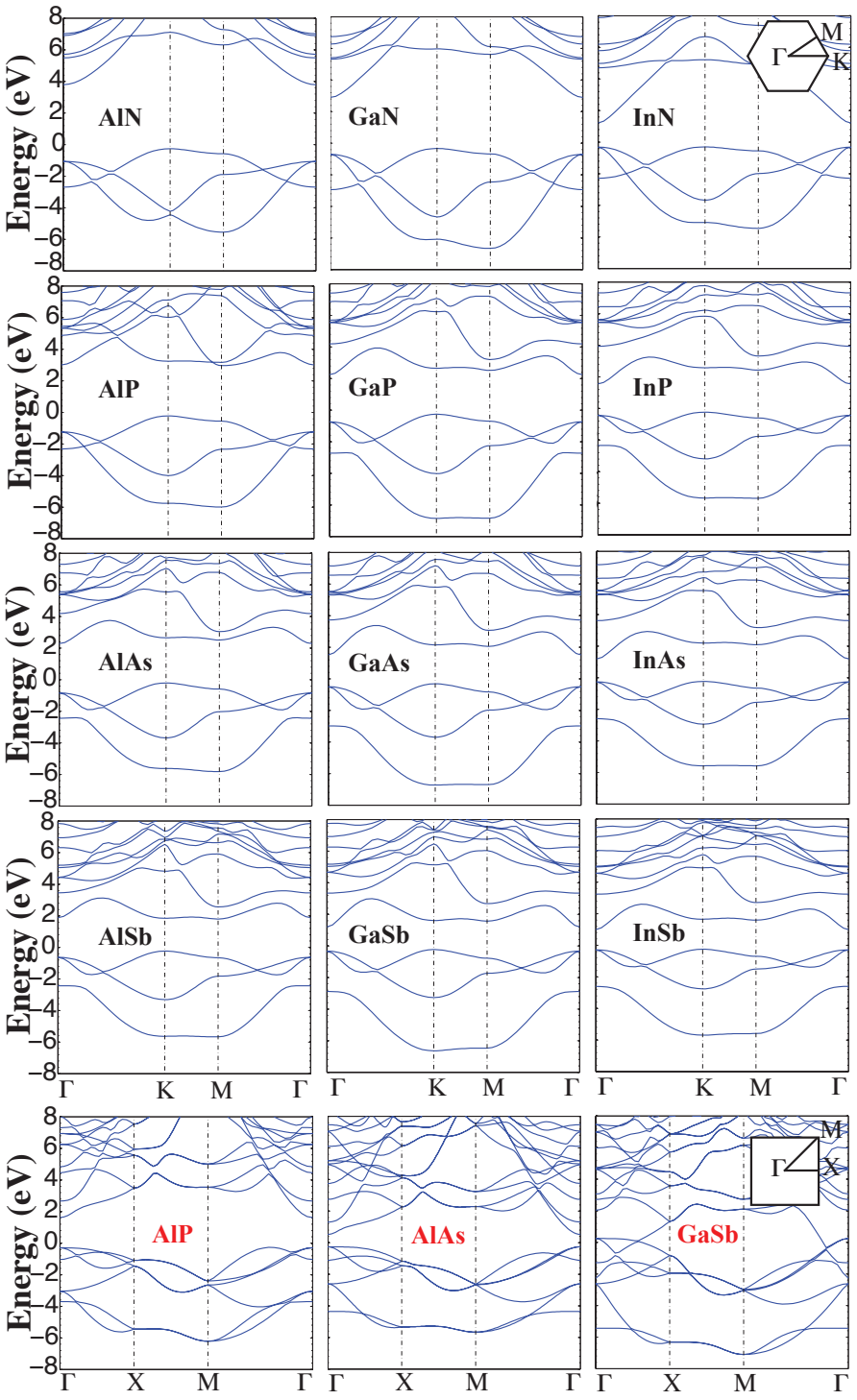

Figure 4.4: Band structures of hexagonal (black labels) and tetragonal (red labels) 2D group III-V materials calculated with the HSE06 hybrid functional.

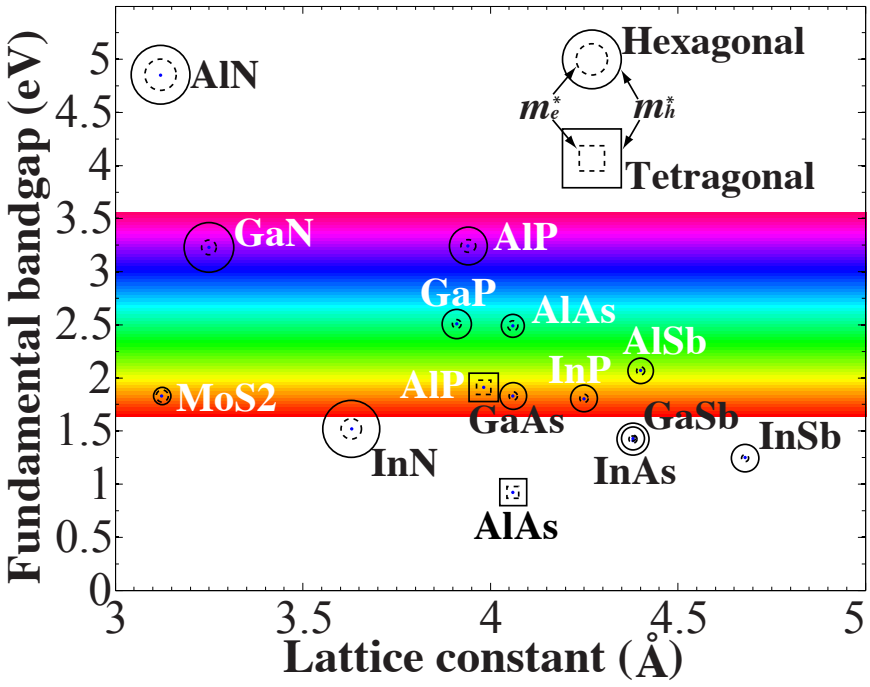

Figure 4.5: The relationship between fundamental band gaps and lattice constants of the semiconducting 2D group III-V materials. A sketch of the light spectrum is overlaid to aid visualization of the band gap size. The center of the two concentric circles or squares determines the band gap size of hexagonal and tetragonal structures, respectively. Additionally, the inner and outer radii or side length represent the electron and hole effective mass, respectively. The data of single-layer MoS_2 from Ref. [5] is shown for comparison

.

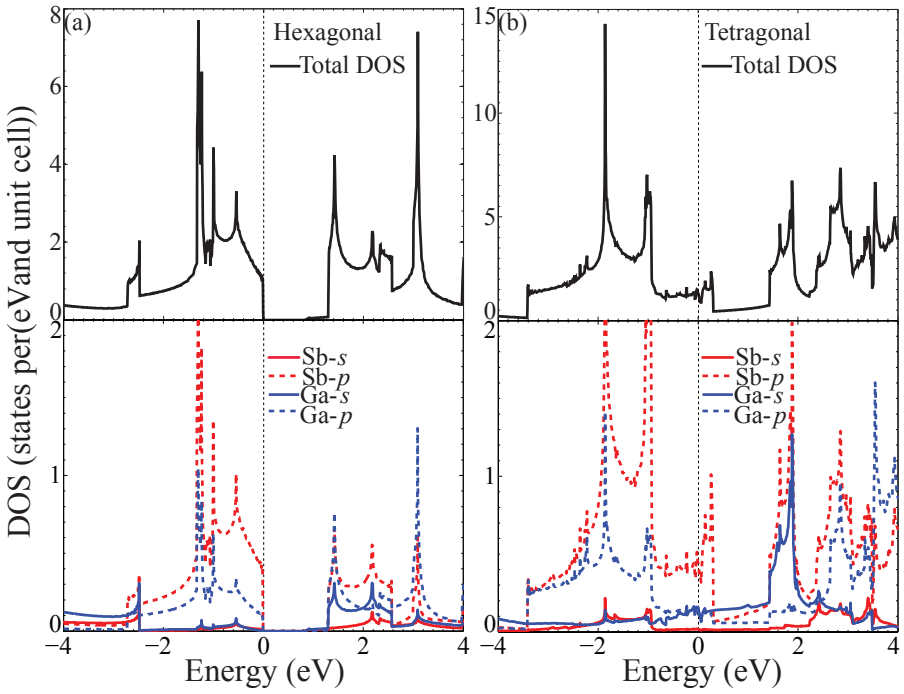

Figure 4.6: Total density of states (DOS) and projected DOS of (a) hexagonal and (b) tetragonal GaSb.

CHAPTER 5

COMPUTATIONAL DISCOVERY OF SINGLE-LAYER OXIDE SEMICONDUCTORS

5.1 Abstract[1]

The search for single-layer materials is an active research field. Using a first-principles design approach focusing on formation energy and band gap, we search the family of II-VI oxides for metastable single-layer semiconductor materials. We discover a single-layer CdO phase that exhibits a small formation energy and a direct band gap of 2.1 eV. The phonon spectrum confirms the dynamical stability of single-layer CdO. Calculations of the optical properties show a similar absorption to that of graphene. Estimates of the tunneling barrier of a graphene/CdO/graphene heterostructure, reveal that CdO might be a potential dielectric for applications of graphene in electronic devices.

5.2 Introduction

Although graphene has attractive electronic properties, the lack of a band gap limits its applications in electronic devices [73]. This limitation, however, has stimulated experimental and theoretical searches for other complementary materials exhibiting intrinsic band gaps. Experimental efforts have resulted in the emergence of various single-layer materials such as zinc oxide [15], silicon carbide [94], boron nitride [95] and transition metal dichalcogenides [32, 50, 108].

[1]Reprinted with permission from: H. L. Zhuang and R. G. Hennig, *App. Phys. Lett.*, **103** (21), 212102 (2013). Copyright 2013 by American Institute of Physics.

All these advanced materials have promising applications in nanoelectronic devices. For example, the transistors employing single-layer MoS_2 as the active element have recently been demonstrated [3].

Interestingly, the experimental synthesis of several single-layer materials was preceded by density-functional theory (DFT) studies. For instance, the computational prediction of single-layer ZnO precedes the corresponding experimental work by a year [109, 15]. This demonstrates the power of computational tools for the discovery of as-yet hypothetical materials. Recently, we predicted that boron pnictides and other III-V single-layer materials are promising semiconductors that can be stabilized by appropriate substrates [55, 19].

In this Letter, we employ DFT to explore the possibility of single-layer oxide materials in the II-VI family including BeO, CaO, MgO, ZnO, CdO, and HgO. In their three-dimensional bulk form, these oxides exhibit attractive electronic properties [105]. Thus, it is interesting to determine the effects of dimensionality reduction on their electronic properties. We investigate the energetic and dynamical stability of these oxides using their formation energies and phonon spectra. Accurate hybrid DFT calculations [97] determine the electronic properties of these hypothetical materials. Based on the predicted formation energies and band gaps, we narrow our focus to CdO, which has a low formation energy of 0.26 eV/atom compared to its bulk form and a direct band gap of 2.1 eV. This band gap lies within the region of visible light. Calculations of the optical properties show that CdO may be suitable for potential applications in photocatalysis and solar energy conversions [110]. Estimates of the tunneling barrier for a vertical graphene/CdO/graphene heterostructure illustrate the potential application of single-layer CdO as a dielectric material.

5.3 Methods

All calculations are based on DFT using the projector-augmented wave method as implemented in the Vienna *Ab initio* Simulation Package (VASP version 5.3.2) [59, 77, 78]. For the structural relaxations and energy calculations we employ the generalized gradient approximation with the Perdew-Burke-Ernzerhof (PBE) parametrization [61]. To overcome the problem of band gap underestimation in semilocal exchange-correlation functionals, the Heyd-Scuseria-Ernzerhof (HSE06) hybrid functional is used for band structure calculations [63, 97]. We have previously shown that this functional yields an accurate band gap of single-layer BN in agreement with experiment [55]. A cutoff energy of 400 eV for the plane wave basis set ensures an accuracy of the energy of 1 meV/atom. The threshold for the electronic convergence is set to an energy change of 10^{-6} eV between successive self-consistent iterations. The k-point sampling employs for the 2D materials a 120×120×1 grid for the PBE functional, a 12×12×1 grid for the more expensive HSE06 functional, and a 32×32×32 grid for the bulk systems resulting in a similar accuracy as the cutoff energy convergence. For the single-layer materials a vacuum spacing of 18 Å ensures that the interlayer interactions are negligible. We optimize all structures until the forces and stresses are converged below 1 meV/Å and 0.01 GPa, respectively.

5.4 Results

5.4.1 Structure and Formation Energies

We investigate three different structures for the single-layer oxides BeO, CaO, MgO, ZnO, CdO, and HgO: (i) a planar honeycomb hexagonal structure (ii) a buckled hexagonal structure, and (iii) a tetragonal structure [19]. In a previous study, we found that the tetragonal structure reduced the formation energy of most single-layer III-V semiconductors [19]. We compare the stability of the single-layer oxides to their bulk form by calculating the energy difference $\Delta E_{\mathrm{f}} = E_{\mathrm{2D}}/N_{\mathrm{2D}} - E_{\mathrm{3D}}/N_{\mathrm{3D}}$, where E_{2D} and E_{3D} denote the energies of the 2D and 3D bulk (wurtzite, rocksalt or orthorhombic) phases, respectively and N_{2D} and N_{3D} refer to the number of atoms in the respective unit cells. We find that due to their large ionicity and similar to single-layer BN [14], the oxide materials prefer planar hexagonal structures and that the tetragonal reconstruction is unfavorable by 0.11-0.25 eV/atom.

Tab. 5.1 shows the formation energies relative to the energy of the corresponding bulk phases, ΔE_{f}, and the lattice parameters, a_0, for the planar hexagonal oxides. BeO, ZnO, CdO, and HgO have low formation energies of 0.1-0.3 eV/atom, while the formation energies of MgO and CaO are significantly higher with values of 0.4-0.6 eV/atom. The low formation energies of BeO, ZnO, CdO, and HgO indicate that these materials could be synthesized and indeed, single-layers of both ZnO and BeO have recently been grown [15, 111]. The low formation energy of the as-yet hypothetical single-layer CdO indicates that it is a promising material for synthesis efforts.

Table 5.1: Properties of single-layer oxides, including formation energies ΔE_f relative to the bulk phases in eV/atom, lattice parameters a_0 in Å, Bader charges Q in units of electrons, and the band gap sizes E_g in eV and types. HgO reconstructd to a *Pbam* structure, denoted as HgO (*Pbam*) (see Appendix A)

	ΔE_f	a_0	Q	E_g	band gap type
BeO	0.09	2.67	1.69	6.80	Indirect
MgO	0.43	3.30	1.62	4.80	Indirect
CaO	0.56	3.74	0.55	3.81	Indirect
ZnO	0.19	3.28	1.18	3.29	Direct
CdO	0.26	3.68	1.18	2.09	Direct
HgO	0.21	3.73	0.90	0.18	Direct
HgO(*Pbam*)	0.01	7.02	0.88	1.89	Direct

We observe that the formation energies ΔE_f are similar for all post-transition metal oxides (ZnO, CdO, and HgO) and increase with atomic number for the alkaline earth metal oxides (BeO, MgO, and CaO) suggesting a change in bond character. To investigate this trend, we calculate the Bader charges, Q. The results shown in Tab. 5.1 show a decrease in ionicity for the alkaline earth metal oxides with atomic number contrary to the trend in electronegativity. The same trend and very similar Bader charges are observed for the bulk oxide phases, *e.g.* for single layer CaO $Q = 0.55e$ and for CaO in the rocksalt structure $Q = 0.53e$. This suggests an increase in covalent bond character for the alkaline earth metal oxides with atomic number, which helps explain the decrease in stability of the planar single-layer structures.

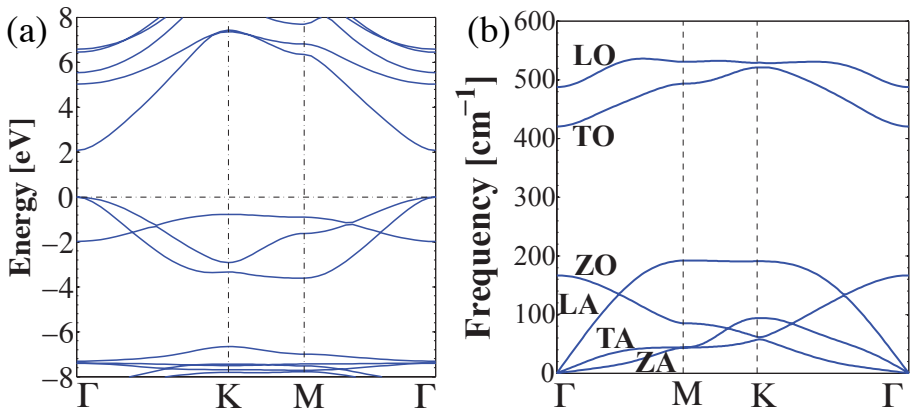

Figure 5.1: (a) Band structure of single-layer CdO calculated with the HSE06 functional. The valence-band maximum is set to zero. (b) Phonon spectrum of single-layer CdO. The lack of imaginary modes confirms the dynamical stability. The band structures and phonon spectra of single-layer BeO, MgO, ZnO, and HgO are shown in Appendix A.

5.4.2 Electronic Band Structure

Next, we screen the single-layer oxides by their electronic band gap. We calculate the band structures of the single-layer oxides using the HSE06 functional which is known to provide accurate estimates of the band gaps [63, 97]. Tab. 5.1 summarize the band gaps and band gap types of the oxides. Fig. 5.1(a) shows the band structure of single-layer CdO; the band structures of the other single-layer oxides are shown in Appendix A. The alkaline earth metal oxides exhibit indirect gaps while the post transition metal oxides all display direct band gaps. Compared with their bulk counterparts, the band gaps of CdO and HgO change from indirect to direct [112, 113], while the band gap of ZnO remains direct [105]. Additionally, the reduction in dimensionality from three to two dimensions transforms the band gap types of BeO, MgO and CaO from direct to indirect.

The 2.09 eV direct band gap exhibited by single-layer CdO is within the

range of visible light, indicating the potential usefulness of single-layer CdO for electro-optical device applications. In the following we focus on the properties of this single-layer material. Although no experimental band gap data is available for single-layer CdO, our calculated band gap of 2.09 eV is consistent with the experimental band gap of 2.16 eV measured for thin-film CdO [114]. The calculated band gap of ZnO of 3.29 eV agrees well with previous computational studies. It is consistent with a band gap of 3.37 eV reported for the same hybrid functional [115] and similar to the value of 3.58 eV obtained using the GW approximation [116], confirming the accuracy of the HSE06 functional.

5.4.3 Phonon Spectrum and Dynamical Stability

To determine the dynamical stability of single-layer CdO, we calculate its phonon spectrum by post-processing the force constants calculated with density functional perturbation theory as implemented in VASP [57, 101] and the Phonopy package [117]. Since CdO has a strong ionic character, it is important to include the long-range Coulomb forces in the force constant matrix [102, 57]. We calculate the Born effective charges and the permittivity, ϵ, and include them into the non-analytical term of the force-constant matrix.

Fig. 5.1(b) shows the phonon spectrum of single-layer CdO. No imaginary frequencies are observed, confirming the dynamical stability of single-layer CdO. Similar to graphene and other single-layer materials, the phonon spectrum consists of three optical modes and three acoustic modes. The long-range Coulomb forces in CdO, lead to a splitting of the longitudinal and transverse optical modes, denoted LO and TO, at the Γ point.

The longitudinal acoustic (LA) and transverse acoustic (TA) modes are linear functions of the wavevector q in the long-wavelength limit, *i.e.* near the Γ point. From the slopes of the TA and LA modes, we obtain the sound velocities v_s of 1.65 and 5.68 km/s for the two modes, respectively. These sound velocities are significantly smaller than the experimental values for graphene of v_s^{TA} = 14.7 km/s and v_s^{LA} = 22.2 km/s [118], and theoretical values for single-layer BN with v_s^{TA} = 9.1 km/s and v_s^{LA} = 22.0 km/s [119]. The out-of-plane acoustic mode (ZA) is quadratic in q [120]. From the quadratic relation, $\omega = \delta \cdot q^2$, we determine the δ as 1.15×10^{-6} m^2/s for single-layer CdO, much larger than for graphene with a theoretical value of $\delta = 6 \times 10^{-7}$ m^2/s [121]. The magnitude of δ determines the flexural rigidity [122]. As a result, the larger δ of CdO implies a higher energy cost to transform CdO from a single-layer form into a nanotube form.

5.4.4 Optical Properties

To further investigate the potential of single-layer CdO for opto-electronic applications, we calculate its imaginary permittivity ϵ_2 and absorbance $A(\omega)$. We calculate the imaginary permittivity $\epsilon_2(\omega)$ within the independent particle approximation using

$$\begin{aligned} \varepsilon_2 = \quad & \frac{1}{4\pi\epsilon_0}\frac{4\pi^2 e^2}{\Omega_0}\lim_{q\to 0}\sum_k 2\omega_k \delta(\epsilon_{ck+q} - \epsilon_{vk} - \hbar\omega) \\ & \times \left|\frac{1}{q} < u_{ck+q}|u_{vk} >\right|^2, \end{aligned} \tag{5.1}$$

where ϵ_0 is the vacuum permittivity, e the elementary charge, Ω_0 the volume of the cell, q the wavevector of incoming light, and ω_k is the weight for each k point [101]. The complex functions u_{ck+q} and u_{vk} present the periodic parts of

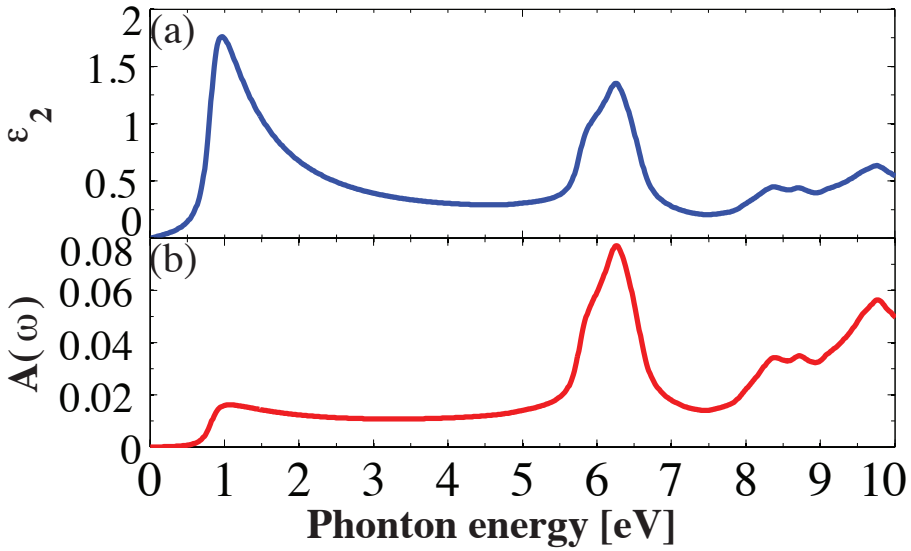

Figure 5.2: Optical properties of single-layer CdO, (a) imaginary dielectric constant ϵ_2 and (b) optical absorbance spectrum A(ω), both calculated using the PBE functional.

the conduction and valence band Bloch wavefunctions, respectively. For light with a polarization vector within the plane of single-layer CdO, the optical absorbance $A(\omega)$ is given by $A(\omega) = \omega/c \cdot L \cdot \epsilon_2$ where c is the speed of light in vacuum and L is the vacuum spacing (18 Å) between the isolated CdO layers [123].

Accurate calculations of the imaginary permittivity ϵ_2 using Eq. (5.1) require a dense k-point mesh. We use the PBE functional and a 300×300×1 k-point mesh for the integration. Fig. 5.2(a) shows ϵ_2 as a function of photon energy. Two main peaks can be observed. The first peak arises from the optical transitions between the valence and conduction bands around the Γ point, while the second peak is due to the transitions near the M point.

Fig. 5.2(b) shows the optical absorption $A(\omega)$ as a function of photon energy. As can be seen, the optical absorption $A(\omega)$ of single-layer CdO is about 2% over the energy range corresponding to visual light, slightly smaller than that of graphene of 2.3% [124]. Using the HSE06 functional associated with a 36×36×1

k-point grid yields qualitatively the same results, except that the peak positions are shifted to the larger band gaps of the HSE06 functional. The results show that CdO is nearly transparent in the optical region of the electromagnetic spectrum.

5.4.5 Single-Layer Oxides as a Dielectric Barrier

Single-layer boron nitride has recently been used as a dielectric barrier in a field-effect tunneling transistor consisting of a vertical graphene/BN/graphene heterostructure [125]. As that study points out, to improve the transistor's performance requires a dielectric with a smaller tunneling barrier. The tunneling barrier for electrons and holes in this application is given by the energy difference between the Fermi level in graphene and the conduction band minimum (CBM) or valence band maximum (VBM) of the dielectric, respectively [125]. To investigate he possibility of using the single-layer oxides as a dielectric material, we determine the band offsets and the interaction between graphene and the oxides.

We first construct a vertical heterostructure of graphene/dielectric/graphene to evaluate the interaction between the layers and to determine if the presence of graphene can stabilize the oxide layer. For CdO the stacking of 3×3 supercells of graphene with a 2×2 supercell of CdO results in a negligible misfit strain between the graphene layer and the CdO layer in the heterostructure. Since the lattice parameters of single-layer BN and graphene are closely matched, a stack of the unit cells of graphene and BN is sufficient.

To determine the character of the inter-layer interaction we perform calcula-

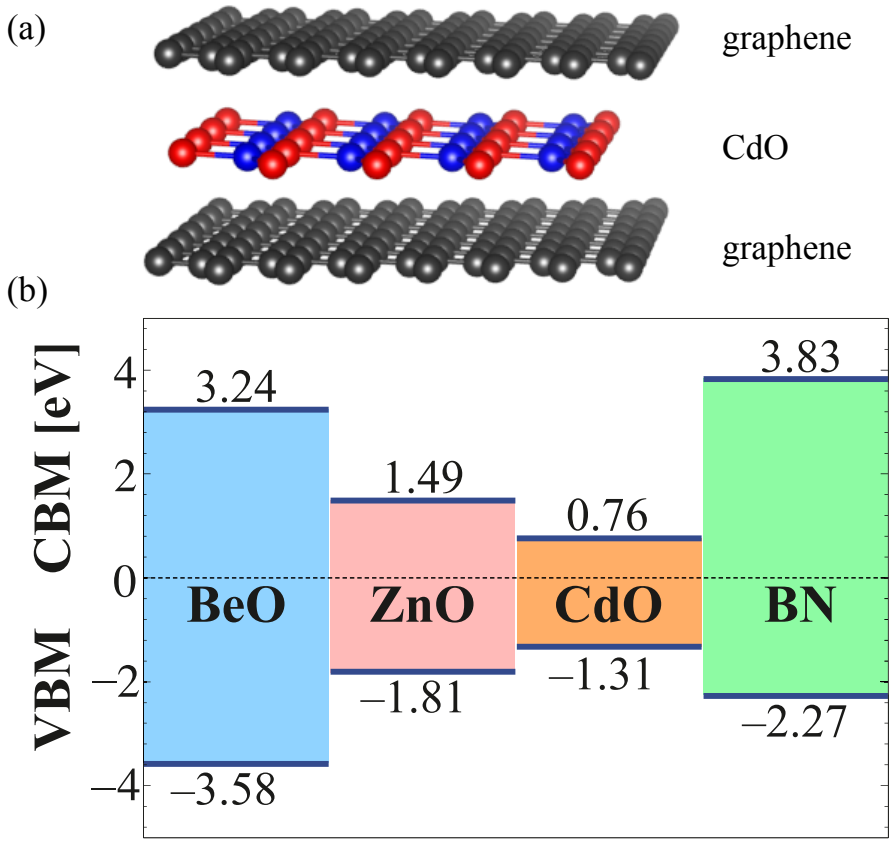

Figure 5.3: (a) An illustration of graphene/CdO/graphene heterostructure. (b) Band alignment of single-layer oxides and BN with reference to the Fermi level of graphene, which is set to zero.

tions for two different functionals, PBE and the van der Waals functional vdw-optB88 [120]. The results show that binding energy between the graphene and CdO or BN layers is dominated by van der Waals interactions. The optimal interlayer distance of the graphene/dielectric/graphene heterostructure is 3.34 Å for CdO and 3.31 Å for BN. The presence of the two graphene layers in the heterostructure also has a stabilizing effect on the CdO and BN layer. The formation energy, ΔE_{f}, is significantly reduced; for CdO by 0.2 eV/atom to 0.06 eV/atom and for BN by 0.11 eV/atom to −0.02 eV/atom, making the energy of both single-layer materials comparable to the energy of their bulk counterpart.

To determine the tunneling barrier for the different single-layer oxide dielectrics, we calculate the band offsets between the single-layer oxide materials and graphene by performing separate calculations for each of the single-layer materials using the HSE06 functional and aligning the value of the electrostatic potential in the vacuum region for the different cells [126].

Fig. 5.3 compares the band offsets in the vertical heterostructure of the single-layer oxides BeO, ZnO, and CdO with the offsets of BN. Both ZnO and CdO exhibit smaller band offsets than BN. In contrast to BN, for all three oxides the CBM offset is smaller than the VBM offset. This indicates that the oxides as dielectric layers may preferentially lead to electron tunneling compared to hole tunneling observed in the graphene/BN/graphene heterostructure [125]. The increase in stability and the reduced band offsets indicate that CdO and ZnO are promising alternative dielectric barrier for field-effect tunneling transistors, particularly for electron tunneling.

5.5 Summary

In summary, we searched for single-layer oxide materials in the family of II-VI materials and identified planar hexagonal CdO as a promising material for future synthesis efforts with a low formation energy. Hybrid functional calculations show that CdO has a direct band gap of 2.1 eV, making it a promising material for semiconductor applications. The optical absorption is comparable to that of graphene. Calculations for vertical graphene/oxide/graphene heterostructures show that the graphene layers significantly stabilizes the single-layer oxides and that single-layer ZnO and CdO present a promising alternative

to BN as a dielectric barrier for field-effect tunneling transistors. Our results provide valuable guidance for experimental synthesis efforts and potential applications of single-layer oxide materials.

CHAPTER 6

SINGLE-LAYER GROUP-III MONOCHALCOGENIDE PHOTOCATALYSTS FOR WATER SPLITTING

6.1 Abstract[1]

The recent synthesis of single-layer GaS and GaSe opens the question of stability for other single-layer group-III monochalcogenides (MX, M = Ga and In, X = S, Se, and Te) and how the dimension reduction affects the properties of these materials. Using a first-principles design approach, we determine that the single-layer group-III monochalcogenides exhibit low formation energies and are suitable for photocatalytic water splitting. First, density-functional calculations using a van der Waals functional reveal that the monochalcogenides have formation energies similar to that of single-layer MoS_2, implying the ease of mechanically extracting single-layer monochalcogenides from their layered bulk counterparts. Next, calculations using a hybrid density functional and the quasiparticle many-body G_0W_0 approximation determine the conduction and valence band edge positions. Comparing the band edge positions with the redox potentials of water, shows that single-layer monochalcogenides are potential photocatalysts for water splitting. Moreover, the band gaps, band edge positions, and the optical absorption of the single-layer monochalcogenides can be tuned by biaxial strain to increase the efficiency of solar energy conversion. Finally, calculations of the enthalpy of solvation of the single-layer monochalcogenides suggest their stability in aqueous solution.

[1]Reprinted with permission from: H. L. Zhuang, and R. G. Hennig, *Chem. Mater.,* **25** (15), 3232-3238 (2013).

6.2 Introduction

Group-III monochalcogenides (MX, M = Ga and In, X = S, Se, and Te) have been extensively studied due to their potential applications in fields such as solar energy conversion [127, 128]. For example, solar cells based on InSe have achieved efficiencies as high as 10.9% [127]. The ultimate dimension reduction of three-dimensional MX leads to single-layer MX, which consist of four sublayers stacked in the sequence X-M-M-X, as illustrated in Fig. 6.1(a). Experimental efforts have recently been undertaken to fabricate these MX in single-layer form and single-layer GaS and GaSe sheets have already successfully been synthesized [129, 130, 131].

The reduction of a materials' dimension from 3D to 2D frequently results in novel electronic and mechanical properties. An example for electronic properties is given by recent experimental studies that have shown that single-layer MoS_2 exhibits a wider band gap than its 3D bulk counterpart [86, 132]. For mechanical properties, 2D materials are often easier to strain. For instance, pristine graphene can withstand strains of up to 25% [30], which is significantly larger than that of graphite with a maximum elastic strain of 0.1% [133]. In view of these unusual 2D properties, it is desirable to determine the potential of single-layer MX materials for solar energy conversion and photocatalysis.

Hydrogen generation by photocatalytic water splitting presents a promising method for solar energy conversion [110]. Fig. 6.1(b) illustrates the working principle of water splitting [134]. When sun light shines on a semiconductor, the photons can generate pairs of electrons and holes. The excited electrons can then take part in the hydrogen reduction reaction generating H_2: $2H^+$ +

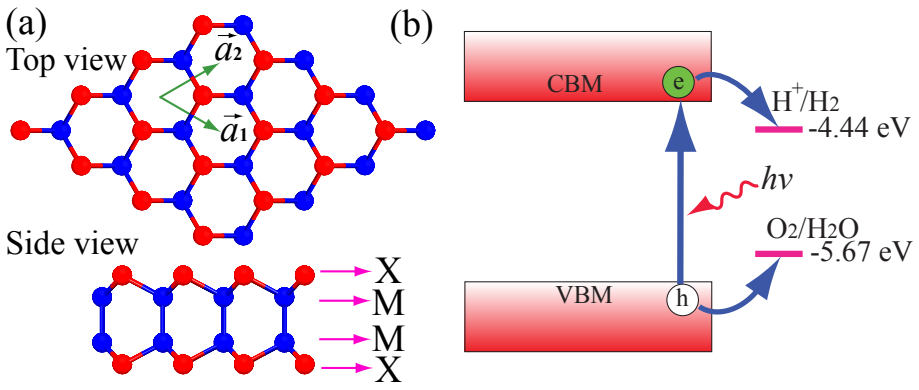

Figure 6.1: (a) Top and side views of the single-layer MX structure. (b) Illustration of photocatalytic water splitting. The band edge positions of a photocatalyst must be aligned with reference to the redox potentials for water splitting.

$2e^- \rightarrow H_2$. The holes, on the other hand, participate in the oxidation reaction to generate O_2: $H_2O + 2h^+ \rightarrow \frac{1}{2}O_2 + 2H^+$. In order for a semiconductor to facilitate photocatalytic water-splitting, two conditions need to be satisfied. First, the band gap of the semiconductor must exceed the reaction free energy of water splitting of 1.23 eV [135]. Second, a suitable photocatalyst material requires that its conduction band minimum (CBM) energy is higher than the reduction potential of H^+/H_2 and its valence band maximum (VBM) energy lower than the oxidation potential of O_2/H_2O.

In addition to fulfilling the above criteria on their electronic structure, the 2D MX studied in this work, exhibit another advantage for applications as photocatalysts. The 2D nature of these materials means that they maximize their surface area available for water splitting while at the same time minimizing the distance that the generated electrons and holes have to migrate, reducing the possibility of electron-hole recombination and potentially enhancing their catalytic performance [134].

This work focuses on the exploration of single-layer MX as photocatalysts for water splitting to generate hydrogen. We first determine the stability of the materials, followed by the study of the electronic structures of single-layer MX using accurate hybrid density functional and many-body quasiparticle calculations. Next, we study how mechanical strains can be used to tune the band gap, band edge positions, and the optical absorption of the MX to increase the potential efficiency of solar energy conversion. Finally, we address the question of stability of single-layer monochalcogenides in aqueous solution by calculating the enthalpy of solvation and comparing the results to related materials with known solubility.

6.3 Methods

We perform density-functional theory (DFT) calculations using the projector augmented wave method as implemented in the plane-wave code VASP [59, 77, 78]. For the structural relaxations we employ both the PBE generalized gradient approximation (GGA) and the Heyd-Scuseria-Ernzerhof (HSE06) hybrid functional [61, 63]. A cutoff energy of 400 eV for the plane wave basis set is used throughout all calculations and ensures an accuracy of the energy of 1 meV/atom. The k-point sampling uses the Monkhorst-Pack scheme [81] and employs for the single-layer materials a $48 \times 48 \times 1$ mesh for the PBE functional and an $18 \times 18 \times 1$ mesh for the more expensive HSE06 and G_0W_0 calculations. For the single-layer materials a vacuum spacing of 18 Å ensures that the interactions between the layers are negligible.

We define the formation energy E_f of the single-layer MX as

$$E_\mathrm{f} = E_\mathrm{2D}/N_\mathrm{3D} - E_\mathrm{3D}/N_\mathrm{3D}, \tag{6.1}$$

where E_2D and E_3D are the energies of the single-layer and bulk MX, respectively. N_2D and N_3D denote the numbers of atoms in the respective unit cells. The single-layer MX exhibit a hexagonal structures with space group $P\bar{6}m2$ as illustrated in Fig. 6.1. The 3D bulk structures of GaS, GaSe, GaTe, and InSe possess the same structure with space group $P6_3/mmc$, while InS and InTe have structures with space groups $Pnnm$ and $I4/mcm$, respectively [100]. To accurately account for dispersion interactions, we use the vdw-optB88 van der Waals functional for the calculation of the formation energies [120].

We determine the band edge positions E_CBM and E_VBM relative to the vacuum level using the HSE06 and the G_0W_0 method by aligning the energy levels for the different material such that their vacuum levels are set to zero. For the G_0W_0 method we follow the method by Toroker *et al.* [136], and determine the CBM and VBM levels from the band gap center energy E_BGC of the HSE06 functional and the quasiparticle band gap energy E_g^QP as

$$E_\mathrm{CBM/VBM}^\mathrm{QP} = E_\mathrm{BGC}^\mathrm{HSE06} \pm \frac{1}{2} E_\mathrm{g}^\mathrm{QP} \tag{6.2}$$

The validity of this approach relies on the assumption that, in contrast to the band gaps, the band gap center energies are insensitive to the choice of exchange-correlation functional. As shown below, the band gap center energies of the PBE and HSE06 functional for the MX differ by merely 0.01-0.14 eV, verifying this assumption. Further details about the calculation of the band gap center energies are given in Appendix B. We use the PBE wave functions as the starting point for the G_0W_0 calculations. Moreover, we use 64 bands and 96 frequency points, ensuring that the quasiparticle band gaps E_g^QP are converged to

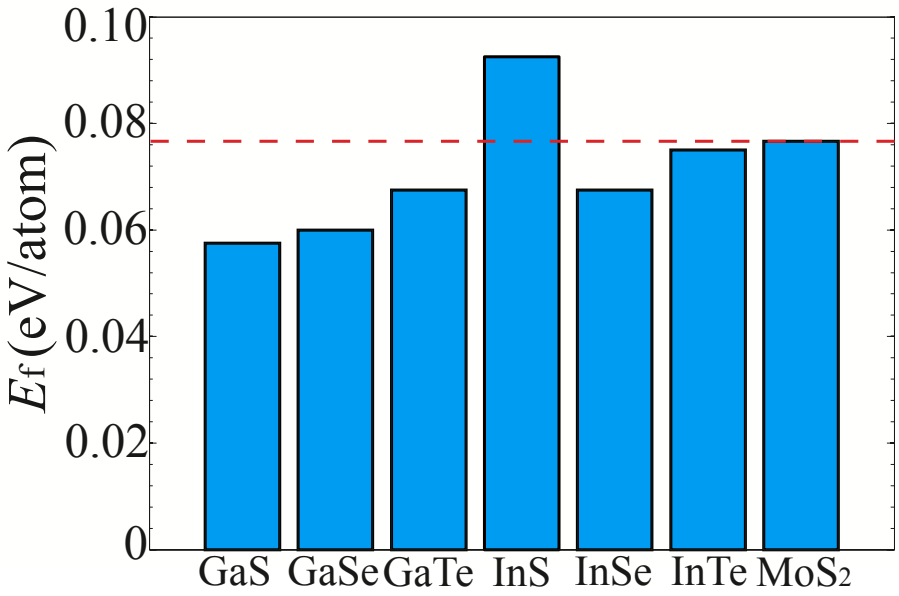

Figure 6.2: Formation energies of single-layer MX and MoS_2. The low formation energies indicate that the MX, similar to MoS_2, could be synthesized by mechanical exfoliation.

1 meV.

For the water splitting reaction, the redox potentials depend on the pH value [137]. Here, we adopt the commonly used value of $E^{\text{red}}_{\text{H}^+/\text{H}_2} = -4.44\,\text{eV} + \text{pH} \cdot 0.059\,\text{eV}$ for the standard reduction potential for H^+/H_2 [137, 138, 139]. Correspondingly, the oxidation potential for $\text{O}_2/\text{H}_2\text{O}$ is $E^{\text{ox}}_{\text{O}_2/\text{H}_2\text{O}} = -5.67\,\text{eV} + \text{pH} \cdot 0.059\,\text{eV}$.

To evaluate the optical properties of single-layer MX, we calculate the optical absorbance $A(\omega)$ given by $A(\omega) = \epsilon_2 L\omega/c$, where ϵ_2 is the imaginary permittivity calculated within the independent particle approximation, L is the vacuum spacing of 18 Å between the isolated MX layers, and c is the speed of light in vacuum [140]. Accurate calculations of the imaginary permittivity ϵ_2 require a dense k-point mesh. We use the PBE functional and a $300 \times 300 \times 1$ k-point mesh for the calculations.

To determine how easy the MX can be strained and how strain affects the electronic and optical properties we perform DFT calculations applying a biaxial strain ϵ to the materials. We calculate the elastic modulus C, an important measurable property of single-layer materials such as graphene and MoS_2 [47, 30], using

$$C = \frac{1}{A_0} \frac{\partial^2 E}{\partial \epsilon^2}, \tag{6.3}$$

where A_0 is the equilibrium area of the simulation cell and E is the energy at strain ϵ.

6.4 Results

6.4.1 Structural Properties

Table 6.1 reports the structural parameters of the single-layer MX calculated with both the PBE and HSE06 functionals. Our calculated structural parameters agree well with previous studies of GaS and MoS_2 [141, 83]. The comparison of PBE and HSE06 lattice parameters reveals an interesting trend that the latter results are smaller than the former ones. The HSE06 functional includes 25% of exact exchange for short distances, which reduces the self-interaction error in the PBE functional and improves the agreement with experimental lattice parameters [142].

Figure 6.2 shows that the formation energies of the single-layer MX materials are comparable or only slightly larger than the formation energy of single-layer MoS_2, which has been successfully synthesized by micro-mechanical exfoliation [38]. Therefore, we expect that the single-layer MX can also be easily syn-

thesized by cleaving their 3D counterparts. Indeed single-layer GaS and GaSe have already successfully been synthesized [129, 130, 131].

Table 6.1 shows the elastic moduli of single-layer MX and MoS_2 calculated with the PBE and HSE06 functionals. The elastic moduli of the MX are significantly smaller than that of MoS_2, implying that single-layer MX are softer and can be easier strained than MoS_2. Moreover, the moduli decrease in the Ga and In monochalcogenides when the chalcogen atoms varies from S to Te. The same trend of elastic modulus is observed in the families of molybdenum and tungsten dichalcogenides [143]. Although no experimental elastic moduli are available for MX, our calculated values for MoS_2 are in excellent agreement with the experimental result [47], indicating the accuracy of DFT for these single-layer materials.

Interestingly, the elastic moduli from HSE06 are systematically larger than the ones from PBE. Notably, the elastic modulus of single-layer MoS_2 of 189 N/m obtained from the HSE06 functional is in excellent agreement with the experimental mean value of 180 N/m [47]. Similar to the difference between LDA and GGA functionals, the larger elastic moduli are likely due to the smaller lattice parameters predicted by the HSE06 functional [142].

6.4.2 Electronic Properties

Figure 6.3 shows the band structures of single-layer MX obtained from the HSE06 functional. As can be seen, all the MX materials display indirect band gaps with the VBM located between the Γ and M points. The CBM for these materials, however, occurs at two different positions. For GaS and GaTe, the CBM

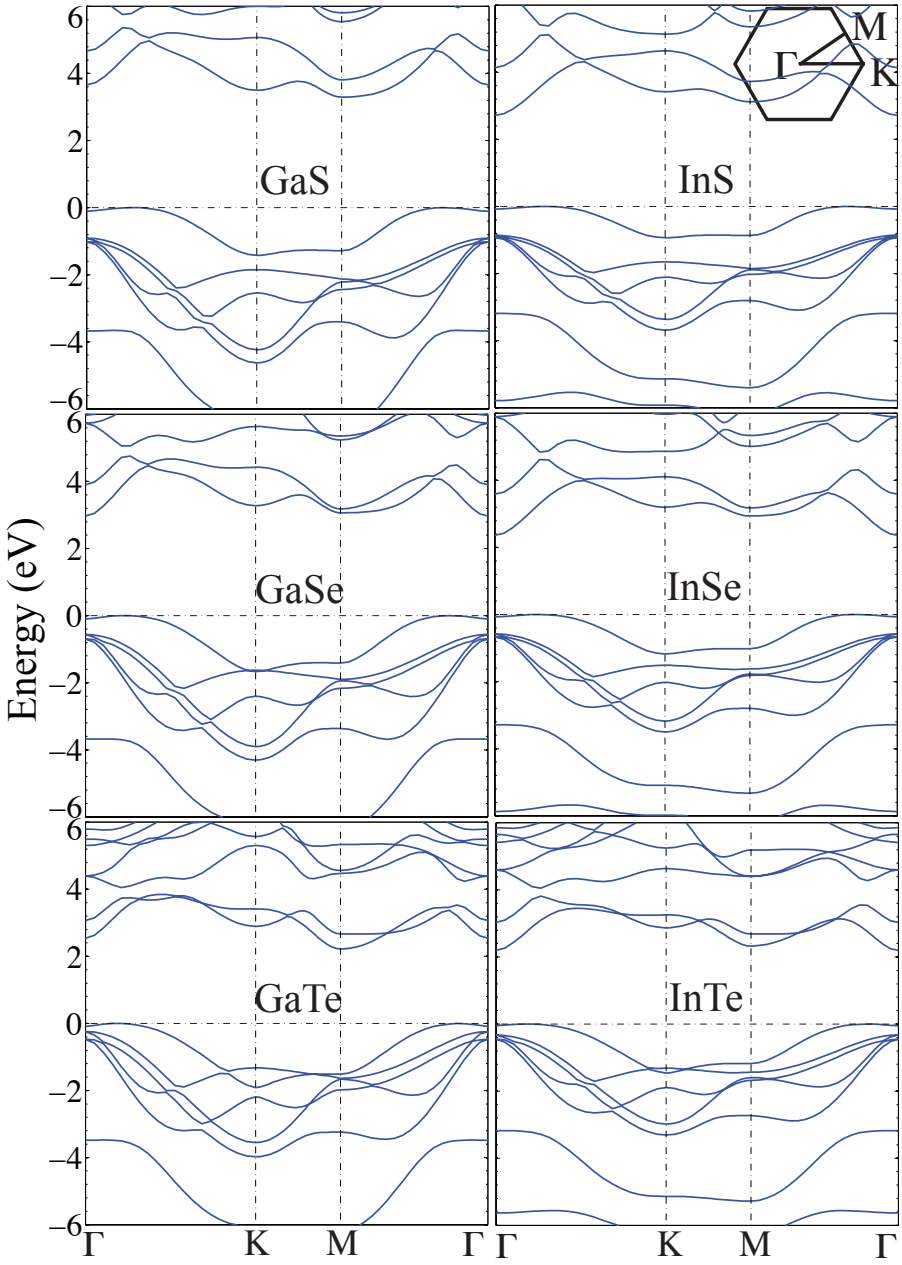

Figure 6.3: Band structures of single-layer MX calculated with the HSE06 functional. The valence band maximum is set to zero. The inset illustrates the first Brillouin zone of the single-layer hexagonal MX structures.

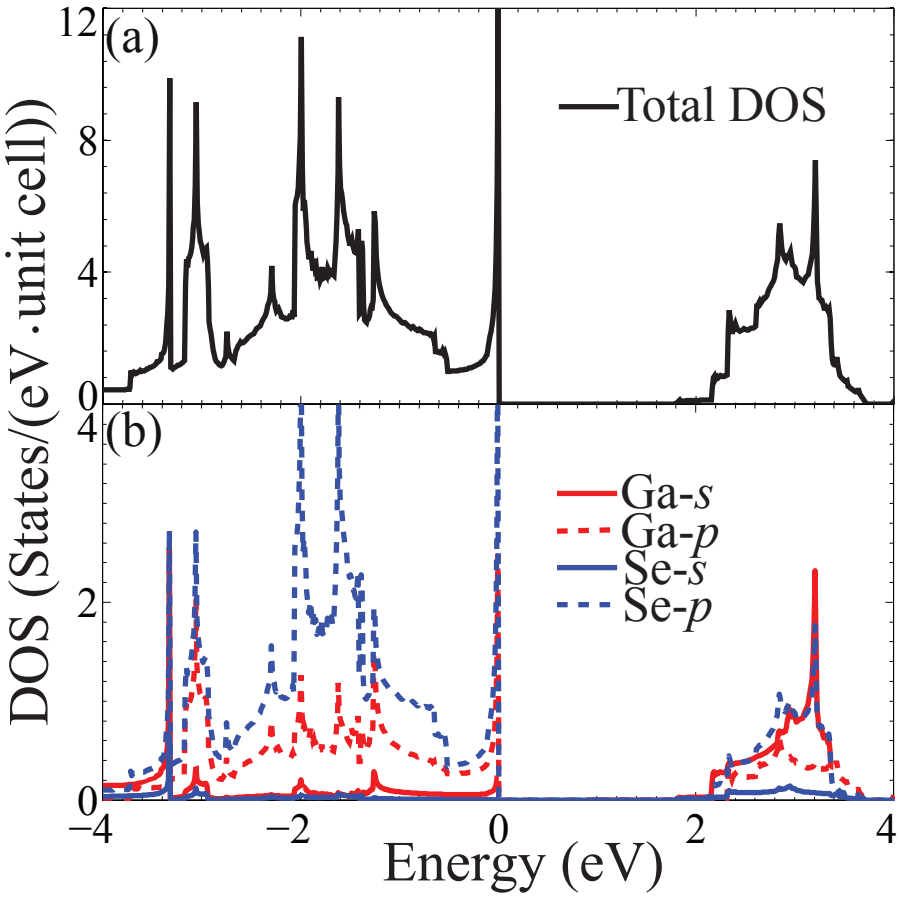

Figure 6.4: (a) Total and (b) projected density of states of GaSe.

is at the M point, while for the other four materials it is at the Γ point. For most MX, the direct band gaps are close in size and position to the direct band gaps with a maximum energy difference of 0.1 eV. We expect that the direct interband transitions at the Γ point improve the optical absorption of these materials, since no phonons are required for this optical transition to proceed.

To understand the bonding characteristics of single-layer MX, we analyze their total and projected density of states, TDOS and PDOS, respectively. Figure 6.4(a) shows that the TDOS of GaSe exhibits multiple van Hove singularities over the entire energy range, which is consistent with the 2D nature of a single-layer material [102]. The corresponding PDOS of GaSe in Fig. 6.4(b) illustrates

that the valence band of GaSe is dominated Ga and Se $4p$ states, indicating hybridization between those orbitals and a covalent bond character, which is typical for layered metal chalcogenides [144].

Table 6.2 summarizes the band gaps of single-layer MX and MoS_2 calculated with the PBE and HSE06 functionals and the G_0W_0 method. With all three methods, we observe a decrease in the band gaps for both the Ga and In monochalcogenide families as the chalcogen species changes from S to Te, which is due to the decrease in ionicity [145]. The PBE functional as usual underestimates the band gaps [146] and predicts gaps 0.6 to 1.4 eV smaller than the HSE06 functional and the G_0W_0 approximation. The HSE06 and G_0W_0 methods predict similar band gaps with the G_0W_0 band gaps being about 0.4 to 0.6 eV larger. There is no experimental band gap data for single-layer MX. However, our HSE06 and quasiparticle band gaps of MoS_2 agree well with previous experimental and theoretical studies, indicating the accuracy of these methods [86, 83, 147]. Comparison with experimental data for the single layer-materials BN, fluorographene, and MoS_2 show that the GW method in these related systems overestimates the band gap [83]. The HSE06 band gap on the other hand, *e.g.*, for single-layer BN, is close to the experimental value [55, 82]. Therefore, in the following discussions, we focus on the results for the HSE06 functional.

We observe that the HSE06 band gaps reported in Tab. 6.2 for all MX except GaS fall within the visible spectrum. This indicates that these materials could harvest a significant fraction of solar light. To confirm whether they are suitable for water splitting, we need to determine the alignment of the CBM and VBM energies with the redox potentials of water.

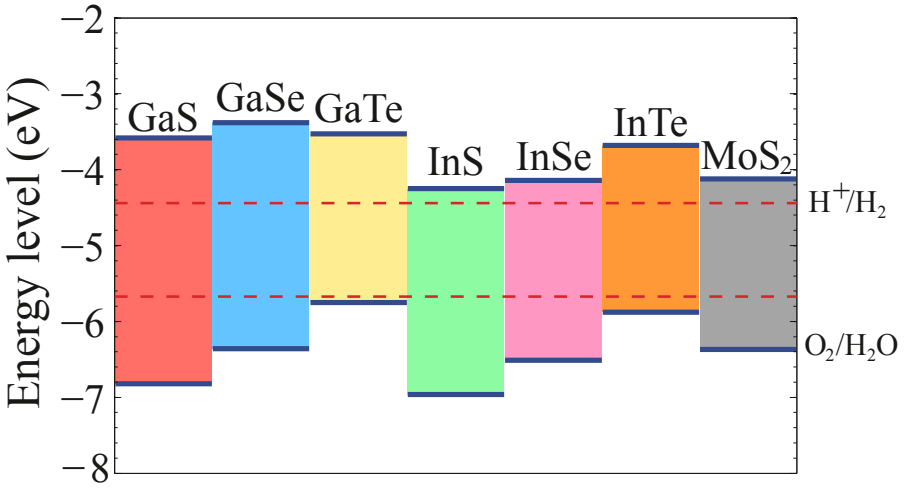

Figure 6.5: Band edge positions of single-layer MX relative to the vacuum level at zero strain calculated with the HSE06 functional. The band edge positions of single-layer MoS_2 and the standard redox potentials for water splitting at pH = 0 are shown for comparison.

6.4.3 Photocatalytic Water Splitting

Figure 6.5 compares the CBM and VBM energy levels with the redox potentials of water splitting and Tab. 6.2 lists the values of the band edge positions relative to the vacuum level for the single-layer MX. The band edge positions of MoS_2 are shown for comparison. All the MX as well as MoS_2 have band edges located at energetically favorable positions for water splitting, suggesting that all of these seven single-layer materials are suitable photocatalysts. The same results are obtained from the G_0W_0 method, as can be seen from Tab. 6.2. Although there is no available experimental data, our prediction of single-layer MoS_2 as a potential photocatalyst is consistent with recent theoretical work [143]. Note that even using the experimental band gap of 1.9 eV for MoS_2 [86], the resulting E_{VBM} and E_{CBM} are −4.05 eV and −6.05 eV, respectively. Therefore, the conclusion that single-layer MoS_2 is a suitable photocatalyst for water splitting remains

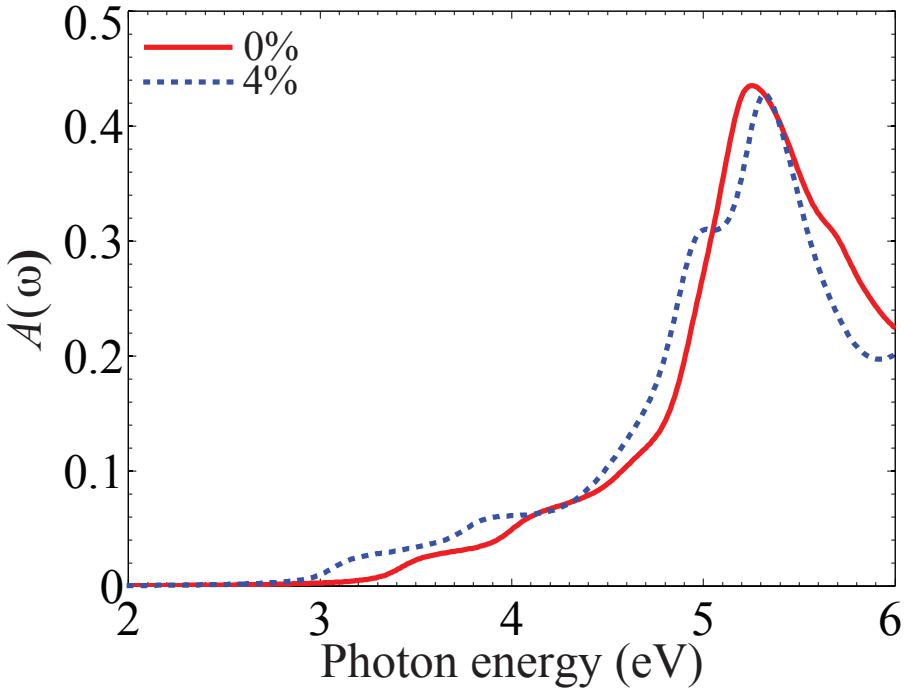

Figure 6.6: Optical absorbance spectrum $A(\omega)$ of single-layer GaSe at the strains of 0% and 4%. $A(\omega)$ is calculated using the PBE functional followed by a rigid energy shift to take into account of the band gap underestimation of the PBE functional.

the same.

The redox potentials for water increase with pH by $\mathrm{pH} \cdot 0.059\,\mathrm{eV}$, shifting the water's redox energy levels in Fig. 6.5 upwards [137]. This shift is beneficial to some MX, such as GaTe and InTe, since their oxidation energy levels at pH= 0 are too close to the oxidation potential for O_2/H_2O. However, for some MX large pH values make the reduction reactions energetically unfavorable. For example, the maximum acceptable pH value for InS is 3.2.

In addition to an appropriate band gap and a suitable band alignment, it is important that a photocatalytic material absorbs a significant fraction of the incoming light. Figure 6.6 shows the optical absorption $A(\omega)$ of single-layer GaSe

as a function of photon energy ω. Following a previous study on TiO_2 [148], we compensate for the band gap underestimation of the PBE functional by a rigid shift of the absorption curves upwards in energy by 1.1 eV, *i.e.* the difference between the HSE06 and PBE band gaps. Unlike graphene which shows a constant absorption of 2.3% in the range of visible light [140], the optical absorption of GaSe increases significantly with photon energy over the range of visible light and reaches a maximum absorption of 43% at 5.2 eV. This absorption peak arises from the optical transitions between the valence and conduction bands around the K point. Because of the similarities in electronic structure between all the MX, we expect that the other MX exhibit a comparable optical absorption as GaSe. The high optical absorption indicates that the single-layer MX are promising candidates for photocatalytic water splitting.

6.4.4 Band Edge Tuning by Strain

Although all single-layer MX have suitable band edge positions with reference to the water splitting redox levels, there arise two practical concerns related to the efficiency of solar energy conversion. First, the band gaps of some MX, *e.g.*, GaS and GaSe, are too large to absorb a significant fraction of the solar spectrum, reducing their potential conversion efficiency. $SrTiO_3$, another promising photocatalyst, exhibits a similar problem of a wide band gap of 3.2 eV, leading to efficiencies of less than 1% [149]. Second, the CBM and VBM of some MX are too close to the redox potentials of water. The CBM of InS is one such example. A useful method to address these two concerns is through band gap engineering by applying strains [133]. In practice, these strains could potentially be realized by epitaxial growth on suitable substrates.

To explore the effects of strain on the band gaps and band edge positions of single-layer MX, we apply biaxial strains in the range from −4% to +4%. We apply the HSE06 functional to relax atomic positions at each biaxial strain and obtain the corresponding CBM and VBM from the relaxed configurations. Figure 6.7 shows the variations of the CBM and VBM levels of the single-layer MX with strain. Over large regions of strain, the CBM and VBM level depend linearly on strain. However, for most materials we observe that the slope changes abruptly at certain strains. This is due to a change of band edge positions. For example, the CBM of GaSe at −4% strain occurs at the K point while at +4% strain, the CBM occurs at the Γ point instead. The corresponding band structures of GaSe at these two strains are shown in Appendix B.

Transitions from an indirect to a direct band gap and changes in the electronic structure under strain could enhance the optical absorption of the single-layer MX. Figure 6.6 compares the optical absorption of single-layer GaSe at zero strain and a strain of +4%. The tensile strain increases the optical absorption significantly over the entire energy range of visible light.

Figure 6.7 provides useful guidance for tuning the band gaps and CBM and VBM levels of single-layer MX in order to maximize the efficiency of solar energy conversion. For the GaX monochalcogenides, tensile strains are generally preferred. Tensile strains not only reduce the band gaps but also keep both the VBM and CBM at suitable energy levels. For example for GaS, a biaxial tensile strain of +4% reduces the band gap to 2.62 eV, right within the visible spectrum. For InX monochalcogenides, on the other hand, compressive strains are suggested, which increase the band gaps slightly but more importantly make the band edge positions more favorable. In contrast, tensile strains reduce the CBM

of InS and InSe below the reduction potential of H^+/H_2 making it unsuitable for water splitting at high tensile strains.

6.4.5 Stability in Water

To assess the stability of single-layer gallium and indium monochalcogenides in water, we estimate their solubility by calculating the enthalpy of solvation ΔH_{solv}. The enthalpy of solvation is determined as the sum of the cohesive energy and the energy change from gas atoms to hydrated ions. For the chalcogenides we also consider the possibility of ion association decreasing the enthalpy of solvation. Details are provided in Appendix B.

As a benchmark test of our method, Fig. 6.8(a) compares the calculated enthalpies of solvation ΔH_{solv} of five poorly soluble compounds (three silver halides and two sulfides) with experimental data [150, 151, 152]. All the experimental values are obtained from the solubility product and include an entropic term that is expected to be small. For the silver halides the calculated enthalpies correlate well with experimental data for the solubility. A similar agreement is observed for the sulfides CuS and CdS when ion association is taken into account. The difference between the experimental Gibbs energy of solvation ΔG_{solv} is nearly system independent indicating a similar entropy of solvation.

Figure 6.8(b) shows the calculated enthalpies of solvation ΔH_{solv} of the single-layer gallium and indium monochalcogenides considering either isolated ions or ion association. The solvation enthalpies are all larger than 200 kJ/mol. Comparison with the solubility of the known compounds shown in Fig. 6.8(a) indicates that the solubility of the single-layer monochalcogenides are below

10^{-16} mol/100g water, implying their stability in water.

6.5 Summary

We performed a systematic search for potential photocatalysts in the family of group-III monochalcogenides. We find that the formation energies of the single-layer MX are low and comparable to those of single-layer MoS_2 which has been successfully synthesized. Our calculations of the band gaps and band edge positions using accurate hybrid functional and quasiparticle methods predict that the MX are potentially suitable photocatalysts for water splitting. We show that the MX absorb a significant amount of light in the visible range. Additionally, we show that mechanical strains can be applied to tune the band gaps, band edge positions, and optical absorption for a better match with the solar spectrum and the redox potentials of water in order to increase the efficiency of solar energy conversion. Finally, we predict high enthalpies of solvation for the single-layer monochalcogenides, indicating that they are insoluble in water. These results provide valuable guidance for synthesis efforts of single-layer monochalcogenide materials and for their potential applications as photocatalysts.

Table 6.1: Structural parameters and elastic modulus of single-layer MX and MoS_2 calculated with the PBE and HSE06 functionals. The parameters include the lattice parameter a_0, the M-M bond length b_{M-X}, X-X bond length b_{X-X} in units of Å, and the X-M-M bond angle θ_{X-M-M} in units of degrees. The elastic modulus C is in units of N/m.

	a_0^{PBE}	a_0^{HSE06}	b_{M-M}^{PBE}	b_{M-M}^{HSE06}	b_{M-X}^{PBE}	b_{M-X}^{HSE06}	θ_{X-M-M}^{PBE}	θ_{X-M-M}^{HSE06}	C^{PBE}	C^{HSE06}
GaS	3.64	3.58	2.48	2.45	2.37	2.33	117.49	117.47	98	120
GaSe	3.82	3.75	2.47	2.44	2.50	2.46	118.12	118.17	79	104
GaTe	4.14	4.06	2.47	2.44	2.71	2.66	118.14	118.21	66	84
InS	3.94	3.88	2.82	2.78	2.57	2.53	117.61	117.68	73	89
InSe	4.09	4.02	2.82	2.77	2.69	2.65	118.54	118.60	60	76
InTe	4.39	4.31	2.81	2.77	2.89	2.84	118.81	118.91	39	63
			b_{Mo-S}^{PBE}	b_{Mo-S}^{HSE06}	b_{S-S}^{PBE}	b_{S-S}^{HSE06}	θ_{S-Mo-S}^{PBE}	θ_{S-Mo-S}^{HSE06}		
MoS_2	3.18	3.15	2.41	2.39	3.13	3.11	80.80	81.02	165	189

Table 6.2: band gaps E_g, band gap centers E_{BGC}, and band edge positions E_{VBM} and E_{CBM} of single-layer MX obtained from different methods. All energies are in units of eV. Data of single-layer MoS_2 are shown for comparison.

	E_g^{PBE}	E_g^{HSE06}	E_g^{QP}	E_{BGC}^{PBE}	E_{BGC}^{HSE06}	E_{CBM}^{HSE06}	E_{CBM}^{QP}	E_{VBM}^{HSE06}	E_{VBM}^{QP}
GaS	2.48	3.19	3.82	–5.07	–5.17	–3.58	–3.26	–6.77	–7.08
GaSe	1.91	2.98	3.34	–4.92	–4.87	–3.38	–3.20	–6.36	–6.54
GaTe	1.66	2.22	2.84	–4.52	–4.64	–3.53	–3.22	–5.75	–6.06
InS	1.74	2.71	3.16	–5.55	–5.60	–4.25	–4.02	–6.96	–7.18
InSe	1.49	2.37	2.83	–5.30	–5.32	–4.14	–3.91	–6.51	–6.74
InTe	1.40	2.20	2.69	–4.79	–4.78	–3.68	–3.44	–5.88	–6.13
MoS_2	1.68	2.25	2.36	–5.10	–5.24	–4.12	–4.06	–6.37	–6.42

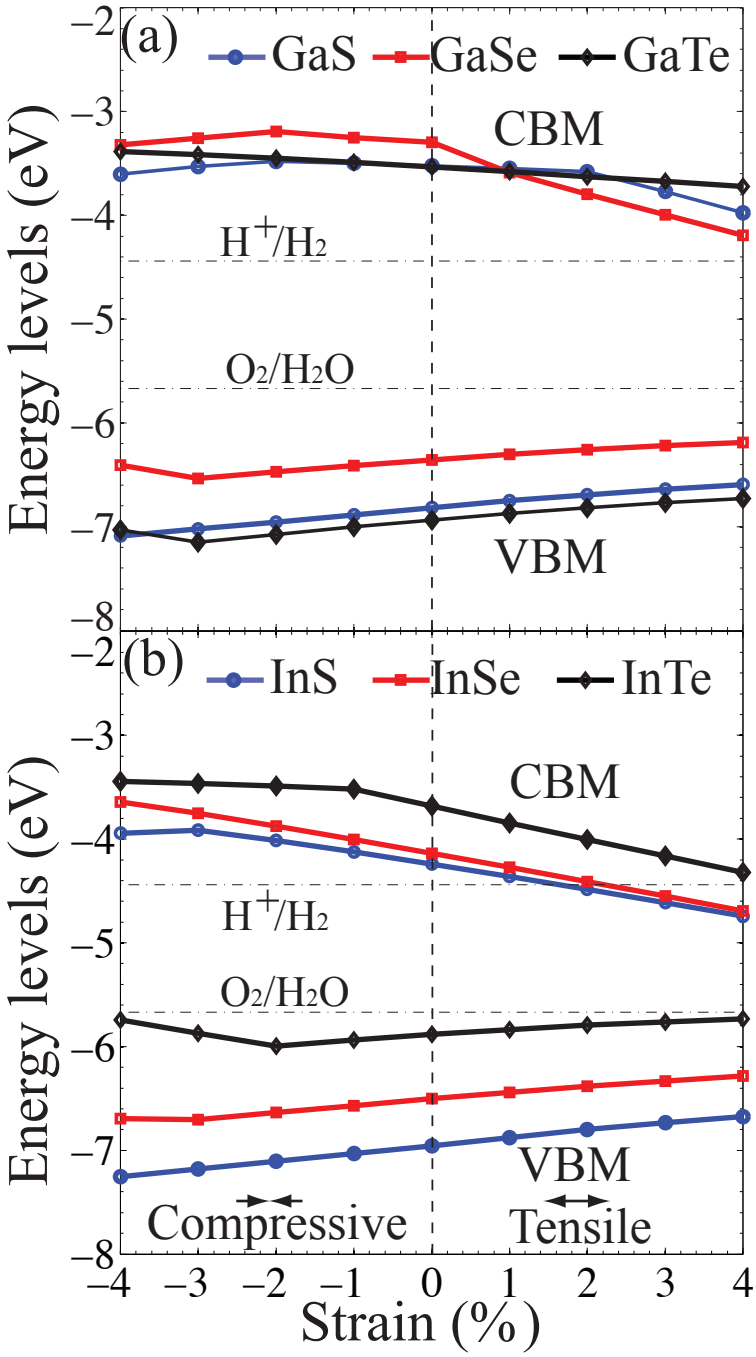

Figure 6.7: Strain effects on band edge positions of single-layer (a) GaX and (b) InX. Following the convention, positive strains indicate tension while negative strains denote compression. The discontinuity in slope of the band edges with strain for some MX arises from changes of the band edge positions to different k points.

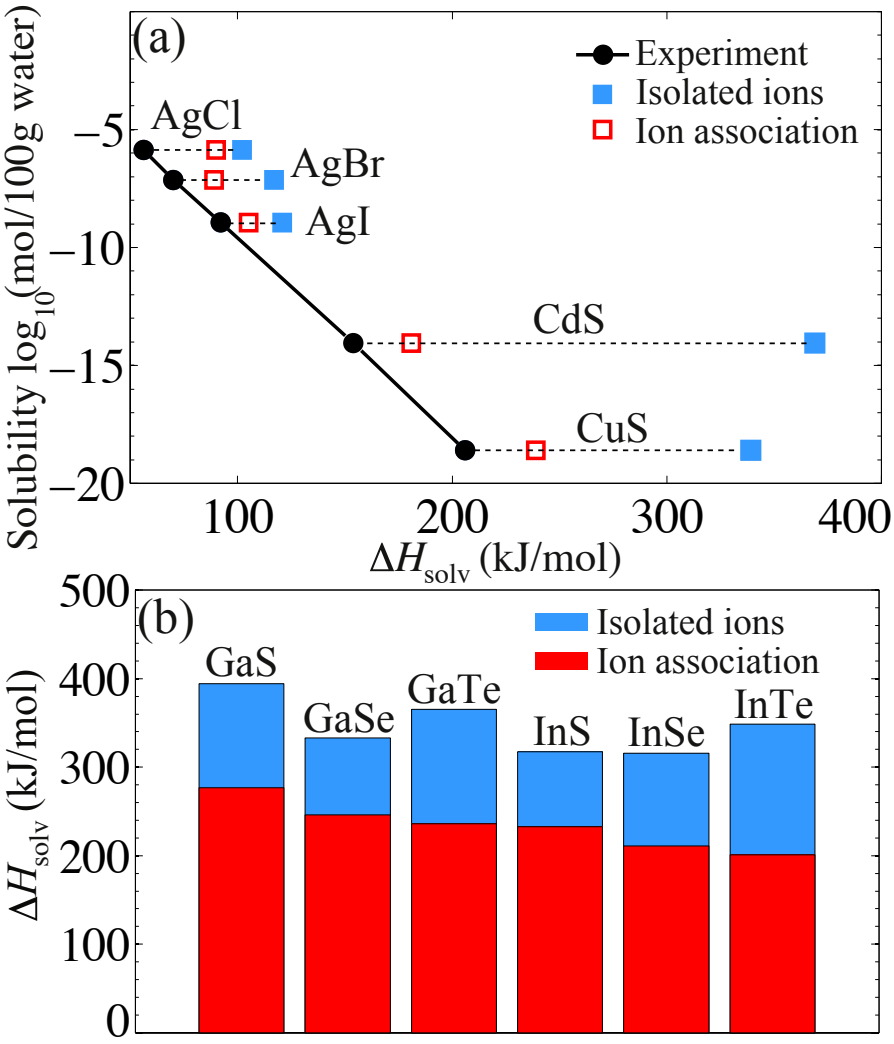

Figure 6.8: Stability of single-layer GaX and InX in water. (a) Experimental solubility of three silver halides and two sulfides as a function of calculated and experimental enthalpy of solvation ΔH. (b) Predicted enthalpy of solvation ΔH of the single-layer monochalcogenides. The high solvation enthalpies indicate that the single-layer monochalcogenides are insoluble in water.

CHAPTER 7

COMPUTATIONAL SEARCH FOR SINGLE-LAYER TRANSITION-METAL DICHALCOGENIDE PHOTOCATALYSTS

7.1 Abstract[1]

Some of the members of the family of single-layer transition-metal dichalcogenides have recently received a lot of attention for their promising electronic properties with potential applications in electronic devices. In this work we focus on the stability of the dichalcogenides and determine their potential for photocatalytic water splitting. Using a first-principles design approach, we perform a systematic theoretical study of the dichalcogenides MX_2 (M = Nb, Mo, Ta, W, Ti, V, Zr, Hf, and Pt; X = S, Se, and Te). First, we use a van der Waals functional to accurately calculate their formation energies. The results reveal that most MX_2 have similar formation energies to those of single-layer MoS_2 and WS_2, implying the ease of mechanically exfoliating a single-layer MX_2 from their layered bulk counterparts. Next, we use the many-body G_0W_0 approximation to obtain the band structures, finding that about half of the MX_2 are semiconductors. We then calculate conduction and valence band edge positions by combining the band gap center energies from the density-functional calculations and the G_0W_0 quasiparticle band gaps. Comparing these band edge positions with the redox potentials of water, we identify that single-layer MoS_2, WS_2, PtS_2 and $PtSe_2$ are potential photocatalysts for water splitting. Furthermore, we find that $PtSe_2$ undergoes a semimetal-to-semiconductor transition when the dimension is re-

[1]Reprinted with permission from: H. L. Zhuang, and R. G. Hennig, *J. Phys. Chem. C,* **117** (40), 20440-20445 (2013).

duced from 3D to 2D. Finally, large solvation enthalpies of these four candidate photocatalysts suggest their stability in aqueous solution.

7.2 Introduction

The family of single-layer transition-metal dichalcogenides MX_2 has recently received extensive attention because several of its members such as MoS_2 and WS_2 have successfully been synthesized and shown to exhibit attractive electronic properties such as direct band gaps [32]. In addition to the wide investigation of electronic properties [153, 3]. the study of photochemical properties of single-layer MX_2 appears to be another fast emerging research field [143]. For example, theoretical studies have shown that single-layer MoS_2 exhibits the potential of being used as photocatalysts for solar water splitting to generate hydrogen [154, 143].

To become a promising candidate semiconductor for water splitting, three criteria need to be satisfied simultaneously [155]. First, the band gap of the semiconductor must be at least 1.6-1.7 eV to drive the kinetics of the hydrogen and oxygen evolution reactions. Second, the band edges must straddle the redox potentials of water. Finally, the semiconductor should be insoluble in an aqueous solution.

On the basis of these criteria, we have suggested a general procedure of screening potential 2D photocatalysts.This procedure consists of the successive evaluations of the stability of the 2D materials, their bandgaps, band edge positions, and solubility. We have successfully applied this procedure in a previous study to single-layer Ga and In-based monochalcogenides which are all semi-

conductors [2]. In the current work, we extend the applications of the screening procedure to the family of transition-metal dichalcogenides, differing from the monochalcogenides not only in their chemistry and structure but also in their electronic structures ranging from metals to semiconductors. To obtain accurate bandgaps and band edge positions, we perform many-body G_0W_0 calculations. To examine the solubility of the single-layer MX_2 compounds in water, we compute their solvation enthalpies.

7.3 Simulation Methods

All calculations are based on DFT and the many-body G_0W_0 approach using the projector augmented wave (PAW) method as implemented in the plane wave code VASP [59, 77, 78]. For the structural relaxations we employ the generalized gradient approximation with the PBE parametrization [61]. A cutoff energy of 400 eV for the plane wave basis set is used throughout all calculations and ensures an accuracy of the energy of 1 meV/atom. The k-point sampling uses the Monkhorst-Pack scheme [81] and employs for the single-layer materials a $48 \times 48 \times 1$ grid for the PBE functional and a $18 \times 18 \times 1$ for the more expensive G_0W_0 calculations. We use 64 bands and 96 frequency points for all G_0W_0 calculations, ensuring E_g^{QP} is converged to 1 meV. For the single-layer materials a vacuum spacing of 18 Å ensures that the interactions between the layers are negligible.

The formation energy E_f of single-layer MX_2 is defined relative to the 3D bulk ground state structure as

$$E_f = E_{2D}/N_{2D} - E_{3D}/N_{3D}, \tag{7.1}$$

where E_{2D} and E_{3D} are the total energies of single-layer and bulk MX_2, respectively [55, 19]. N_{2D} and N_{3D} are the numbers of atoms in the 2D and the 3D unit cell, respectively. The 3D bulk structures of the MX_2 are either $P\bar{3}m1$ or $P6_3/mmc$ [100]. To account for the van der Waals interactions, the vdw-optB88 functional is used for the calculations of the formation energies [120].

We employ the method proposed by Toroker *et al.* to determine the band edge positions [136]. The conduction band minimum (CBM) and valence band maximum (VBM) energies, E_{CBM} and E_{VBM}, are given by

$$E_{CBM/VBM} = E_{BGC} \pm \frac{1}{2} E_g^{QP}, \tag{7.2}$$

where E_{BGC} is the bandgap center energy calculated with the PBE functional. E_{BGC} has been shown insensitive to various exchange-correlation functionals [2], E_g^{QP} in eq 7.2 denotes the quasiparticle bandgap from the G_0W_0 calculation.

The single-layer MX_2 compounds exhibit a structure consisting of three atomic sublayers with the metal atom M in the center sublayer bonded to six nearest-neighbor X atoms located in the top and bottom sublayers. Figure 7.1 depicts the two structure types that correspond to different stacking of the top and bottom X sublayers. In the $2H$ structure the top and bottom X sublayers are in an eclipsing configuration, while in the $1T$ structure the top X sublayer is displaced with reference to the bottom one by a vector of $1/3$ ($\vec{a}_1$+$\vec{a}_2$), where $\vec{a}_1$ and $\vec{a}_2$ are the in-plane lattice vectors. The occurrence of these two distinctive stacking structures is due to the ionicity of MX_2 [139]. MX_2 compounds with higher ionicity favor the $1T$ structure in which the X anions of the top and bottom sublayers are further apart from each other, minimizing their electrostatic repulsion.

To assess the stability of single-layer MX_2 in water, we calculate the solva-

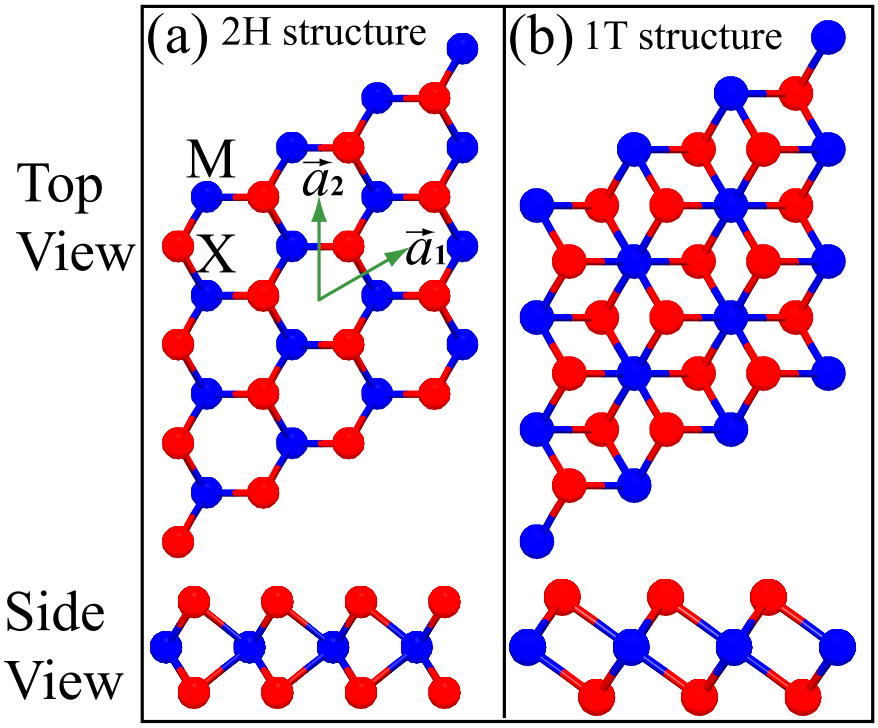

Figure 7.1: Two crystal structures of single-layer MX_2. (a) 2*H* structure and (b) 1*T* structure.

tion enthalpy, ΔH_{solv}, defined as the enthalpy change of the following solvation reaction

$$MX_2(s) \rightleftharpoons M^{2n+}(aq) + 2X^{n-}(aq). \tag{7.3}$$

where $M^{2n+}(aq)$ and $X^{n-}(aq)$ represent the M and X ions in aqueous solution, respectively. To calculate ΔH_{solv}, we decompose the reaction 7.3 into two steps. In the first reaction, the solid compound is separated into isolated gas atoms, i.e.

$$MX_2(s) \rightleftharpoons M(g) + 2X(g). \tag{7.4}$$

The enthalpy change of reaction 7.4, i.e. the cohesive energy of the MX_2 compound, ΔE_{coh}, is calculated using the VASP code and the PBE functional. In the second reaction, the gas atoms are ionized and subsequently solvated in water,

i.e.

$$M(g) + 2X(g) \rightleftharpoons M^{2n+}(aq) + 2X^{n-}(aq). \tag{7.5}$$

To calculate the enthalpy change, ΔH_{hyd}, of this reaction, we calculate the energy of the isolated atoms and of the hydrated ions using Gaussian09 [60]. The aug-cc-pVQZ basis sets are used for all calculations and for the heavy atoms Mo, W, Pt, and Te, we use effective core potentials [156, 157]. The energy of the solvated ions is calculated using several explicit water molecules and the SMD solvation model for the solute-solvent interactions [158]. Our convergence tests show that three water molecules are required to converge the hydration energy ΔH_{hyd} to 25 kJ/mol. We also consider the effect of ion association by calculating the energy of M^{2n+}-X^{n-} pairs in aqueous solution using the SMD model. The enthalpy of solvation ΔH_{solv} is given by the sum of the cohesive energy ΔE_{coh} and the enthalpy of hydration ΔH_{hyd}. The value of n for the charge state of the $M^{2n+}(aq)$ and $X^{n-}(aq)$ ions in aqueous solution is determined by the lowest enthalpy of hydration.

7.4 Results and Discussion

7.4.1 Structure and Stability of Single-Layer MX_2 Compounds

Table 7.1 and Table 7.2 list the formation energies as well as the structural parameters of single-layer MX_2 and Fig. 7.2 compares their formation energies. We observe that the formation energies increase for each cation group. Furthermore, most single-layer MX_2 have comparable formation energies to that of single-layer MoS_2. A common method to fabricate single-layer MX_2 such as

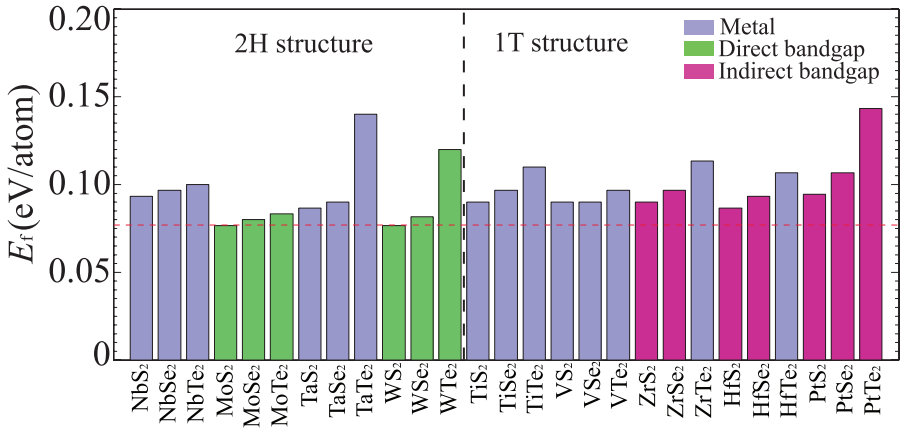

Figure 7.2: Formation energies of single-layer transition-metal dichalcogenides. The similarity of the formation energies for the MX_2 to the value for MoS_2, indicated by the red dashed line, suggests the ease of mechanical exfoliation of the single-layer materials from bulk crystals.

MoS_2 and $NbSe_2$ is micro-mechanical exfoliation [38]. The formation energy is an important indicator of the strength of interlayer van der Waals interactions in bulk MX_2. Therefore, the small formation energies indicate the ease to cleave a sheet of single-layer MX_2 from bulk crystals.

Recent experiments show that both the 2*H* and the 1*T* phases can coexist in single-layer MoS_2 [159]. To test whether a similar phase coexistence can occur in other MX_2, we compare the energy difference ΔE between the 1*T* and 2*H* phases for each MX_2, i.e. $\Delta E = E_{1T} - E_{2H}$. The results of ΔE are given in Table 8.1. For the 2*H* phases, all ΔE are positive, indicating that 2*H* phases remain stable. Surprisingly, the ΔE of MoS_2 is the second largest among all 2*H* phases. Similarly, for the 1*T* phases, the negative ΔE indicates that the 1*T* phases are more stable. Notably for Nb and Ta-based dichalcogenides, their formation energies of the 2*H* and 1*T* structures are close, implying a possible coexistence of these two phases.

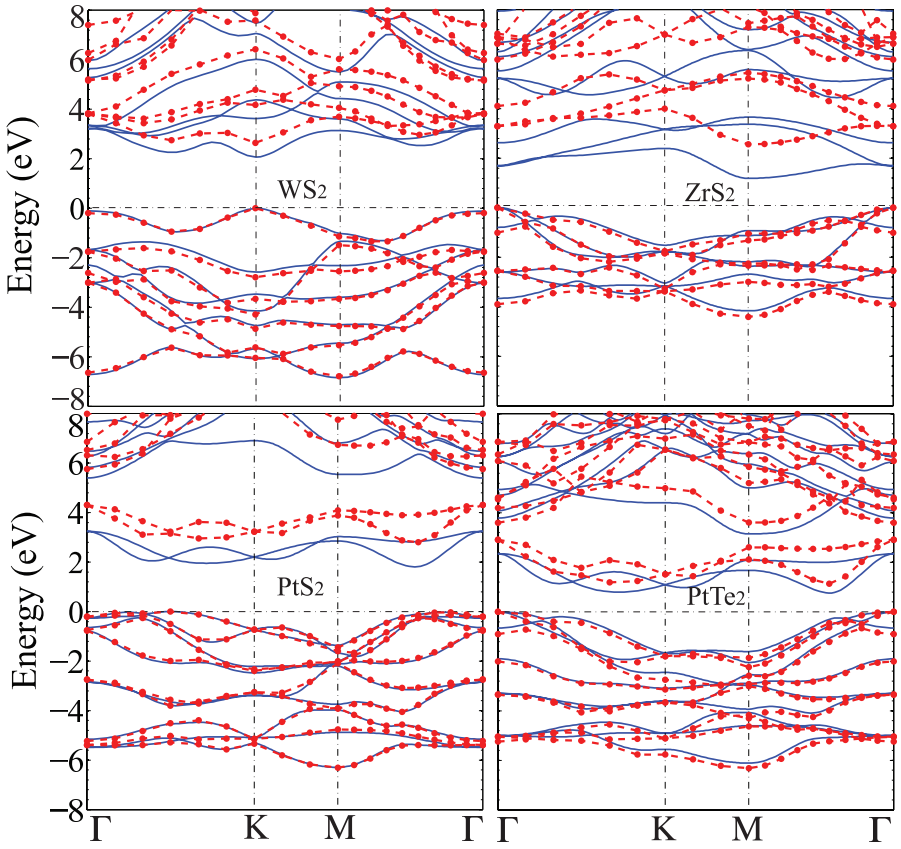

Figure 7.3: Band structures of single-layer WS_2, ZrS_2, PtS_2, and $PtTe_2$ calculated with the PBE functional (solid blue lines) and the G_0W_0 method (red circles). The valence band maximum is set to zero.

7.4.2 Band Alignment of Single-Layer MX_2 Compounds with Water Redox Potentials

We then determine the electronic structures of all 27 single-layer MX_2. Figure 7.2 reveals that 13 MX_2 are semiconductors, whose band edges can be classified into four categories based on the VBM and CBM positions in the reciprocal space. First, for all six molybdenum and tungsten dichalcogenides, both the VBM and the CBM are located at the K point, i.e. all of these compounds are direct-bandgap semiconductors, arising from the strong localization of *d*-electron or-

bitals at the transition metal atoms [132]. Second, for ZrS_2, $ZrSe_2$, HfS_2, and $HfSe_2$, the VBM appears at the Γ point while the CBM is at the M point. Third, for PtS_2, the VBM shows up between the Γ and K points, and the CBM is between the Γ and M points. In the last category comprised of $PtSe_2$ and $PtTe_2$, their VBM is at the Γ point, while the CBM is between the Γ and K points. Four representative band structures from all categories are shown in Fig. 7.3. The PBE functional and the G_0W_0 method are used to obtain these band structures. As can be seen, the G_0W_0 method only corrects the band gap sizes while keeping the positions of the band edges in reciprocal space unchanged.

Table 7.3 summarizes the bandgaps calculated with the PBE functional and the G_0W_0 method. As expected, the PBE bandgaps are smaller than the quasiparticle band gaps and underestimate the experimental ones [146]. The quasiparticle bandgaps correspond to the fundamental bandgaps measured in photoemission/inverse photoemission (PES/IPES) experiments, while the bandgaps measured by optical spectroscopy are reduced due to exciton binding [136]. Previous calculations for single-layer MoS_2 using the G_0W_0 method and the HSE06 hybrid density functional resulted in bandgaps of 2.50 eV and 2.34 eV [160, 133, 147], respectively, which are similar to our G_0W_0 value of 2.36 eV. Recent calculations for single-layer MoS_2 and WS_2 by Shi *et al.* [160] using the self-consistent GW_0 method for the quasiparticle gap and the Bethe-Salpeter equation to determine the exciton binding energy, resulted in quasiparticle bandgaps that are slightly larger by 0.3 eV than our values and predict an exciton binding energy in MoS_2 and WS_2 of 0.6 eV. We observe that most single-layer MX_2 possess quasiparticle bandgaps within the visible light energy range. Both the PBE functional and the G_0W_0 method show a decreases of the bandgap in each cation group because of the decrease in ionicity.

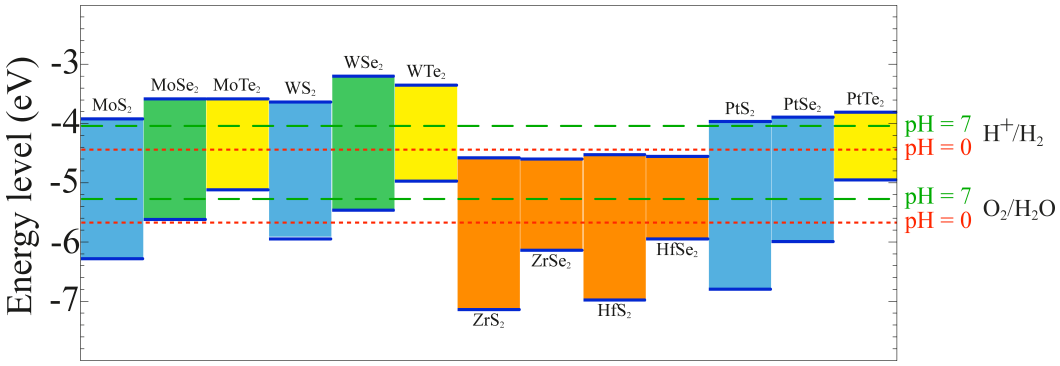

Figure 7.4: Band edge positions of single-layer transition-metal dichalcogenides relative to the vacuum level. The redox potentials of water splitting at pH = 0 (red dotted line) and pH = 7 (green dashed line) are shown for comparison.

Figure 7.4 compares the band edge positions of single-layer MX_2 with the redox potentials of hydrogen evolution (H^+/H_2) and oxygen evolution (O_2/H_2O) at pH = 0 and pH = 7. While the majority of single-layer MX_2 have band edge energies that are unfavorable for photocatalytic water splitting without application of an external bias potential, we find that MoS_2, WS_2, PtS_2, and $PtSe_2$ exhibit band edges that straddle the redox potentials of water at for the pH = 0 and make them promising candidates for photocatalytic water splitting. These four single-layer materials should be able to split water without imposing an external bias voltage. Our conclusion that single-layer MoS_2 is able to catalyze the water-splitting reaction is in agreement with previous theoretical predictions [154, 143].

In the above discussion, we consider a mechanism of water splitting where the *exciton splits* into an electron in the conduction band and a hole in valence band, which diffuse separately and react with water. In this case, the exciton binding energy needs to be overcome and the CBM and VBM must be aligned energetically favorable with the water redox potentials. Indeed, there exists a

second mechanism where the exciton binding plays an important role. In this scenario, the *exciton directly reacts* with water, the exciton binding energy must not reduce the CBM and VBM levels too much as to make the redox reaction unfavorable. Assuming a similar exciton binding energy for all the MX_2 as calculated for MoS_2 and WS_2 of 0.6 eV [160], we observe that the redox reaction is still energetically favorable for MoS_2, WS_2, PtS_2, and $PtSe_2$.

To understand why these 2D materials become promising candidate photocatalysts, we perform similar calculations of bandgaps, bandgap center, and band edge positions of their 3D counterparts. The results are shown in Table 7.4 for all the MX_2 compounds except $PtSe_2$ which is a semimetal [161]. Consistent with the experimental reports, the band edge positions confirm that none of the three bulk materials are suitable for water splitting. Compared with the bandgaps listed in Table 7.3, the bandgaps of MoS_2, WS_2 and PtS_2 increase significantly due to the dimension reduction from 3D to 2D. The increase in bandgap shifts the CBM and VBM and makes these single-layer materials potential photocatalysts for water splitting.

The reason why single-layer $PtSe_2$ turns into a competitive photocatalyst is slightly different. Figure 7.5 shows the density of states (DOS) of bulk and single-layer $PtSe_2$ with the G_0W_0 method. For bulk $PtSe_2$, there exist a finite number of electronic states at the Fermi level. A similar DOS is obtained from the HSE06 functional [63, 162]. Therefore, bulk $PtSe_2$ is metallic, consistent with previous theoretical and experimental studies [161]. In contrast, single-layer $PtSe_2$ is semiconducting as can be seen by the DOS shown in Fig. 7.5(b). The opening of a wide bandgap makes the single-layer $PtSe_2$ a potential photocatalyst.

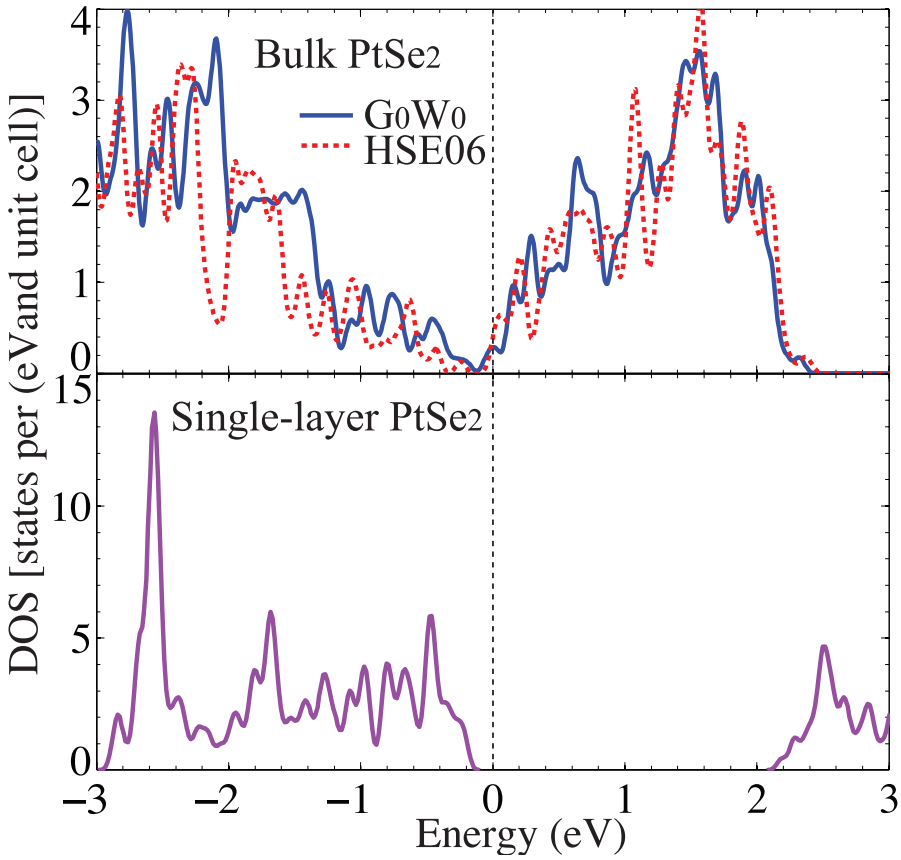

Figure 7.5: Density of states of (a) bulk PtS_2 calculated with the G_0W_0 method and the HSE06 functional and (b) single-layer PtS_2 obtained from the G_0W_0 method.

7.4.3 Tuning of Band Edge Positions

Figure 7.4 shows that some of the band edge positions of the single-layer materials such as $MoSe_2$ and WSe_2 are close to the oxygen redox potential of water. Several approaches can be adopted to shift these band edge positions and enable these materials to drive the oxygen evolution reaction, The first method is based on the dependence the redox potentials on the pH values [137]. Increasing the pH shifts both energy levels of H^+/H_2 and O_2/H_2O upwards as illustrated in Fig. 7.4, making $MoSe_2$ and WSe_2 possible photocatalysts. The second method is based on applying an external bias voltage. The larger the energy difference

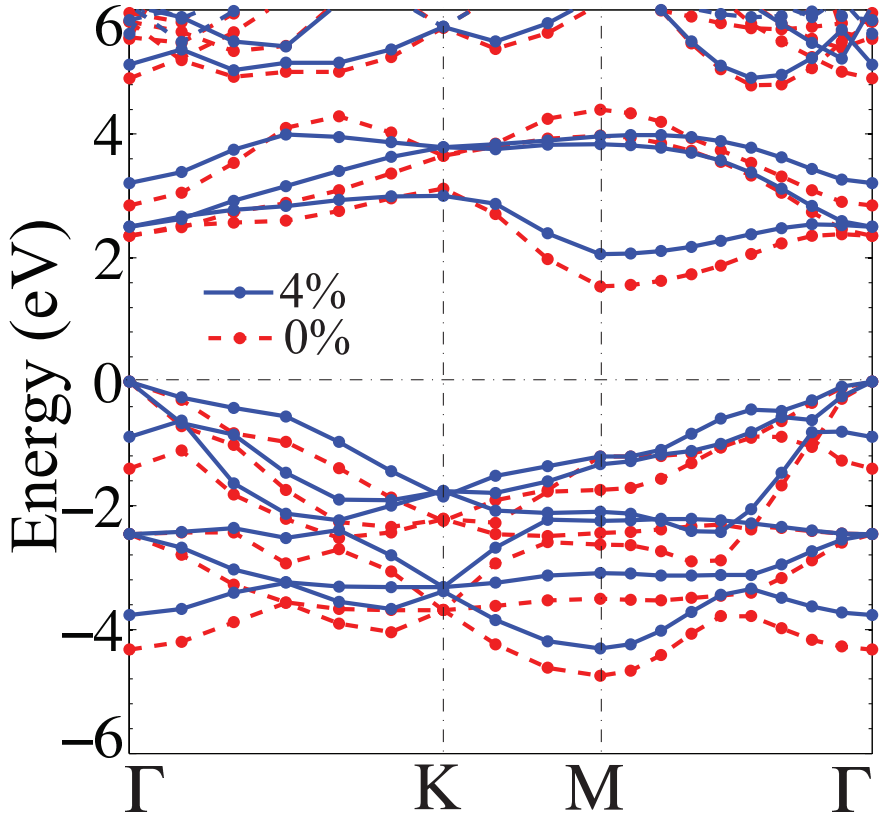

Figure 7.6: G_0W_0 band structures of single-layer $ZrSe_2$ at the strains of 0% (red) and 4% (blue). Valence band maximum is set to zero.

is between the CBM (VBM) and the energy levels of H^+/H_2 (O_2/H_2O) the larger the required bias voltage must be.

A third alternative method of adjusting the bandgaps and band edge positions of a semiconductor is the application of mechanical strains. For example, applying a 4% tensile strain to single-layer $ZrSe_2$ results in the G_0W_0 band structure shown in Fig. 7.6. Compared to the bandgap at zero strain, the bandgap is increased by the strain from 1.54 eV to 2.06 eV. The tensile strain additionally affects the bandgap center energy, decreasing it from −5.37 eV to −5.47 eV. As a result, the CBM is shifted to −4.44 eV. Although this energy remains still insufficient to drive the hydrogen evolution reaction spontaneously, the external bias

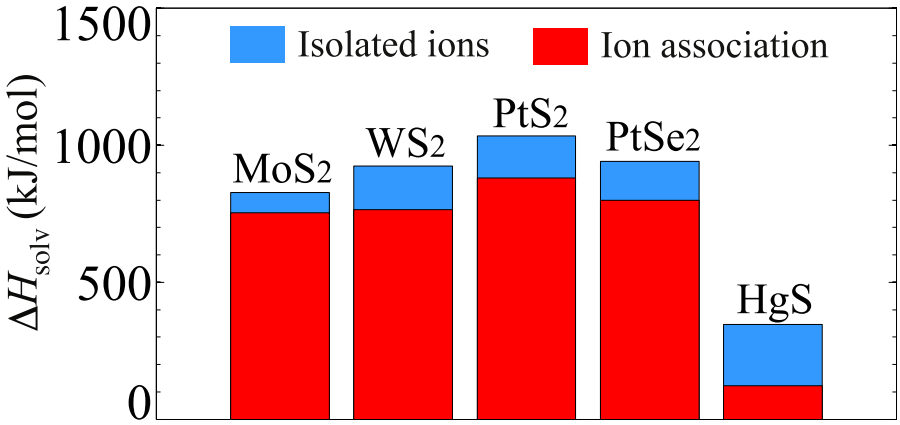

Figure 7.7: Solvation enthalpies of single-layer MoS_2, WS_2, PtS_2, and $PtSe_2$. The enthalpy of insoluble HgS is also shown for comparison.

voltage needed to split water would be drastically reduced.

7.4.4 Stability of MX_2 Compounds in Water

Comparing the solvation enthalpies, ΔH_{hyd}, for different values n for the charge state of the $M^{2n+}(aq)$ and $X^{n-}(aq)$ ions in aqueous solution, we find that the lowest energy charge states of the transition metal cations and chalcogen anions in aqueous solution are +2 and −1, respectively. In contrast, the energy of the solvated ions with charge states of +4 and −2 is more than 3 eV higher than the energy of the lower charge states. We furthermore also consider the effect of possible ion association consisting of M^{2+}-X^{-} pairs in aqueous solution [163].

Figure 7.7 compares the resulting solvation enthalpies, ΔH_{solv}, of single-layer MoS_2, WS_2, PtS_2, and $PtSe_2$ with the calculated ΔH_{solv} of HgS, which exhibits a negligible solubility of 1.27×10^{-27} mol per 100 g water [150]. For both cases of isolated and associated ions, the solvation enthalpies, ΔH_{solv}, of the four single-layer materials are significantly larger than that of HgS. Since the solubility of

a solid compound generally decreases exponentially with increasing solvation enthalpy [2], we expect that these single-layer materials are insoluble in water.

7.5 Summary

We have performed a systematic search for potential photocatalysts for solar water splitting in the family of transition-metal dichalcogenides. We found that the formation energies of single-layer transition-metal dichalcogenides are comparable to those of single-layer MoS_2 and WS_2, which have been successfully synthesized. In addition, the calculations of band structures reveal that 13 single-layer transition-metal dichalcogenides are semiconductors with four different types of band edge positions. Among the semiconducting transition-metal dichalcogenides, we have identified that single-layer MoS_2, WS_2, PtS_2 and $PtSe_2$ are potential photocatalysts for splitting water. In addition, we observed that $PtSe_2$ transforms into a semiconductor because of the dimension reduction. Finally, we predict high enthalpies of solvation for the four single-layer materials, indicating that they are insoluble in water.

Table 7.1: Structural parameters and formation energies E_f of $2H$ single-layer transition-metal dichalcogenides MX_2 calculated with the PBE functional. The structural parameters include lattice constant a_0 (Å), M-X bond length b_{M-X} (Å), X-X bond length b_{X-X} (Å), X-M-X bond angle θ_{X-M-X} (degrees). ΔE refers to the energy difference between the $1T$ and the $2H$ structures. All energies are in units of eV/atom.

	a_0	b_{M-X}	b_{X-X}	θ_{X-M-X}	E_f	ΔE
NbS_2	3.36	2.49	3.14	77.97	0.093	0.035
$NbSe_2$	3.48	2.62	3.37	79.90	0.097	0.032
$NbTe_2$	3.69	2.82	3.70	81.85	0.100	0.003
MoS_2	3.18	2.41	3.13	80.80	0.077	0.283
$MoSe_2$	3.32	2.54	3.34	82.18	0.080	0.237
$MoTe_2$	3.55	2.73	3.61	82.77	0.083	0.173
TaS_2	3.34	2.48	3.13	78.11	0.087	0.023
$TaSe_2$	3.47	2.61	3.35	79.87	0.090	0.023
$TaTe_2$	3.70	2.81	3.66	81.19	0.140	0.003
WS_2	3.18	2.42	3.14	81.05	0.077	0.297
WSe_2	3.32	2.55	3.36	82.46	0.080	0.257
WTe_2	3.55	2.74	3.63	83.02	0.120	0.183

Table 7.2: Structural parameters and formation energies E_f of $1T$ single-layer transition-metal dichalcogenides MX_2 calculated with the PBE functional. The structural parameters include lattice constant a_0 (Å), M-X bond length b_{M-X} (Å), X-X bond length b_{X-X} (Å), X-M-X bond angle θ_{X-M-X} (degrees). ΔE refers to the energy difference between the $1T$ and the $2H$ structures. All energies are in units of eV/atom.

	a_0	b_{M-X}	b_{X-X}	θ_{X-M-X}	E_f	ΔE
TiS_2	3.40	2.43	3.46	89.08	0.090	−0.137
$TiSe_2$	3.52	2.56	3.71	87.00	0.097	−0.113
$TiTe_2$	3.74	2.78	4.10	84.71	0.110	−0.100
VS_2	3.17	2.35	3.46	85.04	0.090	−0.003
VSe_2	3.32	2.48	3.70	83.81	0.090	−0.007
VTe_2	3.55	2.69	4.05	82.54	0.097	−0.002
ZrS_2	3.68	2.57	3.60	91.36	0.090	−0.187
$ZrSe_2$	3.80	2.71	3.85	89.16	0.097	−0.157
$ZrTe_2$	3.97	2.92	4.27	85.83	0.113	−0.097
HfS_2	3.64	2.55	3.57	91.02	0.087	−0.213
$HfSe_2$	3.76	2.68	3.82	89.05	0.093	−0.170
$HfTe_2$	3.96	2.89	4.21	86.54	0.107	−0.127
PtS_2	3.57	2.40	3.21	96.18	0.093	−0.598
$PtSe_2$	3.75	2.53	3.40	95.63	0.107	−0.452
$PtTe_2$	4.02	2.71	3.62	95.96	0.143	−0.056

Table 7.3: Bandgaps E_g, bandgap center energies E_{BGC}, and band edge positions E_{CBM} and E_{VBM} of single-layer semiconducting transition-metal dichalcogenides. The bandgaps are calculated with two approaches, with DFT using the PBE functional yielding E_g^{PBE} and the many-body G_0W_0 approximation yielding the quasiparticle bandgaps E_g^{QP}. All energies are in units of eV.

	E_g^{PBE}	E_g^{QP}	E_{BGC}	E_{CBM}	E_{VBM}
MoS_2	1.68	2.36	−5.10	−3.92	−6.28
$MoSe_2$	1.45	2.04	−4.60	−3.58	−5.62
$MoTe_2$	1.08	1.54	−4.35	−3.58	−5.12
WS_2	1.82	2.64	−4.79	−3.47	−6.11
WSe_2	1.55	2.26	−4.33	−3.20	−5.46
WTe_2	1.07	1.62	−4.16	−3.35	−4.97
ZrS_2	1.19	2.56	−5.86	−4.58	−7.14
$ZrSe_2$	0.50	1.54	−5.37	−4.60	−6.14
HfS_2	1.27	2.45	−5.75	−4.53	−6.98
$HfSe_2$	0.61	1.39	−5.25	−4.56	−5.95
PtS_2	1.81	2.83	−5.45	−3.97	−6.80
$PtSe_2$	1.41	2.10	−5.03	−3.98	−6.08
$PtTe_2$	0.79	1.14	−4.38	−3.81	−4.95

Table 7.4: Bandgaps E_g, bandgap center E_{BGC}, and band edge positions E_{CBM} and E_{VBM} of the 3D bulk structures of semiconducting MoS_2, WS_2 and PtS_2. The bandgaps are calculated with two approaches, with DFT using the PBE functional yielding E_g^{PBE} and the many-body G_0W_0 approximation yielding the quasiparticle bandgaps E_g^{QP}. All energies are in units of eV.

	E_g^{PBE}	E_g^{QP}	E_{BGC}	E_{CBM}	E_{VBM}
MoS_2	0.94	1.30	−4.82	−4.17	−5.47
WS_2	1.05	1.48	−4.56	−3.82	−5.30
PtS_2	0.73	1.13	−5.18	−4.62	−5.75

CHAPTER 8

THEORETICAL PERSPECTIVE OF PHOTOCATALYTIC PROPERTIES OF SINGLE-LAYER SnS_2

8.1 Abstract[1]

We present a first-principles study of the photocatalytic properties of single-layer SnS_2. First, we calculate the formation energy and the phonon spectrum, verifying static and dynamical stability, respectively. In addition, our calculated energy of solvation suggests that single-layer SnS_2 is stable in aqueous solution. Next, by solving the Bethe-Salpeter equation, we obtain an optical band gap of 2.75 eV, consistent with the measured optical band gap. The resulting exciton binding energy of 0.41 eV is consistent with the Mott-Wannier model. Finally, by aligning the band edges with the redox potentials of water, we find that a bias potential of at least 0.9 V is required to drive the hydrogen evolution and that compressive strains can reduce this bias potential.

8.2 Introduction

Hydrogen is regarded as the fuel of the future [164]. Generating hydrogen from solar water splitting via a semiconducting photocatalyst is a promising clean solution to overcome the existing energy shortage problems [155]. In addition to their attractive electronic properties [86, 3, 32], single-layer materials have recently been shown by both theoretical calculations and experiments to

[1]Reprinted with permission from: H. L. Zhuang and R. G. Hennig, *Phys. Rev. B,* **88** (11), 115314 (2013). Copyright 2013 by American Physics Society.

function as potential photocatalysts for water splitting. For example, theoretical studies have predicted that single-layer transition metal dichalcogenides and group-III monochalcogenides are potential photocatalysts for water splitting [154, 143, 2, 56].

Experiments show evidence that several single-layer materials are advantageous over their three-dimensional (3D) counterparts for use as photocatalysts. One representative example is the study by Sun *et al.* for single-layer SnS_2 as a photocatalyst for solar water splitting [45]. The work shows that the incident photon-to-current conversion efficiency of single-layer SnS_2 can approach 38.7%, in striking contrast to the low efficiency of 2.33% of 3D bulk SnS_2. Single-layer SnS_2 exhibits a hexagonal structure with space group $P3m1$. Figure 8.1 shows that the single-layer structure consists of three atomic sublayers with Sn atoms forming the center sublayer bonded to six nearest-neighbor S atoms located in the top and bottom sublayers.

In this work we determine the stability, band gap, and band edge positions of single-layer SnS_2, which are of importance for the material being a potential photocatalyst. We show that single-layer SnS_2 exhibits a low formation energy, dynamically stable phonon modes, and a high energy of solvation. Furthermore, we determine the optical band gap of single-layer SnS_2 as 2.75 eV, right within the range of visible light. Moreover, we show that the lowest-energy exciton in single-layer SnS_2 is accurately described by the Mott-Wannier model [165]. Finally, we show that an external bias potential of at least 0.9 V is required to drive the hydrogen evolution and that compressive strains can reduce this bias potential.

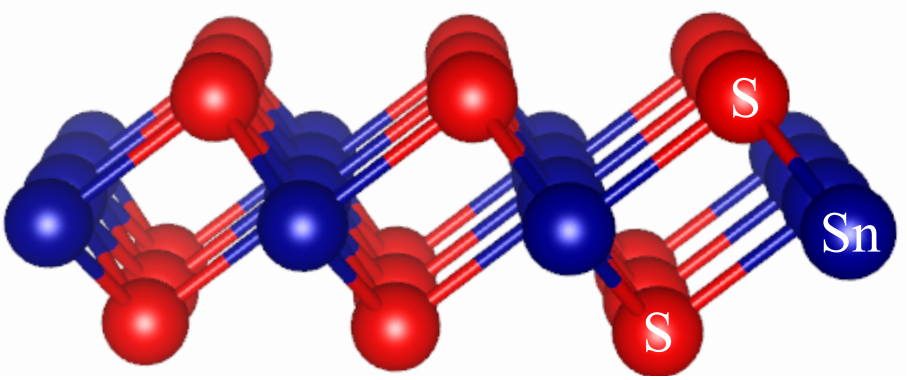

Figure 8.1: Crystal structure of single-layer SnS_2. Each sulfur atoms (red ball) has three nearest neighboring tin atoms, while each tin atom (blue ball) has six nearest neighboring sulfur atoms.

8.3 Methods

We perform density-functional theory (DFT) calculations using the projector augmented wave method as implemented in the plane-wave code VASP [59, 77, 78]. For the structural relaxations we employ both the Perdew-Burke-Ernzerhof (PBE) generalized gradient approximation and the Heyd-Scuseria-Ernzerhof (HSE06) hybrid functional [61, 63]. For the phonon calculations, we use a cut-off energy of 600 eV to ensure the convergence, particularly of the low-energy phonon modes. For all other calculations, a cutoff energy of 400 eV for the plane wave basis set ensures an energy accuracy of 1 meV/atom. The k-point sampling uses the Monkhorst-Pack scheme [81] and employs for the single-layer materials a $48 \times 48 \times 1$ mesh for the PBE functional and an $18 \times 18 \times 1$ mesh for the more expensive HSE06, G_0W_0, and Bathe-Salpeter calculations. For the single-layer SnS_2 calculations, a periodic repeat length of 18 Å in the direction perpendicular to the SnS_2 sheet ensures that the interactions between the layers are negligible.

Table 8.1: Structural parameters and elastic modulus of single-layer and bulk SnS_2. The parameters include the lattice parameter a_0, the Sn-S bond length b_{Sn-S}, S-S bond length b_{S-S} in units of Å, and the Sn-S-Sn bond angle $\theta_{Sn-S-Sn}$ in units of degrees. The elastic modulus C is in units of N/m.

System	Functional	a_0	b_{Sn-S}	b_{S-S}	$\theta_{Sn-S-Sn}$	C
Single layer	PBE	3.70	2.60	3.65	90.75	87
	vdw-optB88	3.69	2.60	3.66	90.58	90
	HSE06	3.64	2.56	3.59	90.80	102
Bulk	vdw-optB88	3.71	2.60	3.66	90.82	89

The electron-hole interaction plays an important role in the optical response of a material [64]. We calculate the optical spectra of single-layer SnS_2 including the excitonic interaction by solving the Bethe-Salpeter equation (BSE) implemented in the VASP code [65, 66]. The BSE spectrum calculations are carried out starting from the G_0W_0 quasiparticle energies and the PBE wavefunctions. For the G_0W_0 calculations, we use 192 bands and 128 frequency points. The 12 highest valence bands and 16 lowest conduction bands are included in the calculation of the excitonic states.

To determine the stability of single-layer SnS_2 in aqueous solution we use Gaussian09 [60, 158] to calculate the hydration energy using the PBE functional. We employ the aug-cc-pVQZ basis sets, and for the heavy atom Sn we use effective core potentials [157, 156]. The energy of the solvated ions is calculated using several explicit water molecules and the density-based solvation model (SMD) for the solute-solvent interactions [158]. We find that three water molecules are required to converge the hydration energy to 4 kJ/mol.

8.4 Results

8.4.1 Stability

To be a useful material, single-layer SnS_2 needs to be stable, particularly in an aqueous environment. We determine the stability of single-layer SnS_2 by calculating its formation energy relative to the 3D bulk phase, its dynamic stability, and its solvation energy in water.

We first determine the structural parameters of single-layer SnS_2. Table 8.1 shows that bulk- and single-layer SnS_2 exhibit similar structural parameters and elastic moduli. The generalized gradient approximation slightly overestimates the in-plane lattice parameter of bulk SnS_2 compared to the experimental value of 3.65 Å [166]. The HSE06 lattice parameters of single-layer SnS_2 is smaller than the PBE counterpart, since the HSE06 functional includes 25% of exact exchange, reducing the self-interaction error in the PBE functional and improving the agreement with experimental lattice parameters [142]. The elastic modulus of single-layer SnS_2 is significantly smaller than that of MoS_2, which exhibits an experimental mean value of 180 N/m [47].

To test the stability of single-layer SnS_2 relative to the energy of bulk SnS_2, we calculate its formation energy E_f as $E_f = E_{2D} - E_{3D}$. To accurately account for dispersion interactions, we use the vdw-optB88 van der Waals functional for the calculation of the formation energy. This functional has been found to accurately describe lattice constants and cohesive energies [59]. Without the van der Waals functional the single-layer SnS_2 incorrectly becomes the ground state. The resulting formation energy of single-layer SnS_2 is only 80 meV/atom higher

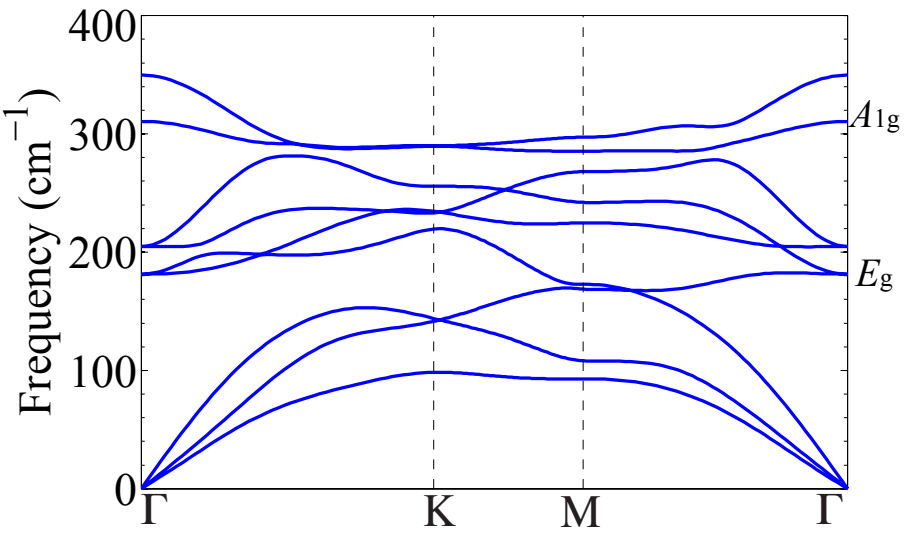

Figure 8.2: Phonon spectrum of single-layer SnS_2. The Raman-active modes at Γ are denoted as A_{1g} and the E_g, respectively.

than that of the bulk phase. This low formation energy is comparable to that of single-layer transition metal dichalcogenides such as MoS_2 and other group-III monochalcogenides such as GaS and GaSe, all of which have been successfully synthesized by micro-mechanical exfoliation [56, 2, 38].

To determine the dynamical stability of single-layer SnS_2, we obtain its phonon spectrum from the force constants calculated with density functional perturbation theory [57, 101] and the PBE functional. Figure 8.2 shows the phonon spectrum of single-layer SnS_2. No imaginary frequencies are observed, confirming the dynamical stability of single-layer SnS_2. The irreducible representation of the phonon modes at the center of the Brillouin zone is given by $\Gamma = A_{1g} + 2A_{2u} + E_g + 2E_u$ [167]. Two of these six modes, the A_{1g} and E_g modes denoted in Fig. 8.2, are Raman active [101]. Our calculated phonon frequencies for the A_{1g} and E_g modes are 311 and 181 cm^{-1}, respectively. This is in excellent agreement with the experimental values of 310 and 200 cm^{-1}, respectively [45], indicating the accuracy of DFT for single-layer SnS_2.

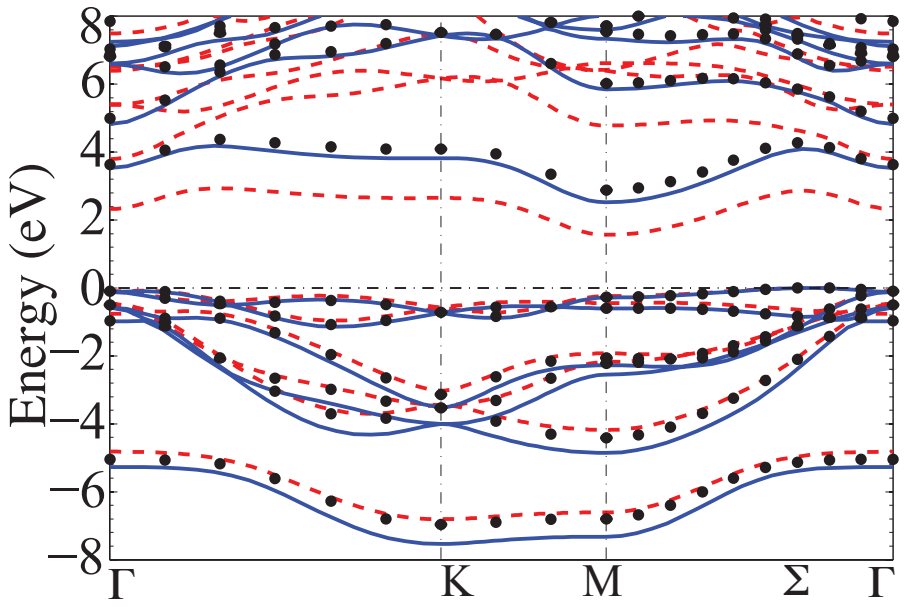

Figure 8.3: Band structure of single-layer SnS_2 calculated with the PBE (red dashed line) and HSE06 (blue solid line) functionals and the G_0W_0 method (black dots).

We then assess the stability of single-layer SnS_2 in water by calculating the solvation energy when crystalline SnS_2 is decomposed into Sn and S ions in aqueous solution. We first obtain the cohesive energy from the PBE functional as implemented in VASP and then calculate the hydration energy using the Gaussian09 package [60]. The solvation energy is given by the sum of these two energies [56, 2]. This method has been successfully applied to determine the stability of other single-layer materials such as MoS_2 and group-III monochalcogenides [56, 2]. The resulting solvation energy of single-layer SnS_2 is 620 kJ/mol, significantly larger than that of other poorly soluble compounds such as CuS exhibiting solvation energies ranging from 300 to 400 kJ/mol [150]. Taking into account ion association where a solvated cation-anion pair is formed, we obtain an almost identical solvation energy of 619 kJ/mol. The high solvation energy implies the stability of single-layer SnS_2 in aqueous solution.

Table 8.2: Fundamental indirect and direct band gaps (in eV) of single-layer SnS_2 obtained from three different approaches. Experimental optical band gaps from Ref. [1] are shown for comparison.

Gap	E_g^{PBE}	E_g^{HSE06}	$E_g^{G_0W_0}$	Experiment
Indirect (Σ-M)	1.57	2.52	2.88	2.23
Direct (M-M)	1.81	2.81	3.16	2.55

8.4.2 Electronic Structures

Figure 8.3 shows the band structures of single-layer SnS_2 obtained from the PBE and HSE06 functionals and the G_0W_0 method. SnS_2 displays an indirect band gap with the VBM located between the Γ and M points, while the CBM occurs at the M point. Table 8.2 compares the direct and indirect fundamental band gaps of single-layer SnS_2 from these three different approaches with the experimental optical band gaps [1]. The PBE functional as usual underestimates the band gaps [146] and predicts gaps 1 eV smaller than the HSE06 functional and the G_0W_0 approximation. The HSE06 and G_0W_0 methods predict similar band gaps with the G_0W_0 band gaps being about 0.35 eV larger. However, all three methods show that the difference between the indirect and direct band gaps is small, with a value of 0.3 eV, consistent with the difference of the experimental optical band gaps [1]. Furthermore, the band gaps of single-layer SnS_2 are well positioned within the range of 1.7 - 3.0 eV that is required for efficient photocatalytic water splitting [168, 134].

To understand the bonding characteristics of single-layer SnS_2, we analyze the total and projected density of states (TDOS and PDOS) within the energy

window of −4 to 4 eV with reference to the VBM. Figure 8.4 shows that the TDOS at the valence band edge is as large as 2.8 states/(eV unit cell). Such a large DOS is suggested as a main contributing factor to the prominent visible-light conversion efficiency of single-layer SnS_2 [45]. The corresponding PDOS of SnS_2 in Fig. 8.4 illustrates that the valence band of SnS_2 from −2 to 0 eV is dominated by the S $3p$ states, whereas in the lower energy window between −4 and −2 eV, it mainly consists of hybridized states of S $3p$ and Sn $5p$ orbitals.

8.4.3 Optical Properties

Figure 8.5 shows the imaginary part of the permittivity ϵ_2 calculated from the Bethe-Salpeter equation and random-phase approximation (RPA), respectively. Similar to single-layer MoS_2, the entire BSE optical absorption spectrum is dominated by resonant excitonic states [133, 160]. Three absorption peaks are observed in the low-energy region below 3.2 eV of the BSE spectrum. In contrast, no peaks are observed in the RPA spectrum of the same energy window, indicating the importance of considering excitonic effects. The first peak, located at an energy of 2.75 eV, corresponds to the direct optical band gap at the M point. This energy agrees well with the experimental direct optical band gap of 2.55 eV measured by UV-vis transmission spectroscopy [1]. The second peak appears at 2.92 eV due to another exciton, and the third peak corresponds to the direct quasiparticle band gap of 3.16 eV obtained with the G_0W_0 method. The energy difference between the first and third peak positions gives an exciton binding energy of 0.41 eV, close to the binding energy of 0.4 eV in bulk SnS_2 [169] ,and also comparable to the exciton binding energy of single-layer MoS_2 and WS_2 of 0.6 eV [160].

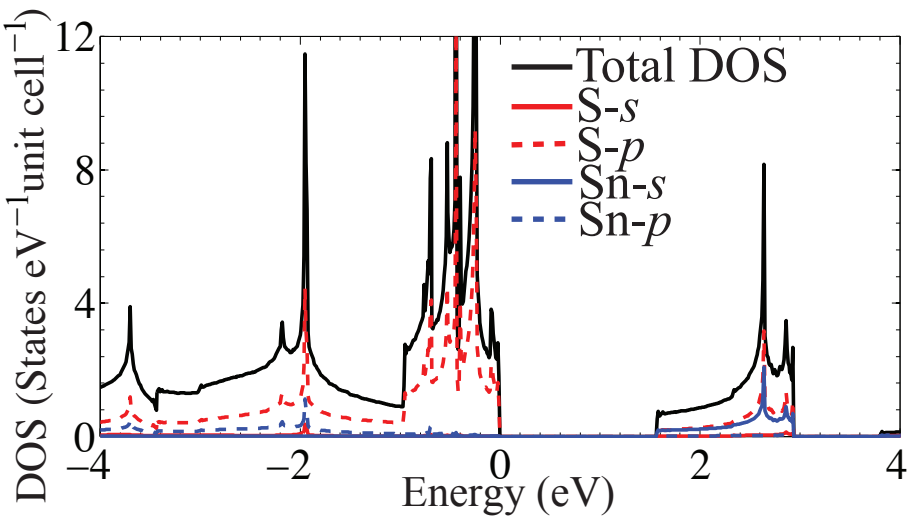

Figure 8.4: Total and projected density of states of single-layer SnS_2.

The Mott-Wannier model has recently been applied to estimate the exciton binding energy of single-layer MoS_2 [170, 165]. It is worthwhile testing whether this model is applicable to the excitons in single-layer SnS_2 as well. In this model excitons forms hydrogen-like states. In two dimensions, the first excitonic binding energy is

$$E_0 = 4\frac{m_r}{m_0}\frac{R_\infty}{\epsilon_{2D}^2}, \tag{8.1}$$

where m_r is the reduced effective electron mass, m_0, the rest mass of the electron, ϵ_{2D} the effective permittivity, and R_∞ the Rydberg constant [170].

For 2D systems, subtleties arise since the calculated permittivity tensor depends on the size of the simulation cell, i.e. the thickness of the vacuum layer. To determine the permittivity of single-layer SnS_2, ϵ_{SnS_2}, we treat each cell as a composite of one layer of SnS_2 and one layer of vacuum with $\epsilon_{vac} = 1$. We approximate the thickness of single-layer SnS_2 as 5.89 Å, which is the interlayer distance in bulk SnS_2 calculated with the vdw-optB88 van der Waals functional. Using the linear law [171], $\epsilon_{calc} = f \cdot \epsilon_{SnS_2} + (1-f) \cdot \epsilon_{vac}$, where f is the volume frac-

tion of the SnS_2 layer in a simulation cell, we fit the permittivity of single-layer SnS_2 from the calculated permittivity, ϵ_{calc}, for cells of dimension 10, 18, and 25 Å. This results in the relative permittivity parallel to the sheet of $\epsilon_{\parallel} = 8.17$, perpendicular to it of $\epsilon_{\perp} = 2.41$, and the effective permittivity of $\epsilon_{\text{2D}} = \sqrt{\epsilon_{\parallel} \cdot \epsilon_{\perp}}$. We obtain the reduced effective electron mass from $1/m_{\text{r}} = 1/m_{\text{e}} + 1/m_{\text{h}}$, where $m_{\text{e}} = 0.25\, m_0$ and $m_{\text{h}} = 0.37\, m_0$ are the electron and hole effective masses, respectively, at the *M* point obtained from the HSE06 band structure. The exciton binding energy predicted from the Mott-Wannier model is 0.41 eV, identical to the binding energy calculated by solving the Bethe-Salpeter equation. While such perfect agreement is probably somewhat fortuitous, it nevertheless indicates that the exciton in single-layer SnS_2 is a Mott-Wannier-type exciton.

8.4.4 Band Alignments

To determine under what conditions single-layer SnS_2 is able to photocatalytically split water, we calculate the band edge positions E_{CBM} and E_{VBM} relative to the vacuum level and compare them with the reduction and oxidation potentials of water. We follow the method by Toroker *et al.*[136] and determine the CBM and VBM levels from the band gap center energy, E_{BGC}, relative to the vacuum level and the value of the band gap E_{g}:

$$E_{\text{CBM/VBM}} = E_{\text{BGC}} \pm \frac{1}{2} E_{\text{g}}. \tag{8.2}$$

This method takes advantage of the observation that the band gap center energy is relatively insensitive to the exchange-correlation functional used [136, 2]. The approach also allows for the combination of different methods for the band gap center energy and the band gap. We calculate the energy difference between the

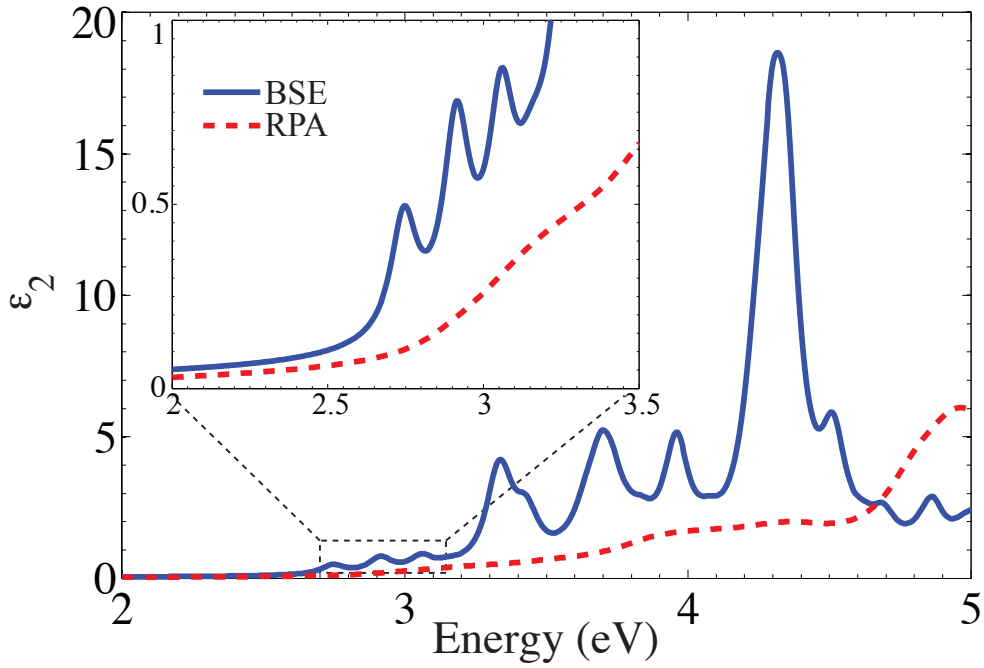

Figure 8.5: Imaginary part of the permittivity calculated with the BSE and RPA scheme. The inset shows a close-up of the first three BSE peaks. To compensate for the band gap underestimation using the PBE functional in the RPA calculation, we have shifted the spectra by 1.0 eV, which is the difference between the HSE06 and PBE band gaps.

band gap center and the vacuum level, which is obtained as the average electrostatic potential halfway in between the SnS_2 layers. For the HSE06 functional we obtain $E_{\mathrm{BGC}} = -6.16$ eV relative to the vacuum level and for the PBE functional we obtain $E_{\mathrm{BGC}} = -6.04$ eV. Similar to our previous study on group-III monochalcogenides [2], we observe that the band-gap center energy depends only weakly on the functional.

In a number of studies of various materials, including single-layer MoS_2 and bulk Ag_3PO_4, the band gap center energy is determined from the Mulliken electronegativity χ [172, 154, 173]. We test this phenomenological model for single-layer SnS_2 and calculate the Mulliken electronegativity χ of single-layer SnS_2

as the geometric mean $\chi = (\chi_{\mathrm{Sn}}^m \chi_{\mathrm{S}}^n)^{1/(m+n)}$ of the electronegativities of Sn and S atoms, χ_{Sn} and χ_{S}, respectively, with $m = 1$ and $n = 2$ for SnS_2 [174]. The Mulliken electronegativity of an atom is given by the average of the electron affinity and first ionization potential. Using experimental data for the electron affinity and ionization potential [150], we obtain a χ for SnS_2 of −5.47 eV. This empirical value significantly overestimates the band-gap center energy, indicating that the empirical model does not accurately predict the band-edge positions of single-layer SnS_2.

Figure 8.6 shows the band-edge positions of the CBM and the VBM obtained from Eq. (8.2) using the HSE06 band-gap center energy with the PBE and HSE06 fundamental gaps and the G_0W_0 quasiparticle gap. To determine the bias potential at which SnS_2 is able to photocatalytically split water, we compare the calculated band-edge positions with the reduction and oxidation potentials of water. These potentials depend on the pH value, i.e. the standard reduction potential for H^+/H_2 is $E^{\mathrm{red}}_{H^+/H_2} = -4.44\,\mathrm{eV} + \mathrm{pH} \cdot 0.059\,\mathrm{eV}$ [137]. In the experimental study of Ref. [45], the use of 0.5 M Na_2SO_4 electrolyte resulted in a pH value of 6.6. Using this value we obtain for the reduction potential $E^{\mathrm{red}}_{H^+/H_2} = -4.05\,\mathrm{eV}$ and for the oxidation potential $E^{\mathrm{ox}}_{O_2/H_2O} = -5.28\,\mathrm{eV}$.

The comparison of the water reduction and oxidation potentials with the band-edge positions of single-layer SnS_2 in Fig. 8.6 shows that although the VBM is energetically favorable for oxygen evolution, the CBM is insufficient to drive the hydrogen evolution. Therefore, an external bias potential is needed for photocatalytic water splitting. Such bias potentials decrease the efficiency for water splitting [155]. We find that a minimum bias potential of 0.9 V is required to shift the HSE06 CBM above the reduction potential of H^+/H_2. An additional

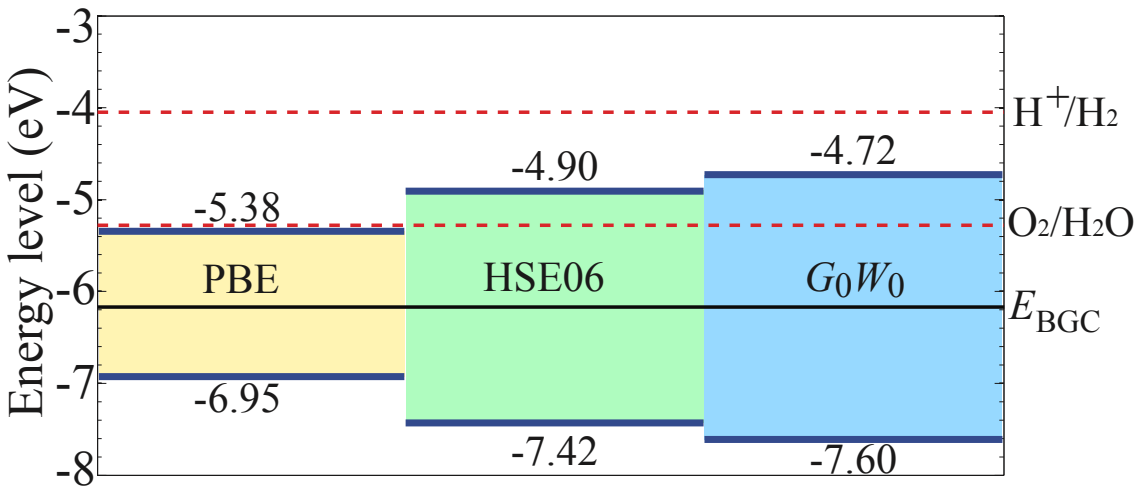

Figure 8.6: Energy diagram of single-layer SnS_2 with respect to normal hydrogen electrode level in electrolyte of pH = 6.6. The CBM and VBM energy levels are obtained from the HSE06 band gap center in combination with the band gaps from three different approaches including the PBE functional (1.57 eV) and the HSE06 functional (2.52 eV), and the G_0W_0 method (2.88 eV).

overpotential of the order of a few tenth of eV is required to overcome various activation barriers, with the overpotential for the hydrogen evolution reaction being typically smaller than the one for the oxygen evolution reaction [175]. Comparing the calculated minimum bias potential of 0.9 eV with the reported experimental bias potential of 1.0 eV [45] indicates a small overpotential for the hydrogen evolution for single-layer SnS_2, on the order of a tenth of an eV.

Strain engineering can be used to reduce the bias potential. Using the HSE06 functional, we predict that compressive strains are favorable. A 4% biaxial compressive strain decreases the band gap to 2.38 eV and increases the CBM and VBM band edges to −4.65 and −7.03 eV, respectively. This reduces the required bias potential for hydrogen evolution from 0.9 to 0.6 V and improves the efficiency for photocatalytic water splitting.

8.5 Summary

In summary, we have investigated several important aspects of using single-layer SnS_2 as a photocatalyst for water splitting. We show that single-layer SnS_2 has a low formation energy relative to bulk SnS_2, is dynamically stable, and stable in aqueous solution. By solving the Bethe-Salpeter equation, we obtain an optical band gap of 2.75 eV and an exciton binding energy of 0.41 eV. The optical band gap lies within the range of visible light, implying that a significant fraction of solar light can be harvested by single-layer SnS_2. Finally, we show that a bias potential of at least 0.9 V is needed for the water splitting to proceed and that compressive strains can reduce the required bias potential. Overall, our simulation results support the experimental finding that single-layer SnS_2 is a promising photocatalyst for water splitting [45].

CHAPTER 9

CHARGE-DENSITY WAVE DRIVEN PHASE TRANSITIONS IN SINGLE-LAYER MoS_2

9.1 Abstract

The electronic properties of single-layer MoS_2 make it an ideal two-dimensional material for application in electronic devices. Experiments show the MoS_2 can undergo structural phase transitions, however, the transformation mechanisms and their effect on the electronic structure are not yet understood. We reveal by density-functional calculations that charge doping can induce the phase transition of single-layer MoS_2 from the $2H$ to the $1T$ structure. Further, the $1T$ structure undergoes a second phase transition due to the occurrence of charge-density wave (CDW). By comparing the energies of several possible resulting CDW structures, we find that the $\sqrt{3}a \times a$ orthorhombic structure is the most stable one, consistent with experimental observations. Moreover, we discover that the band structure of the $\sqrt{3}a \times a$ structure possesses a Dirac cone, which is split by spin-orbit coupling interactions into a bandgap of 50 meV. We show that the underlying CDW transition mechanism is not electronic in nature, but nonetheless can be controlled by charge doping. Finally, we calculate the interface energy and band offsets of a lateral heterostructure formed by the $2H$ and $\sqrt{3}a \times a$ structures.

9.2 Introduction

Transition-metal dichalcogenides MX_2 exhibit a variety of polytypes due to their unique layered structures and weak interlayer van der Waals interactions [144]. When the dimensionality is reduced to two, the structures of single-layer MX_2 appear equally diverse. For instance, single-layer MoS_2, an actively investigated member of the MX_2 family for electronic applications [3], can occur in three crystal structures, the $2H$, $1T$, and $1T'$ structures [159]. Most studies focus on the ground state $2H$ structure shown in Fig. 9.1(a) where the top and bottom sulfur sublayers are in an eclipsing configuration [56]. Recent experiments showed that single-layer MoS_2 in the $1T$ structure illustrated in Fig. 9.1(b) can function as an efficient catalyst for the hydrogen evolution reaction [176]. In the $1T$ structure the top sulfur sublayer is displaced with reference to the bottom one by $1/3(\vec{a}_1+\vec{a}_2)$, where $\vec{a}_1$ and $\vec{a}_2$ are the in-plane lattice vectors.

Previous experiments identified two phase transitions in single-layer MoS_2 [159]. First, the semiconducting $2H$ structure is transformed to the metallic $1T$ one. Given the large energy difference and barrier between the $2H$ and $1T$ structures [56], the mechanism of this phase transition, however, remains unclear. Second, the $1T$ structure is further reconstructed to the $1T'$ superlattice structure, which is a modulated $1T$ structure that emerges *only* from the precursor metallic state and not from the semiconducting one [159], suggesting the possibility of a charge density wave mechanism as is seen in many three-dimensional metallic chalcogenides that are isostructural to single-layer MoS_2 [177].

In this work, we employ density-functional theory to elucidate the mecha-

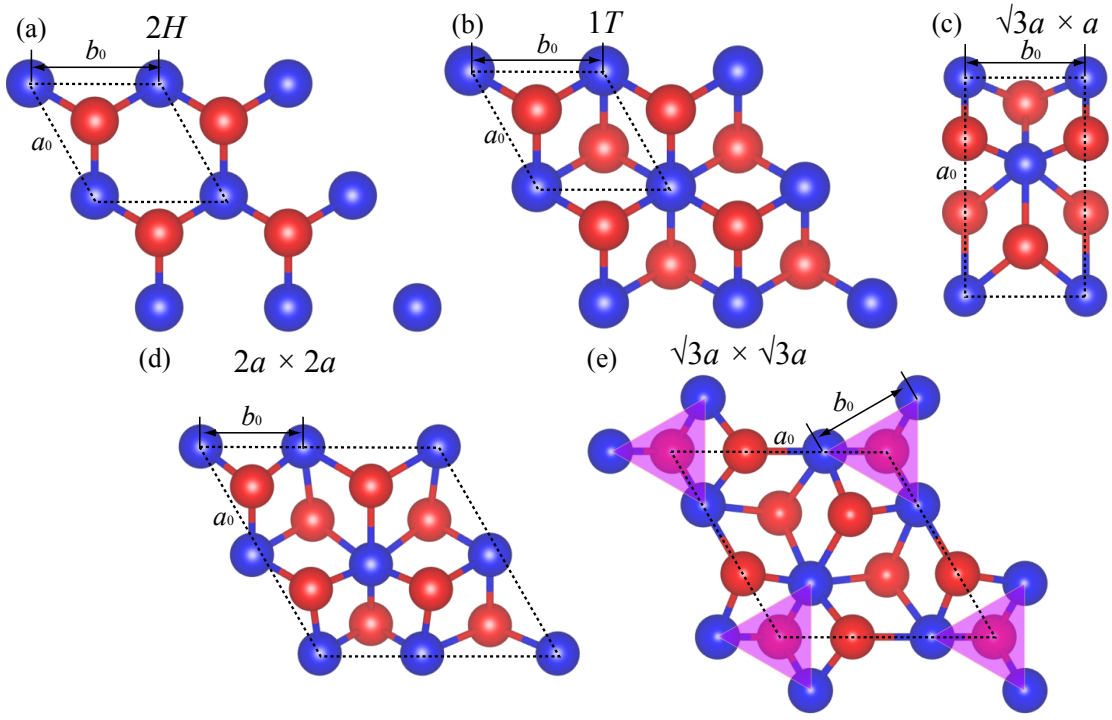

Figure 9.1: Atomic structures of single-layer MoS_2.The unit cells are enclosed by dashed lines. Molybdenum and sulfur atoms are represented by blue and red balls, respectively.

nism of the two phase transitions in single-layer MoS_2 and their effect on the electronic properties. We analyze the effect of charge doping, which has been found to strongly affect various materials' properties such as mechanical and magnetic behaviors [178, 179]. We find that charge doping reduces the barrier of the 2*H* to 1*T* phase transition, as well as the energy difference between the two structures. Furthermore, we show that the transition to the 1*T*′ state opens a gap at the Femi level in a typical CDW-like manner, but that soft modes driven by a strong *non-nesting* electron-phonon mechanism are the underlying cause of the instability. Our calculations show that this second transition can also be controlled by charge doping which provides a possible route to both promote the transition from 2*H* to 1*T* and stabilize the 1*T* structure against the CDW

Table 9.1: Structural parameters, energies, and fundamental bandgaps of single-layer MoS_2 with various structures. The parameters a_0 and b_0 for each structure are denoted in Fig.9.1. All energies E_{ref} are with reference to the energy of MoS_2 with the $2H$ structure and are in units of eV/atom. The bandgaps E_g with and without spin-orbit coupling are calculated with the PBE functional.

Structure	a_0	b_0	E_{ref}	$E_g^{w/o\ SOC}$	$E_g^{w/SOC}$
$2H$	3.18	3.18	0	1.67	1.60
$1T$	3.18	3.18	0.28	0	0
$\sqrt{3}a \times a$	5.72	3.18	0.18	0	0.05
$2a \times 2a$	6.44	2.77	0.21	0.14	0.10
$\sqrt{3}a \times \sqrt{3}a$	5.67	2.83	0.22	0.57	0.57

transition, thereby preserving the metallicity.

Studying the stability of metallic single-layer MX_2 is of critical importance as it becomes increasingly useful as an alternative to graphene as metallic leads for van der Waals heterostructures [180]. Therefore, for the second phase transition, we compare the stability of several CDW reconstructions originating from $1T$ single-layer MoS_2 and characterize their electronic structures. We confirm that the $1T'$ structure, i.e. a $\sqrt{3}a \times a$ orthorhombic reconstruction, is the most stable one, consistent with experimental results. Surprisingly, the band structure of the stable $\sqrt{3}a \times a$ structure exhibits a Dirac cone, split only by spin-orbit coupling interactions, indicating the possibility of topological insulator behavior in $1T'$ single-layer MoS_2. Finally, we study the electronic structure of the interface of the lateral heterostructure between $2H$ and $1T'$ in single-layer MoS_2 and determine the band offset.

9.3 Methods

We perform density-functional theory (DFT) calculations using the projector augmented wave method as implemented in the plane-wave code VASP [57, 101] and the PBE exchange-correlation functional [61]. For all calculations, a cutoff energy of 600 eV for the plane-wave basis set ensures an accuracy of the energy of 1 meV/atom. The k-point sampling uses the Monkhorst-Pack scheme [81] and employs for single-layer $2H$ and $1T$ MoS_2 a $48 \times 48 \times 1$ mesh and a $48 \times 48 \times 7$ mesh for the density of states calculations using the tetrahedra method. The k-meshes used for the other structures are given in Appendix D. For the single-layer MoS_2 calculations, a periodic spacing of 18 Å between the MoS_2 sheets ensures that the interactions between the layers are negligible.

To simulate the charge doping, we modify the number of valence electrons to a neutral system using a uniformly charged background. This method has been widely used in other systems [178]. Consequently, adding or removing electrons implies n-type and p-type doping, respectively.

The calculations of the phonon spectra are performed using the PHONOPY program [117] with the interatomic force constants calculated by VASP with the linear-response method based on the density-functional perturbation theory (DFPT) [59, 101].

9.4 Results

We first determine the structural parameters and ground state energies of single-layer MoS_2 with both the $2H$ and $1T$ structures. Table 9.1 lists the struc-

tural parameters calculated with the PBE functional. As can be seen, the lattice constants of the 2H and 1T structures are almost identical, facilitating the formation of a coherent interface as observed in the experiment [159]. However, the energy difference between the two structures is as large as 0.28 eV/atom.

In addition to the calculations of energy difference, we utilize the nudged elastic band method to determine the energy barrier between the 2H and 1T structures [181, 182]. Figure 9.2 shows the energy difference between the 1T and the 2H structure as a function of reaction coordinate and doping, i.e. the number of added or removed electrons. Without charge doping, we obtain an energy barrier of 0.52 eV/atom, much larger than the thermal energy of 25 meV/atom. On the other hand, the energy barrier from the 1T to 2H structures is slightly smaller than 0.24 eV/atom, but still significantly larger than the thermal energy. Therefore, once the 1T structure is formed, it may be kinetically stabilized and not easily transform back into the 2H structure. The latter energy barrier is also comparable to that of 0.33 eV/atom calculated for the same phase transition in single-layer WS_2 [183].

Electronic doping affects both the energy difference as well as the energy barrier.This is exemplified by the doping effects on the martensitic transformation from α to ω titanium [184]. Figure 9.2 illustrates that the energy barrier is drastically reduced due to either n or p-type doping. Furthermore, the energy difference between the 2H and 1T structures decreases as the number of electrons either increases or decreases. Therefore, charge doping facilitates the phase transition from the 2H to the 1T structure. This is similar to the proposed charge-transfer mechanism contributing to the 2H-to-1T phase transition in MoS_2 nanotubes [185]. However, our finding provides a somewhat more gen-

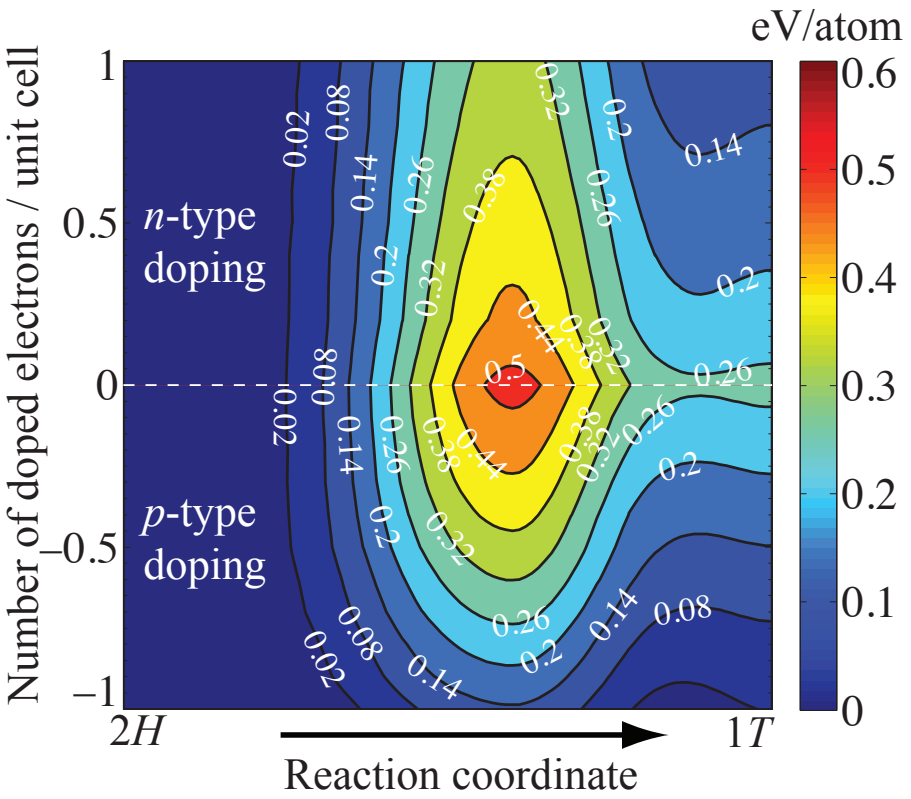

Figure 9.2: Energy difference between the 1*T* and the 2*H* structure as a function of reaction coordinates and number of doped electrons per unit cell.

eral mechanism of phase transition. This mechanism may also apply to other single-layer materials such as WS_2. In practice, the change of the number of electrons can be realized by several commonly used methods such as lithium intercalation [176] or *in situ* transition electron microscopy under high electron beam doses [186].

We then characterize the electronic structure of 1*T* MoS_2. Figure 9.3(a) displays the band structure of single-layer MoS_2 within the 1*T* structure. Three bands crossing the Fermi level confirm that the 1*T* MoS_2 exhibits a metallic behavior. Figure 9.3(b) shows the Fermi surface of 1*T* single-layer MoS_2. The Fermi surface consists of several features including two nearly circular loops

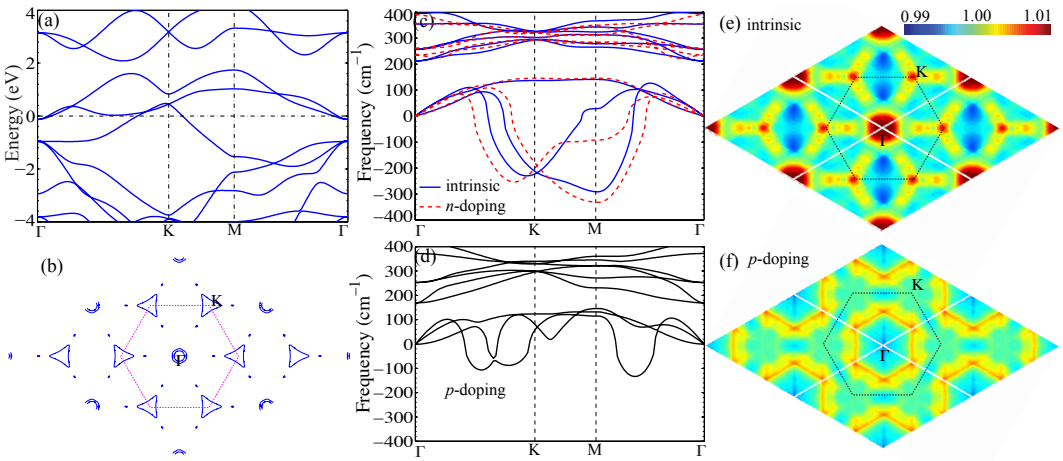

Figure 9.3: (a) Band structure and (b) Fermi surface of 1T single-layer MoS_2. Phonon spectra of intrinsic and n-type doped 1T MoS_2 are shown in panel (c), while the panel (d) shows the phonon spectrum of p-type doped 1T MoS_2. The real part of the electric susceptibility of intrinsic and p-type doped 1T MoS_2 are shown in panels (e) and (f), respectively.

around the Γ point and ellipse along the Γ to K points. More interestingly, we observe that the two triangular Fermi surfaces around neighboring K points are almost parallel to each other, giving rise to a significant nesting defined as the superposition of Fermi surfaces when a piece of them is translated to another one by a nesting vector $\mathbf{q}$ [187]. Fermi surface nesting is often cited as a determining factor in the stability/instability of metallic MX_2 [188], toward CDW formation, though we argue here that this is not the case for single-layer MoS_2.

To determine the dynamical stability of 1T single-layer MoS_2 we calculate the phonon spectrum. Fig. 9.3(c) shows that 1T single-layer MoS_2 exhibits two dynamically unstable acoustic phonon branches with imaginary frequencies throughout a significant portion of the spectrum, with the strongest softening near the M point. This is in contrast to 2H MoS_2 which is dynamically stable (see Fig.D.3 in Appendix D).

The phonon spectra of intrinsic $1T$ single-layer MoS_2 are affected differently by electron and hole doping. For n-type doping with 0.5 electrons per unit cell, the phonon spectrum displayed in Fig. 9.3(c) shows visible, but minor differences from the intrinsic phonon spectrum. In contrast, the p-doped phonon spectrum shown in Fig. 9.3(d) illustrates a drastic reduction in the magnitude of unstable phonon frequencies. Therefore, p-type doping is not only more effective in reducing the energy barrier between the $2H$ and $1T$ structures (see Fig. 9.2), but also acts against the phonon softening that destabilizes the $1T$ phase.

The phonon mode of intrinsic $1T$ single-layer MoS_2 at the M point implies a commensurate reconstructed structure, however, the dynamical instability in the second unstable acoustic branch disturbs this simplicity. In other words, the numerous wavevectors at which the phonon modes become imaginary yield few clues as to the final stable reconstruction. Therefore, we test three CDW structures found for 3D MoS_2 in the literature, i.e. the $\sqrt{3}a \times a$ [189], $2a \times 2a$ [190] and $\sqrt{3}a \times \sqrt{3}a$ structures [191, 192]. Here, a is the nearest Mo-Mo bond length or the lattice constant of undistorted $1T$ MoS_2.

The atomic positions of these three structures after geometry optimizations are illustrated in Fig.9.1(c)-(e). Unlike the other two structures without a clusterization of Mo atoms, the neighboring three Mo atoms form a trimer in the $\sqrt{3}a \times \sqrt{3}a$ structure. Symmetry analysis shows that the $\sqrt{3}a \times a$ structure has symmetry group number of 6 (Pm), whereas both the $2a \times 2a$ and $\sqrt{3}a \times \sqrt{3}a$ structures have group numbers of 157 (P31m) [193].The corresponding structural parameters denoted as a_0 and b_0 in Fig.9.1 are listed in Tab.9.1. Note that the ratio between a_0 and b_0 in fact slightly deviates from the ideal $\sqrt{3}$ in the

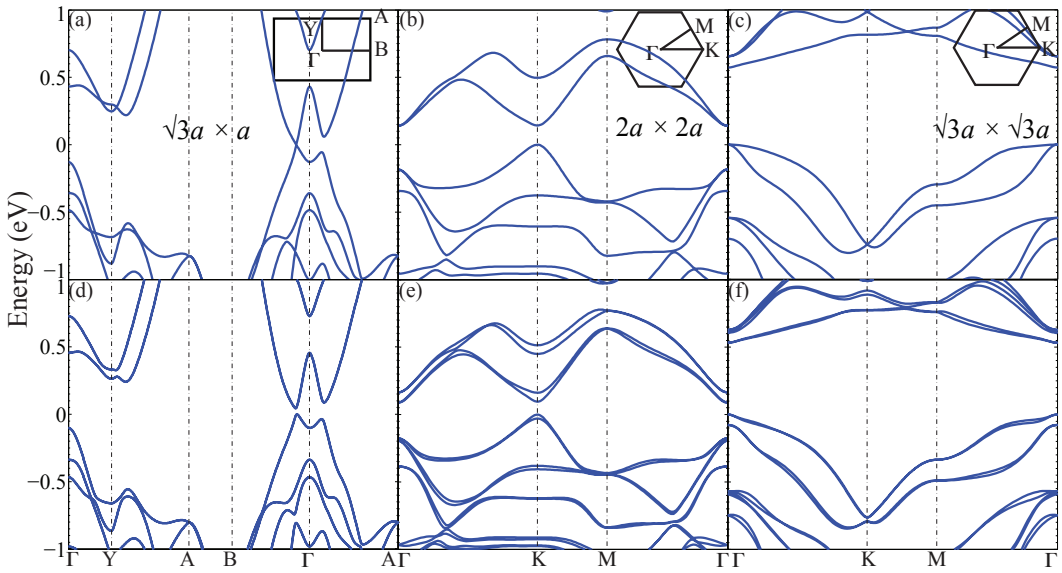

Figure 9.4: (a)-(c) Band structures of 1T single-layer MoS_2 with three reconstructed CDW structures. The corresponding band structures with spin-orbit coupling are shown in panels (d)-(e). Valence band maximum is set to zero. Common notations for the high symmetry k points are used.

$\sqrt{3}a \times a$ structure.

Table 9.1 reports the energies of the $\sqrt{3}a \times a$, $2a \times 2a$, and $\sqrt{3}a \times \sqrt{3}a$ structures with reference to the 2H structure. The similarity in energies of these three structures may explain why all these structures can be observed in the experiments of 3D MoS_2 [189, 190, 191, 192].The $\sqrt{3}a \times a$ structure has the lowest energy, consistent with the experimental observation in single-layer MoS_2 [159]. A similar CDW structure has also been discovered in single-layer WS_2 [183].

Figure 9.4(a)-(c) depict the band structures of the $\sqrt{3}a \times a$, $\sqrt{3}a \times \sqrt{3}a$, and $2a \times 2a$ structures. The corresponding total density of states calculated with tetrahedron method is shown in Appendix D. For the $\sqrt{3}a \times a$ structure, no electron states are found at the Fermi level, and a surprising Dirac-cone is formed between the B and M points. In contrast, for the $2a \times 2a$ and $\sqrt{3}a \times \sqrt{3}a$ structures,

they are semiconducting with their direct bandgaps summarized in Tab.9.1.

Spin-orbit coupling (SOC) affects the electronic structures of single-layer transition-metal dichalcogenides [194]. To this end, we test whether the SOC also modifies the electronic structures of the above three reconstructed structures. Including the spin-orbit coupling (SOC) separates the Dirac cone of the $\sqrt{3}a \times a$ structure, opening a bandgap of around 50 meV, as seen in Figure 9.4(d). The bandgap opening due to SOC is interesting, as it may be related to recently predicted two-dimensional topological insulators [195]. Figure 9.4(e) shows that SOC also decreases the bandgap of the $2a \times 2a$ structure. However, the bandgap of the $\sqrt{3}a \times \sqrt{3}a$ structure, illustrated in Figure 9.4(f), is almost unaffected by the SOC.

Having confirmed the stability of the $1T'$ structure, we note that FS nesting will peak near the K point of the Brillouin zone (corresponding to translating the flat sides of the Fermi surface triangles into one another), whereas the realized $\sqrt{3}a \times a$ corresponds to $q = M/2$ in reciprocal space. This means that nesting itself is clearly unrelated to the eventual structural transition.

As suggested in previous works on CDW formation, the Fermi surface is only a small part of the energy range from which weight in the susceptibility is gathered [196, 187]. We therefore calculate the full real part of the susceptibility, which is the relevant quantity for electronically driven CDW formation and which may contain peaks at substantially different vectors than the FS nesting alone. This quantity, $\chi'(\mathbf{q})$ is given as:

$$\chi'(\mathbf{q}) = \sum_{\mathbf{k}} \frac{f(\varepsilon_{\mathbf{k}}) - f(\varepsilon_{\mathbf{k+q}})}{\varepsilon_{\mathbf{k}} - \varepsilon_{\mathbf{k+q}}}, \tag{9.1}$$

where $\varepsilon_{\mathbf{k}}$ and $\varepsilon_{\mathbf{k+q}}$ are band energies at the wave vectors of **k** and **k+q**, respectively and the numerator is the difference between Fermi functions at those energies. Figure 9.3(e) shows the calculated $\chi'(\mathbf{q})$ for 1T MoS_2.

Though strong peaks are clearly visible in $\chi'(\mathbf{q})$, they are still mainly at the K point or along $\Gamma - K$ and are still unrelated to the observed modulation vector. This definitively eliminates a purely electronic (Peierls-like) mechanism for the transition to the CDW 1T' structure. The electronic structure could, however, still be an important ingredient, entering through the electron-phonon coupling that softens the phonons. For instance, the nesting term given in Eq. D.1 enters directly into λ, the electron phonon coupling constant relevant to superconductivity, and the phonon renormalization (softening) that can result, eventually, imaginary frequencies is proportional to $\chi'(\mathbf{q})$. The prevalent softening of the phonons around the K point seen in the spectrum of Figure 9.3(c) may therefore stem from structure in $\chi'(\mathbf{q})$. However, the equal or stronger softening elsewhere that gives rise to the 1T' structure cannot be related to $\chi''(\mathbf{q})$ or $\chi'(\mathbf{q})$ and is more likely the result of strengthened electron-phonon matrix elements, as has been experimentally and theoretically seen in other phonon spectra [197].

The effect of n-type doping on the nesting and on the phonon spectra of 1T MoS_2 is weak, whereas p-type doping significantly decreases the nesting and to the weak effect that n-type phonon spectrum of 1T MoS_2, the FS nesting is almost unaffected by n-type doping. However, p-type doping significantly decreases the nesting peaks (not shown) and the corresponding peaks in $\chi'(\mathbf{q})$, as seen in Figure 9.3(f) and furthermore acts toward stabilization of phonons across the entire spectrum. This again supports our suggestion that p-type doping is a more effective strategy to stabilize the 1T structure.

Finally, we investigate the effects of the presence of the $\sqrt{3}a \times a$ structure on the energetics and electronic structures of $2H$ MoS_2. To simulate the interface structure, we construct a supercell from nine rectangular cells of each structure, leading to two interfaces due to the periodic boundary condition. Figure D.6 in Appendix D shows the relaxed interface structure. We determine the interface energy as 0.17 eV/Å, much smaller than the calculated grain boundary energies of at least 0.35 eV/Å [198].This implies that forming the $2H/1T'$ interface is more favorable than creating different grain boundaries.

Figure 9.5 shows the local density of states (LDOS) of a formula unit of $2H$ MoS_2, which is sufficiently far (> 2.5 nm) away from the interface to model pure $2H$ single-layer MoS_2. The valence band offset (VBO) extracted from the LDOS is 0.32 eV. Correspondingly, the conduction band offset (CBO) or the Schottky barrier, is 1.58 eV when taking into account of the underestimation of the experimental bandgap by the PBE functional. The VBO and CBO represent the energy barriers to overcome for the carriers moving between the $2H$ structure and the $1T'$ one. Therefore, we expect that the appearance of the $1T'$ structure decreases the carrier mobility when $2H$ single-layer MoS_2 is used for electronic applications such as nanotransistor.

9.5 Summary

To conclude, we have studied two types of phase transitions in single-layer MoS_2. For the phase transition from the $2H$ to $1T$ structures, we find that charge doping of either type n or p lowers the transition barrier and induces the phase transition. For the phase transition from the $1T$ to $1T'$ superlattice structure, we

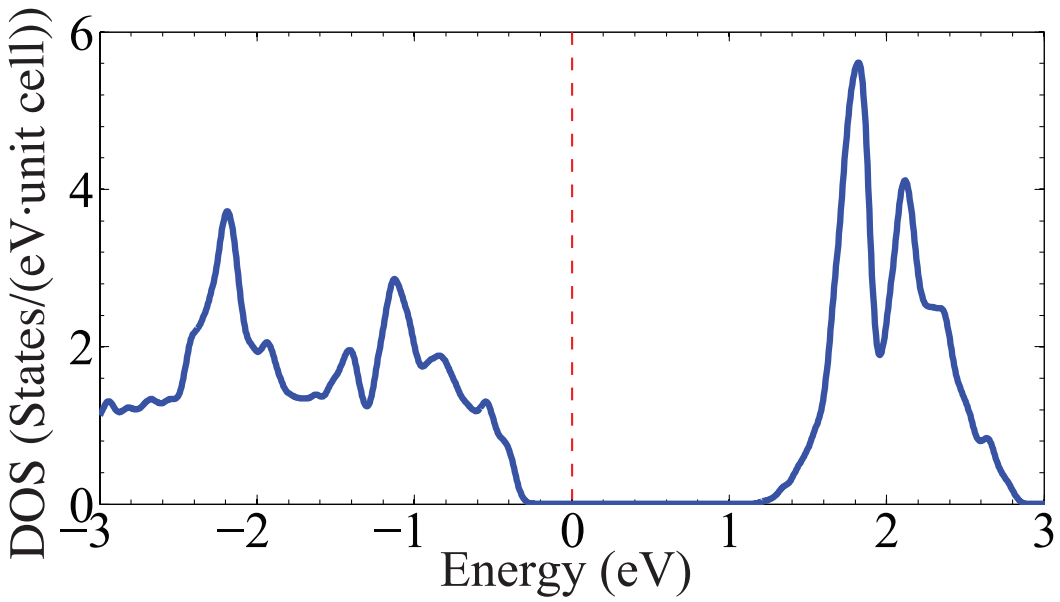

Figure 9.5: Local density of states of one unit of $2H$ single-layer MoS_2 which is far away from the interface of the $2H/1T'$ heterostructure.

show that the modulation must be induced by a strong electron-phonon coupling that is also manipulable by charge. For this transition, only p-type doping has an appreciable effect. The simultaneous existence of all three phases, $2H$, $1T$, and $1T'$, despite very high barriers at stoichiometry suggests that intrinsic charge doping may exist and that intentional p-type doping is a possible route towards stabilizing the metallic $1T$ phase against the other two gapped phases. Furthermore, we confirm that the $\sqrt{3}a \times a$ structure has the lowest energy, agreeing well with the experimental observation. The $\sqrt{3}a \times a$ structure additionally owns a Dirac cone in the band structure. The spin-orbit coupling splits the Dirac cone, implying a topological-insulator behavior. Finally, we estimate the energy barriers met by the charge carriers in the $2H/1T'$ heterostructure.

CHAPTER 10

COMPUTATIONAL PREDICTION AND CHARACTERIZATION OF SINGLE-LAYER CrS_2

10.1 Abstract[1]

Using first-principles calculations, we predict a previously unreported bulk CrS_2 phase that is stable in the 2*H* structure against competing phases and that single-layer CrS_2 exhibits a competitively low formation energy and is dynamically stable. We characterize the electronic, optical, and piezoelectric properties of this not yet synthesized single-layer material and reveal that it bears both similarities and differences compared to single-layer MoS_2. Like single-layer MoS_2, CrS_2 has a direct bandgap and valley polarization. However, the direct optical bandgap of CrS_2 is smaller with a value of 1.3 eV, close to the ideal bandgap of 1.4 eV for photovoltaic applications. Moreover, the calculated optical spectrum shows stronger optical absorbance. Applying compressive strain further increases the optical absorbance and bandgap, transforming it into a promising photocatalyst for solar water splitting. Finally, we show that single-layer CrS_2 possesses superior piezoelectric properties to single-layer MoS_2.

10.2 Introduction

Immense attention has recently been directed toward the search for novel, perfectly 2D materials [49, 2, 56]. Among the various strategies employed to screen

[1]Reprinted with permission from: H. L. Zhuang, M. D. Johannes, M. Blonsky, and R. G. Hennig. submitted to Appl. Phys. Lett. Copyright 2013 by American Institute of Physics.

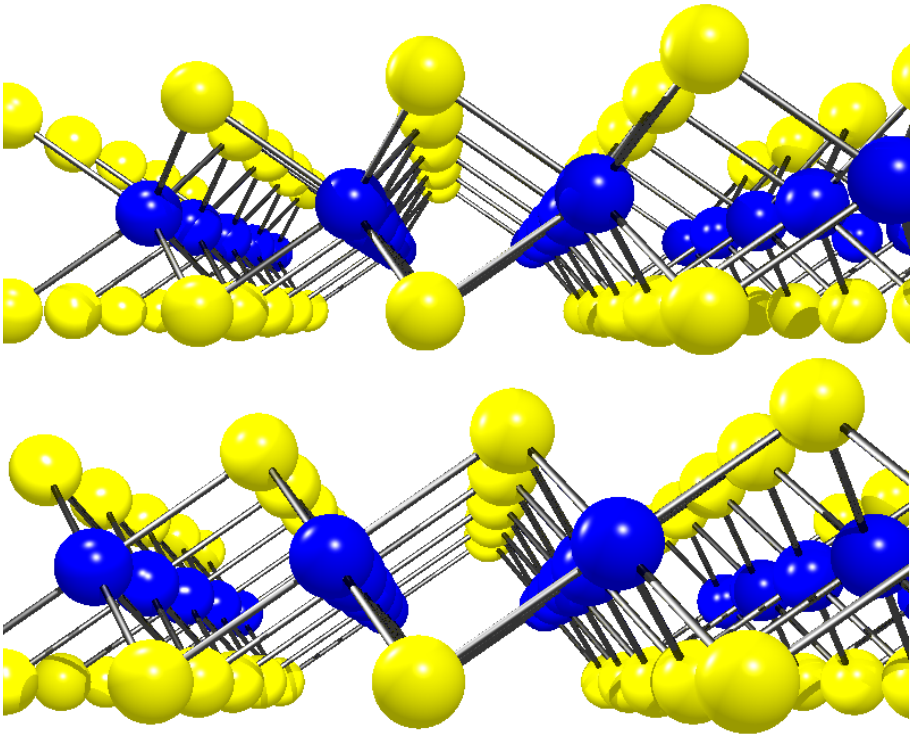

Figure 10.1: Ball-and-stick model of single-layer CrS_2 with the 2*H* (top) and 1*T* (bottom) structures. Chromium and sulfur are represented by the blue and yellow balls, respectively.

for promising 2D materials [50, 55, 19, 54], one common method is systematically exploring the periodic table, e.g., by replacing one element in an existing single-layer material with another element in the same group. This method has led to the successful prediction of silicene [52].

Single-layer transition-metal dichalcogenides such as MoS_2 and WS_2 have been the subjects of a wealth of studies [32]. As chromium belongs to the same group as molybdenum and tungsten, it is therefore natural to investigate the possible stability of single-layer CrS_2 and its potentially interesting and useful properties such as electronic, optical, and piezoelectric.

In this paper, we address the stability of single-layer CrS_2 from energetic,

mechanical, dynamical, and thermal perspectives. All stability metrics strongly suggest the feasibility of experimental synthesis of single-layer CrS_2 in the 2H structure. Regarding the electronic properties of single-layer CrS_2, we clarify previous contrasting conclusions, i.e. Lebègue *et al.* claim that single-layer CrS_2 is a metal [49], whereas Ataca *et al.* determine it as a semiconductor with a bandgap of 1.07 eV [50]. Using a hybrid density functional we show that, similar to MoS_2, single-layer CrS_2 with the 2H structure is semiconducting whereas the 1T structure is metallic. Both of the 2H and 1T structures are illustrated Fig. 10.1. As for the optical properties, we show that single-layer CrS_2 exhibits similar valley polarization to that of single-layer MoS_2. In addition, by solving the Bethe-Salpeter equation, we determine the optical bandgap of single-layer CrS_2 as 1.3 eV, close to the ideal bandgap of 1.4 eV for photovoltaic application. Furthermore, single-layer CrS_2 has a slightly higher optical absorbance than single-layer MoS_2. Mechanical strains can not only tune the bandgap and optical absorbance of single-layer CrS_2, but also enable it to be a potential photocatalyst for solar water splitting. Finally, we show that CrS_2 exhibits remarkable piezoelectric properties.

10.3 Methods

We perform density-functional theory (DFT) calculations using the projector augmented wave method as implemented in the plane-wave code VASP [59, 77, 78]. We use the PAW potentials optimized for *GW* calculations that describe the $1s^2 2s^2 2p^6$ electronic states as core states for both Cr and S. For the structural relaxations we employ the Heyd-Scuseria-Ernzerhof (HSE06) hybrid functional [61, 63]. For the phonon calculations, we use a cutoff energy of 600 eV to

ensure the convergence, particularly of the low-energy phonon modes. For all other calculations, a cutoff energy of 400 eV for the plane wave basis set is used to ensure an accuracy of the energy of 1 meV/atom. The k-point sampling uses the Monkhorst-Pack scheme [81] and employs for the single-layer materials a $48 \times 48 \times 1$ mesh for the PBE functional and an $18 \times 18 \times 1$ mesh for the more expensive HSE06 and G_0W_0 calculations. For the single-layer CrS_2 calculations a vacuum spacing of 18 ensures that the interactions between the layers are negligible.

We calculate the imaginary part of the dielectric constant of single-layer CrS_2 by solving the Bethe-Salpeter equation (BSE) [65, 66]. The calculations are carried out based on the G_0W_0 quasiparticle energies and the HSE06 wavefunctions. Although using the HSE06 wavefunctions as a starting point for the G_0W_0 and BSE calculations is more computationally expensive, it is expected that this strategy provides a more accurate description of the electronic ground state [199]. For the G_0W_0 calculations, we use 192 bands and 128 frequency points. The ten highest valence bands and the ten lowest conduction bands are included in the BSE calculation of the excitonic states.

10.4 Results

10.4.1 Stability

Table 10.1 lists the structural parameters of single-layer CrS_2 for the $2H$ and $1T$ structures calculated with the HSE06 functional. The lattice constants and bond lengths are similar for both structures, which is also observed for other single-

Table 10.1: Structural parameters and formation energies of single-layer CrS_2 in the 2*H* and 1*T* structure. The structural parameters are calculated with the HSE06 functional and the formation energies with the HSE06, PBE, and opt-B88 van der Waals functionals. The structural parameters, in units of Å, include the lattice parameter a_0 and the spacing Δz between the Cr and the S atom layers. The formation energies are in units of eV/atom.

	a_0	Δz	E_f^{HSE06}	E_f^{PBE}	E_f^{vdW}
2*H*	2.99	1.45	-0.008	-0.003	0.075
1*T*	3.00	1.47	0.237	0.176	0.248

layer materials such as MoS_2 [56].

To test the energetic stability of single-layer CrS_2, we consider the energies of different competing Cr-S bulk phases. Surprisingly, neither the ASM Alloy Phase Diagram Database [200] nor the Inorganic Crystal Structure Database (ICSD) [100] show any phases with composition CrS_2. The ICSD displays an erroneous entry for CrS_2 that corresponds to the CrS_2 sublattice of the $YSCrS_2$ misfit layered compound [201]. Instead the listed competing bulk phases for single-layer CrS_2 are Cr_5S_8 and sulphur. Notably, Cr_5S_8 is a layered compound that corresponds to layers of 1*T* CrS_2 with additional intercalating Cr atoms.

We identify a previously unreported CrS_2 bulk phase that is energetically stable against the competing Cr-S phases and show that single-layer CrS_2 is close in energy to the stable CrS_2 bulk phase and lower in energy than the competing Cr-S phases. We find that bulk CrS_2 with the same structure as bulk 2*H* MoS_2 exhibits the lowest energy of various stackings of 1*T* and 2*H* CrS_2 layers. The energetic stability of bulk 2*H* CrS_2 against competing phases is given by the

reaction

$$5CrS_2(\text{bulk}) \rightleftharpoons Cr_5S_8(\text{bulk}) + 2S(\text{bulk}), \tag{10.1}$$

i.e. bulk CrS_2 is decomposed into bulk Cr_5S_8 and S with space groups of $C2/m$ and $P2/c$, respectively. To calculate the energy balance of the reaction, we employ the vdw-optB88 van der Waals functional to account for the dispersion interactions in bulk Cr_5S_8 [120]. We find that bulk $2H$ CrS_2 is energetically stable by 180 meV/atom and expect that it could be experimentally synthesized.

Next, we calculate the formation energy E_f of single-layer CrS_2 relative to the stable bulk CrS_2 compound using the formula $E_f = E_{2D} - E_{3D}$, where E_{2D} and E_{3D} are the energies of single-layer and bulk CrS_2, respectively. Table 10.1 reports the resulting formation energies of single-layer CrS_2 calculated with the HSE06, PBE, and vdW-optB88 functionals. We find for all three functionals that the single-layer $2H$ structure is more stable than the single-layer $1T$ structure, revealing that $2H$ CrS_2 is the single-layer ground state. The slightly negative formation energies of the single-layer $2H$ structure for the HSE06 and PBE functionals are unphysical, due to the lack of van der Waals interactions in these functionals. In addition to the $2H$ and $1T$ structures, we also consider a distorted octahedral structure resembling a single layer of bulk WTe_2 (ICSD number: 14348) [100]. This structure exhibits an energy as calculated by the PBE functional 95 meV/atom higher than the $2H$ CrS_2 ground state. Importantly, the formation energy of single-layer $2H$ $CrS_2$is lower than that of any other single-layer transition-metal dichalcogenide [56], indicating that it should be possible to experimentally synthesize single-layer CrS_2.

Given the much higher formation energy of $1T$ and distorted octahedral CrS_2, we henceforth narrow our focus on the $2H$ structure. We first determine

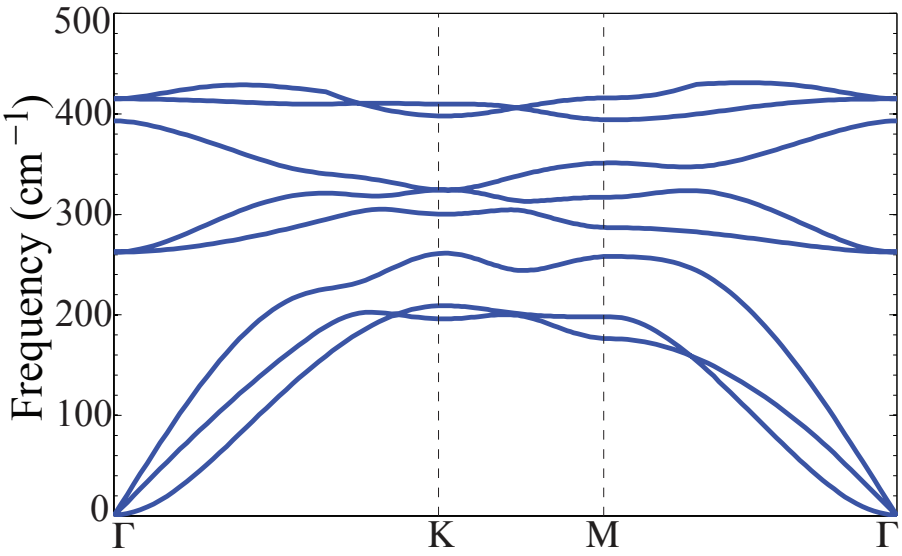

Figure 10.2: Phonon spectrum of single-layer 2*H* CrS_2.

the mechanical stability by calculating the two independent elastic constants of hexagonal 2*H* single-layer CrS_2,

$$C_{11} = \frac{1}{A_0} \cdot \frac{\partial^2 E}{\partial \epsilon_{11}^2} \tag{10.2}$$

and

$$C_{12} = \frac{1}{A_0} \cdot \frac{\partial^2 E}{\partial \epsilon_{11} \partial \epsilon_{12}}. \tag{10.3}$$

Here, E is the total energy of an orthorhombic unit cell employed for the calculations, and A_0 is the equilibrium area of single-layer CrS_2 in the orthorhombic cell. Table 10.2 summarizes the results of C_{11} and C_{12}. Compared to MoS_2, CrS_2 exhibits a smaller C_{11} and a similar C_{12} [35]. The elastic constants fullfil the Born criteria of stability for hexagonal structures, i.e. $C_{11} > 0$ and $C_{11} - C_{12} > 0$, which ensure that 2*H* single-layer CrS_2 is mechanically stable [202].

To determine the dynamical stability of single-layer CrS_2, we obtain its phonon spectrum using the force constants obtained for a 6×6×1 supercell [57, 101]. Figure 10.2 shows the phonon spectrum of single-layer CrS_2. We observe

no imaginary frequencies, confirming the dynamical stability of single-layer CrS_2.

We further test the stability of 2*H* single-layer CrS_2 by performing *ab initio* molecular dynamics (MD) simulations at 600 K for 3 ps using a $6 \times 6 \times 1$ supercell and a time step of 1 fs. The canonical ensemble (*NVT*) is used for the MD simulations. The structures at the end of the MD simulations show no structural transitions, indicating that single-layer CrS_2 is stable at a temperature of 600 K.

The low formation energy of 2*H* single-layer CrS_2 and its mechanical, dynamical, and thermal stability suggest the feasibility of the experimental synthesis of single-layer CrS_2. However, since there is no stable 3D layered counterpart of 2*H* CrS_2 available for mechanical exfoliation, single-layer CrS_2 must be grown by a chemical method such as chemical vapor deposition or molecular beam epitaxy.

10.4.2 Electronic Properties

We now turn to the characterization of the electronic properties of 2*H* single-layer CrS_2. Figure 10.3 shows the band structures of single-layer CrS_2 in the 2*H* and 1*T* structure obtained using the HSE06 functional. The band structure of 2*H* CrS_2 displays a direct fundamental bandgap of 1.48 eV, while 1*T* CrS_2 shows metallic behavior with two bands crossing the Fermi level. Therefore, we suggest that previous contrasting conclusions on whether single-layer CrS_2 is metallic or semiconducting are caused by the different structures used for the calculations.

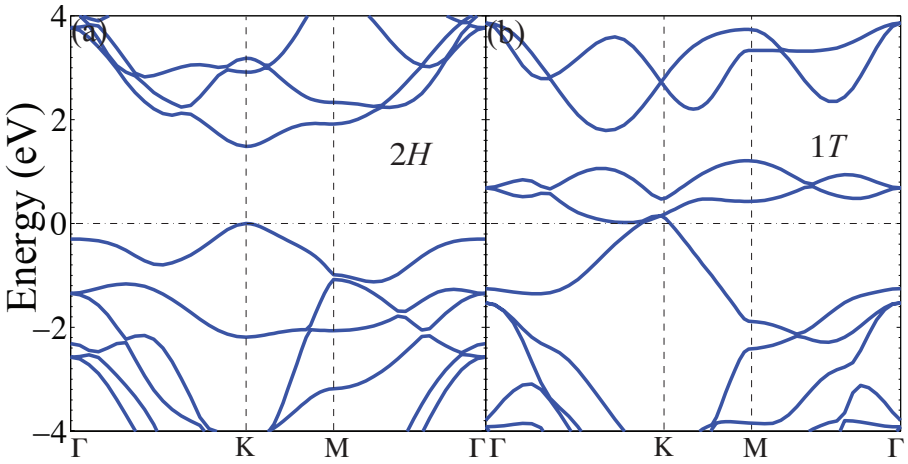

Figure 10.3: Band structures of single-layer CrS_2 for the (a) 2*H* and (b) 1*T* structure calculated with the HSE06 functional.

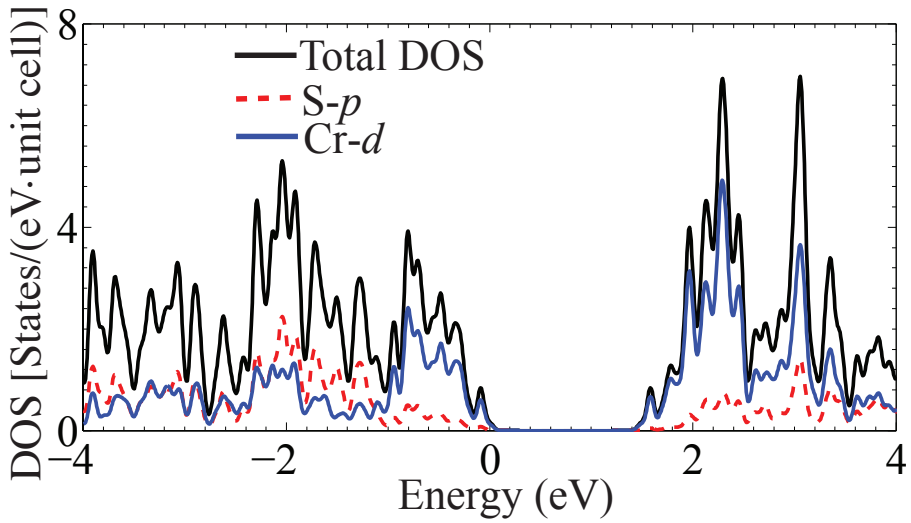

Figure 10.4: Total and projected electronic density of states of single-layer CrS_2 calculated with the HSE06 functional.

To understand the bonding characteristics of single-layer CrS_2, Fig.10.4 shows the total and projected density of states (TDOS and PDOS) within the energy window from −4 to 4 eV with reference to the valence band maximum. Similar to single-layer MoS_2, the entire energy window is dominated by the hybridizations between the S 3*p* and Cr 4*d* orbitals implying covalent bonding between S and Cr atoms. Furthermore, the TDOS of single-layer CrS_2 displays

several van Hove singularities, leading to a large joint density of states that results in the strong optical absorption discussed below [33].

10.4.3 Optical Properties

We now characterize the optical properties of single-layer CrS_2 first for circular polarized light. An important optical property is the degree of circular optical polarization $\eta(\mathbf{k})$ describing the $\mathbf{k}$-resolved chiral absorption selectivity of a honeycomb structure that lacks inversion symmetry [203]. $\eta(\mathbf{k})$ can be calculated by post-processing the optical matrix elements of the optical transitions between the top of the valence band and the bottom of the conduction band [203, 204]. Figure 10.5 shows $\eta(\mathbf{k})$ of single-layer CrS_2 in the reciprocal space. Similar to single-layer MoS_2 [203], we observe that $\eta = \pm 1$ at the K and K' points, corresponding to absorption of exclusively left and right-handed photons, respectively. As a result, single-layer CrS_2 is a promising candidate material for valleytronics applications.

Another critical optical property of single-layer materials is optical absorbance $A(\omega)$. For light with a polarization vector within the plane of the single-layer material, $A(\omega)$ is calculated by $A(\omega) = \omega/c \cdot L \cdot \epsilon_2$, where c is the speed of light in vacuum and L is the interlayer spacing (18 Å) between the isolated CrS_2 layers [123]. The imaginary part of the dielectric constant, ϵ_2, is calculated by solving the BSE.

Figure 10.6 shows the optical absorbance $A(\omega)$ of single-layer CrS_2 as a function of photon energy. The first two absorption peaks arise from the optical transition corresponding to the formations of excitons. Interestingly, the optical

bandgap of 1.30 eV is close to the ideal value of 1.4 eV for photovoltaic applications [205]. The optical absorption $A(\omega)$ of single-layer CrS_2 is about 5-12% over the energy range of visible light, larger than the absorbance of MoS_2 and single-layer graphene with $A(\omega)$ of 5-10% and 2.3%, respectively [206, 124]. Stronger optical absorbance indicates that single-layer CrS_2 is a better sunlight harvester.

Similar to the BSE optical spectrum of single-layer MoS_2 [133], the third peak in the spectrum of single-layer CrS_2 corresponds to the G_0W_0 bandgap of 1.75 eV. The resulting exciton binding energy is 0.45 eV. To test whether this lowest-energy exciton is accurately described by the Mott-Wannier model [165], we first determine the electron and hole effective masses at the K point as m_e = 0.65 and m_h = 0.67 m_0, respectively, where m_0 is the rest mass of the electron. These masses are slightly larger than those of single-layer MoS_2 with m_e = 0.60 and m_h = 0.54 m_0 [194]. We then follow the our previous approach of Ref.47 to determine the in-plane and out-of-plane relative permittivities $\epsilon_{\parallel}$ = 20.4 and $\epsilon_{\perp}$ = 2.2, respectively. This leads to the effective permittivity of ϵ_{2D} = 6.77. Applying the Mott-Wannier model to a 2D system, the first exciton binding energy is given as

$$E_0 = 4\frac{m_r}{m_0}\frac{R_\infty}{\epsilon_{2D}^2}, \tag{10.4}$$

where m_r is the reduced effective mass and R_∞ the Rydberg constant [170]. Using the values from above in Eq.10.4, we obtain E_0 = 0.4 eV, consistent with the excitonic binding energy calculated by solving the BSE. Therefore, we conclude that the exciton in single-layer CrS_2 is of the Mott-Wannier type.

Strain plays an important role in affecting the bandgaps and the optical absorbance of single-layer CrS_2. Similar to the strain effects on the bandgaps of single-layer MoS_2 [160], the bandgaps of CrS_2 increase with increasing com-

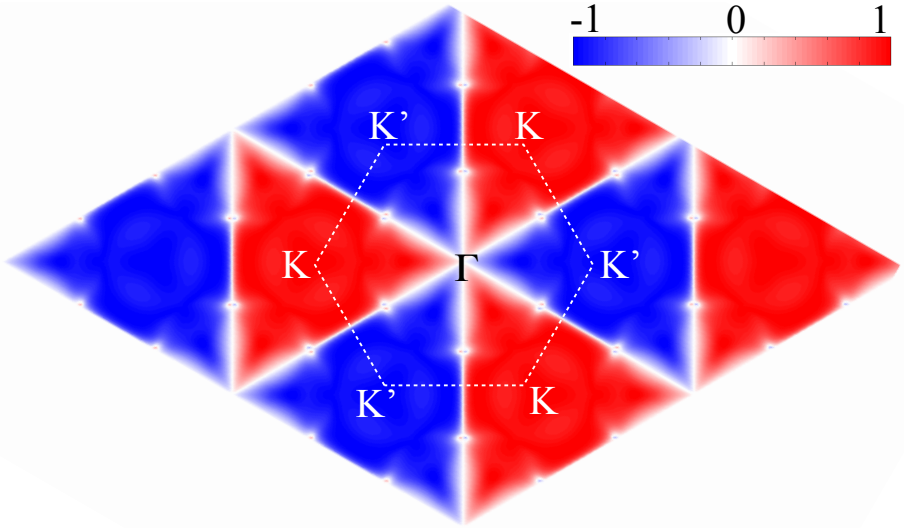

Figure 10.5: Degree of circular optical polarization $\eta(\mathbf{k})$ of single-layer CrS_2.

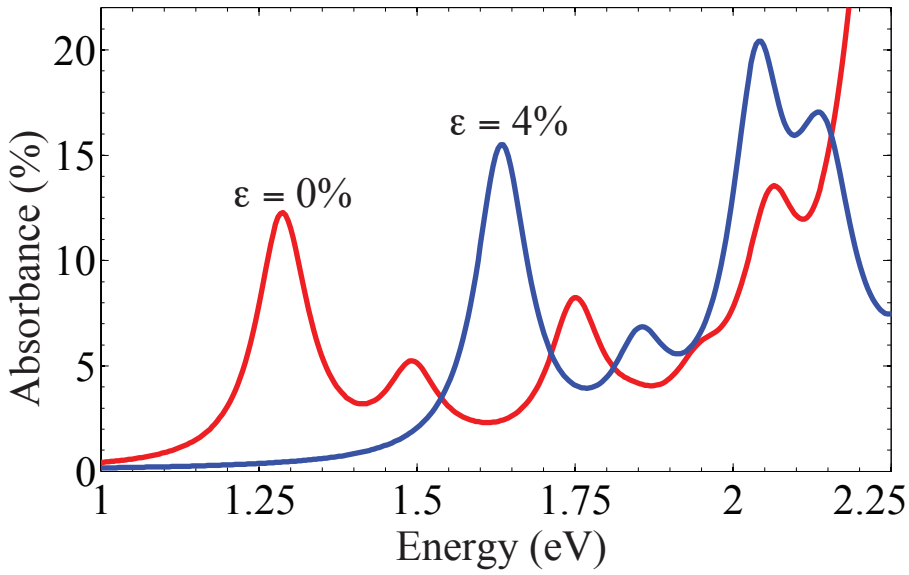

Figure 10.6: Optical absorbance for unstrained and compressively strained single-layer CrS_2 calculated using the BSE scheme.

pressive strains. For example, Fig. 10.6 shows that a compressive strain of 4% increases the optical bandgap to 1.64 eV and leads to an enhanced optical absorbance of 5-15%.

Since the optical bandgap and absorbance of single-layer CrS_2 is mechanically tunable, it is worthwhile exploring its potential for energy conversion applications, e.g., photocatalytic water splitting. To become a promising photocatalyst for water splitting, a material must satisfy two important criteria: (i) the bandgap of the semiconductor must be at least 1.6-1.7 eV and (ii) the band edges must straddle the redox potential energies of water, i.e. -4.44 eV and -5.67 eV for the hydrogen and oxygen evolution, respectively. Using the HSE06 functional we obtain -4.87 eV for the energy level of the conduction band minimum (CBM) and -6.17 eV for the valence band maximum (VBM) relative to the vacuum level. Clearly, the CBM is unable to drive the hydrogen evolution. Applying a compressive strain of 4% increases the CBM and VBM levels to -4.24 and -5.88 eV, respectively, perfectly straddling the redox potential energies of water with a similar overpotential of 0.2 eV for the hydrogen and the oxygen evolution. The bandgap type remains direct under compressive strain. Photocatalyst with direct bandgaps are generally preferred due to their better optical absorption. The fact that only few existing materials possess both a direct bandgap and suitable band edge positions underlines the importance of our prediction that strained single-layer CrS_2 is a potential photocatalyst.

Table 10.2: Elastic constants and piezoelectric coefficients of single-layer CrS_2. The elastic constants C_{11} and C_{12} are in units of N/m. The piezoelectric coefficients e_{111} and d_{111} are in units of 10^{-10} C/m and pm/V, respectively.

	C_{11}	C_{12}	e_{111}	d_{111}
CrS_2	120	32	4.72	5.36

10.4.4 Piezoelectric Properties

A recent study shows that transition-metal dichalcogenides possess sizable piezoelectric coefficients [35]. Additionally, the study predicts an interesting trend that the piezoelectric coefficients increase across each chalcogenide family from W to Mo. To this end, we expect that single-layer CrS_2 exhibits even larger piezoelectric coefficients than MoS_2 and WS_2. To corroborate this expectation, we calculate the piezoelectric coefficients e_{111} and d_{111} defined as $e_{111} = \frac{\partial P_1}{\partial \epsilon_{11}}$ and $d_{111} = \frac{e_{111}}{C_{11}-C_{12}}$, respectively. Here P_1 is the macroscopic polarization along the armchair direction of the lattice, and ϵ_{11} is the mechanical strain along the same direction. Several methods including the density functional perturbation theory (DFPT) and the modern theory of polarization (MTP) can be used to calculate P_1 [57, 207]. We employ the DFPT for the calculations of e_{111}. As a benchmark test, we determine e_{111} for single-layer MoS_2 as 3.48×10^{-10} C/m, in a good agreement with the reported 3.64×10^{-10} C/m calculated according to the MTP [35]. Table 10.2 shows that both piezoelectric coefficients, e_{111} and d_{111}, are significantly larger than those of single-layer MoS_2 [35], suggesting a stronger piezoelectric coupling in single-layer CrS_2.

10.5 Summary

We have predicted a previously unreported bulk CrS_2 phase that is stable in the 2*H* structure against competing phases and have shown that single-layer CrS_2 exhibits a competitive low formation energy and is mechanically, dynamically, and thermally stable. We find that single-layer CrS_2 has prominent electronic and optical properties, such as an optical bandgap of 1.30 eV, a direct fundamental gap of 1.75 eV, valley polarization, and strong optical absorbance. Applying compressive strains can tune the bandgaps and optical absorbance, such that single-layer CrS_2 could become a promising photocatalyst for water splitting. Finally, we predict large piezoelectric coefficients for single-layer CrS_2. We believe that our findings will stimulate experimental interests in synthesizing this single-layer material.

CHAPTER 11

OUTLOOK

Over the next decade, single-layer materials are expected to have a great impact on a wide range of applications from electronic devices to energy conversion. The procedure of computational characterization described in this paper enables the efficient screening of novel single-layer materials and provides valuable guidance for experimental efforts. In addition to these opportunities, four challenges arise that are described here.

First, as mentioned in Chapter 2, most of the input structures for computational simulations originate from their three-dimensional parent structures that can be found in the ICSD. The success of this approach relies somewhat on serendipity and there are likely many other single-layer materials awaiting discovery, whose structures and compositions have no three-dimensional counterparts. To this end, smarter structure-search algorithms such as genetic algorithm [208] are helpful to identify these 'orphan' single-layer materials.

Second, recent studies have shown that stacking different single-layer materials atop each other leads to van der Waals heterostructures that possess great promise for desired electronic properties [180]. Because of the non-epitaxial nature of these heterostructures, the requirement of periodic boundary conditions in computational characterization methods leads to the need to employ large commensurate simulation cells with a drastic increase in the number of atoms for the calculation. This increases the computational cost, which may make accurate calculations of electronic and optical properties with methods such as solving the BSE prohibitive.

Third, studying the interactions between single-layer materials and substrates would benefit from more accurate van der Waals functionals, which indeed remain a long-standing challenge to the computational materials community.

Finally, the computational tools employed in most studies of single-layer materials are limited to DFT-based techniques. However, other theoretical methods such as quantum Monte Carlo method and molecular dynamics simulations are also useful for characterizing single-layer materials. Therefore, it is necessary to incorporate a multi-scale modeling strategy into the framework shown in Fig. 2.1 in order to thoroughly characterize emerging single-layer materials.

The rapid emergence of novel single-layer materials, with a broad range of properties suitable for many applications, presents the exciting opportunity for materials science to explore an entirely new class of materials. This comes at the time when mature computational methods provide the predictive capability to enable the computational discovery, characterization, and design of single-layer materials and provide the needed input and guidance to experimental studies.

APPENDIX A

APPENDIX OF CHAPTER 5

Crystal structures and lattice parameters of bulk HgO. Table A.1 lists the calculated lattice parameters for different structures of HgO shown in the Inorganic Crystal Structure Database [100]. The space group information and lattice parameter are given for each phase, along with the Wyckoff positions for the atoms. As seen from the total energies, The *Imm*2 and $P\bar{1}$ phases are degenerate in energy and much higher in energy than the other phases, indicating that they are not stable structures. The orthorhombic *Pnma* phase is the most stable form of HgO. Therefore, its total energy is used as the reference energy to calculate the formation energy of single-layer HgO as reported in the text. In this phase, the experimental lattice constants are a = 6.613 Å, b = 5.521 Å and c = 3.522 Å and the experimental Wyckoff positions for the Hg and O atoms are Hg 4(c) 0.1136 0.2500 0.2456 and O 4(c) 0.3592 0.2500 0.5955 [100]. Our calculated lattice constants and Wyckoff positions are within 1.5% of the experimental values, verifying the refined crystal structure.

Band structures of single-layer oxides. We use the HSE06 functional to calculate the band structures of single-layer BeO, MgO, CaO, ZnO and HgO, which are shown in Fig. A.1

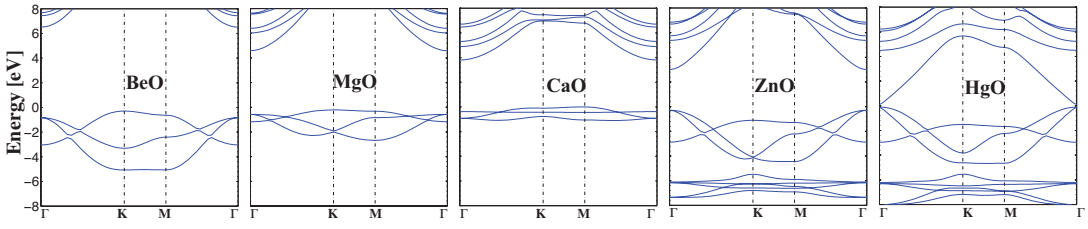

Figure A.1: Band structures of single-layer BeO, MgO, CaO, ZnO, and HgO.

Table A.1: Crystal structure and energy of various reported structures of HgO. The optimized lattice parameters are given in units of Å and the energy is given relative to the lowest energy structure with space group *Pnma* in units of eV per molecular unit of HgO.

Structures	Space group	*a*	*b*	*c*	E_{tot}	Wyckoff positions
orthorhombic	*Pnma* (62)	6.71	5.49	3.56	-5.653	Hg 4(c) 0.115 0.250 0.248
						O 4(c) 0.364 0.250 0.592
orthorhombic	*Imm*2 (44)	3.36	5.13	3.43	-5.421	Hg 2(a) 0.0 0.0 0.085
						O 2(b) 0.0 0.5 0.085
trigonal	$P3_221$ (154)	3.59	3.59	8.75	-5.645	Hg 3(a) 0.0 0.746 0.333
						O 3(b) 0.475 0.0 0.167
trigonal	$P3_121$ (152))	3.60	3.60	8.76	-5.649	Hg 3(a) 0.254 0.0 0.333
						O 3(b) 0.525 0.0 0.833
monoclinic	$P\bar{1}$ (2)	6.92	5.50	6.84	-5.421	Hg 2(i) 0.118 0.250 -0.126
						Hg 2(i) 0.117 0.250 0.373
						Hg 2(i) -0.382 0.251 -0.124
						Hg 2(i) -0.383 0.251 0.376
						O 2(i) 0.366 0.250 0.045
						O 2(i) 0.36491 0.250 -0.455
						O 2(i) -0.133 0.250 -0.296
						O 2(i) -0.134 0.251 0.204

Phonon spectra of single-layer oxides. Figure A.2 shows the calculated phonon spectra of the six single-layer oxides. The phonon spectra are determined using the Phonopy [117] package with the force constants calculated by density functional perturbation theory as implemented in VASP [57, 101]. We calculate the Born effective charges and the permittivity, and include them into the non-analytical term of the force-constant matrix. We use a cutoff energy of 500 eV to ensure convergence, particularly of the low-energy phonon modes. Our calculated phonon spectrum of single-layer ZnO agrees well with a previous study by Ciraci *et al*. [209] As can be seen, among all six single-layer oxides, only single-layer HgO is dynamically unstable. Following the unstable modes of HgO, we identify an 8-atom reconstruction that lowers the energy by 0.2 eV/atom resulting in a formation energy of only 11 meV/atom above the bulk phase. The band gap of the reconstructed HgO structure is 1.89 eV calculated with the PBE functional. Figure A.3 shows the reconstructed single-layer structure, which consists of parallel zig-zag lines of Hg and O atoms, similar to the bulk crystal structure of HgO.

Band alignment with reference to graphene. We calculate the valence band minimum (VBM) and conduction band maximums (CBM) of the single-layer oxides

Table A.2: Conduction band minimum and valence band maximums (CBM and VBM) in units of eV) with reference to graphene's Fermi level.

Structures	BeO	ZnO	CdO	HgO	BN
CBM	3.24	1.49	0.76	-0.96	3.83
VBM	-3.58	-1.81	-1.31	-1.15	-2.27

BeO, ZnO, CdO, and HgO as well as for BN with reference to graphene's Fermi level. The calculations are performed with the HSE06 functional. For HgO, both the CBM and VBM are lower than the Fermi level of graphene, indicating an electron transfer from graphene to HgO in the graphene/HgO heterostructure.

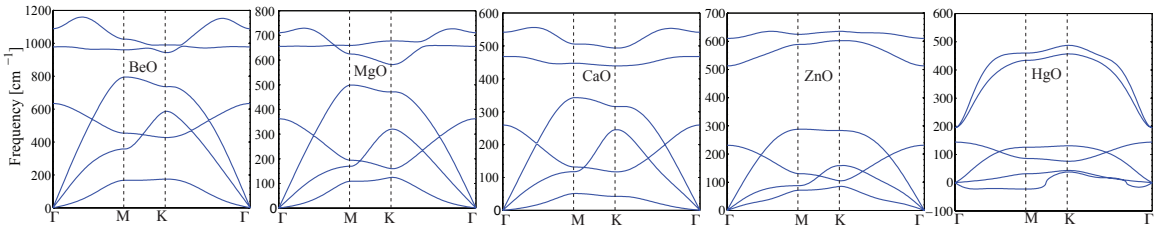

Figure A.2: Phonon spectra of single-layer BeO, MgO, CaO, ZnO, and HgO.

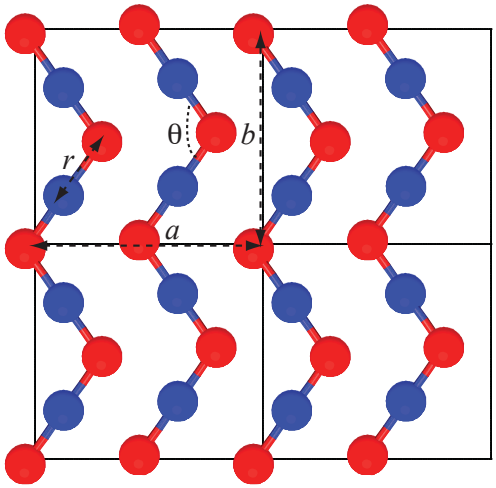

Figure A.3: Reconstructed structure of single-layer HgO. The structure has space group *Pbam* (55) with 8 atoms in the unit cell, and the structural parameters are a = 7.02 Å, b = 6.62 Å, r = 2.03 Å and θ = 109.2°.

APPENDIX B

APPENDIX OF CHAPTER 6

Method of calculating band gap center energy. Figure B.1 shows the average electrostatic potential for single-layer GaSe along the direction perpendicular to the layer calculated using the HSE06 functional. Shifting the energy scale, such that the vacuum level is set to zero, determines the alignment of the CBM and VBM energy levels for different materials. The band gap center energy is given by the average of E_{CBM} and E_{VBM}.

Band alignments of single-layer MX with reference to water's redox potential. Figure B.2 shows the band alignments of single-layer MX and MoS_2 with reference to water's redox potential calculated using the G_0W_0 approximation to obtain the band gaps. Similar to the HSE06 results shown in Figure 6.5 in Chapter 5, the results of band alignments using the G_0W_0 band gaps suggest that single-layer MX and MoS_2 are potential photocatalysts for water splitting.

Strain effects on the band structure of single-layer GaSe. Figure B.3 shows the band structures of single-layer GaSe at the strains of −4% and +4%. As can be seen, at the strain of −4%, the conduction band maximum (CBM) occurs at the K point. At the strain of +4%, the CBM switches to the Γ point. The change of band edge positions leads to the discontinuities of the curves shown in Figure 6.7 in Chapter 5.

Enthalpy of solvation. When a solid ionic compound AB(s) dissolves in water, the following solvation reaction establishes the equilibrium concentrations of the dissolved ions

$$\mathrm{AB(s)} \rightleftharpoons \mathrm{A^+(aq) + B^-(aq)}. \tag{B.1}$$

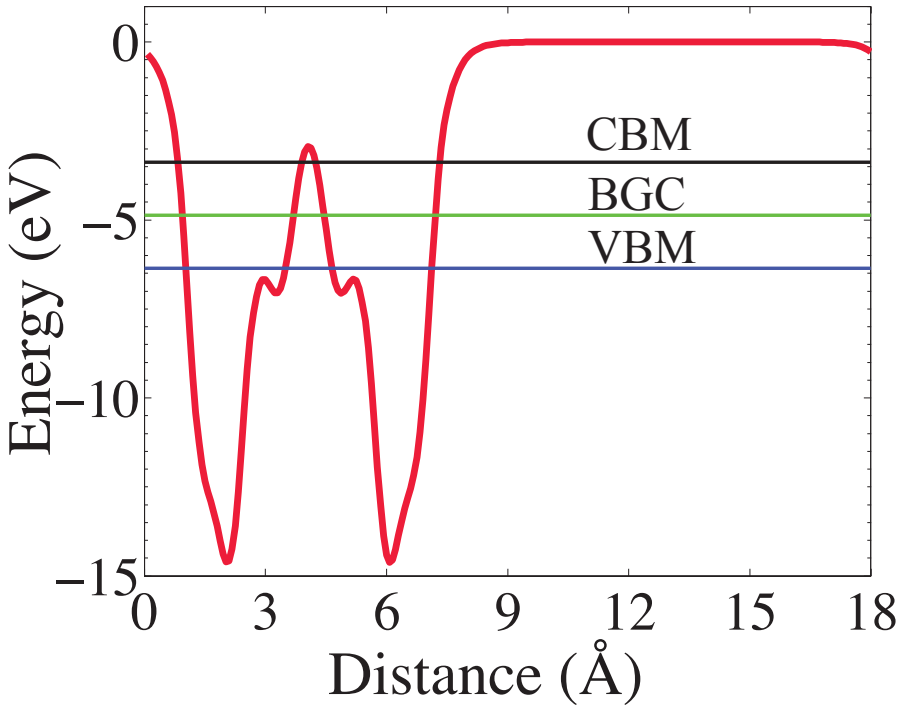

Figure B.1: Average electrostatic potential (red curve) of single-layer GaSe along the direction perpendicular to the layer calculated with the HSE06 functional. The vacuum energy level is set to zero. The conduction band minimum and valence band maximum (CBM and VBM) are shown, along with the band gap center (BGC) energy. All these three energy levels are with reference to the vacuum level.

Here, $A^+(aq)$ and $B^-(aq)$ represent A and B ions in an aqueous solution, respectively. The solubility product K_{sp} of the solvation reaction is given by the Gibbs energy of solvation ΔG_{solv}. In our following analysis, we assume that the entropy of solvation is similar for the various monochalcogenide systems and several other reference systems. To calculate the enthalpy of hydration, ΔH_{solv}, we decompose the reaction (B.1) into two steps. First, the solid compound is separated into isolated gas atoms, i.e.

$$AB(s) \rightleftharpoons A(g) + B(g), \tag{B.2}$$

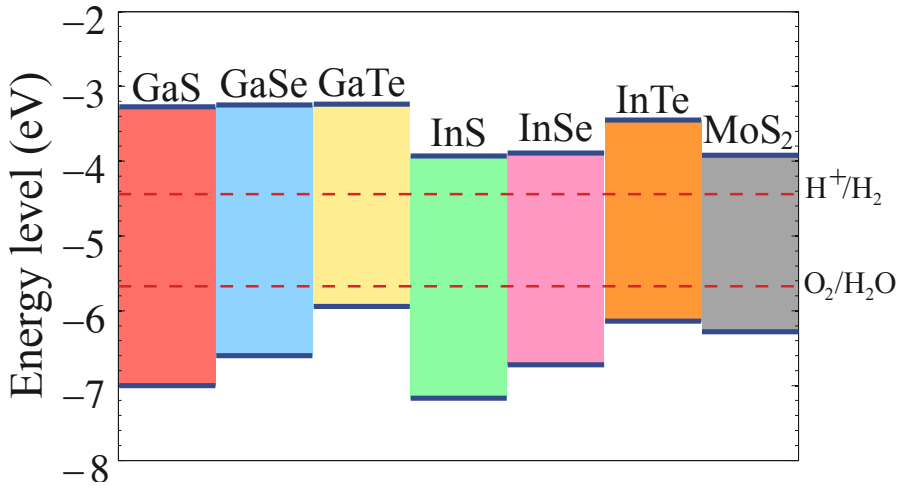

Figure B.2: Band alignments of single-layer MX and MoS_2 with reference to water's redox potential calculated using the G_0W_0 approximation.

where A(g) and B(g) are isolated A and B atoms in gas state. The enthalpy change of reaction (B.2), i.e. the cohesive energy of the AB compounds, ΔE_{coh}, is calculated using the PBE functional as implemented in VASP code. In the second reaction shown below, the gas atoms are ionized and subsequently solvated in water,

$$\text{A(g)} + \text{B(g)} \rightarrow \text{A}^+\text{(aq)} + \text{B}^-\text{(aq)}. \tag{B.3}$$

To calculate the enthalpy ΔH_{hyd} of this reaction, we calculate the energy of the isolated atoms and of the hydrated ions using Gaussian09 [158, 60]. The aug-cc-pVQZ basis sets are used for all calculations and for the heavy atoms Cd, In, and Te we use effective core potentials [156, 157]. The energy of the solvated ions is calculated using several explicit water molecules and the SMD solvation model for the solute-solvent interactions [158]. We find that two water molecules are required to converge the hydration energy ΔH_{hyd} to 5 kJ/mol. Ions in solution can lower their energy by forming pairs [163].These ion associations are more likely to occur for larger cations and ions with multiple charges. We estimate

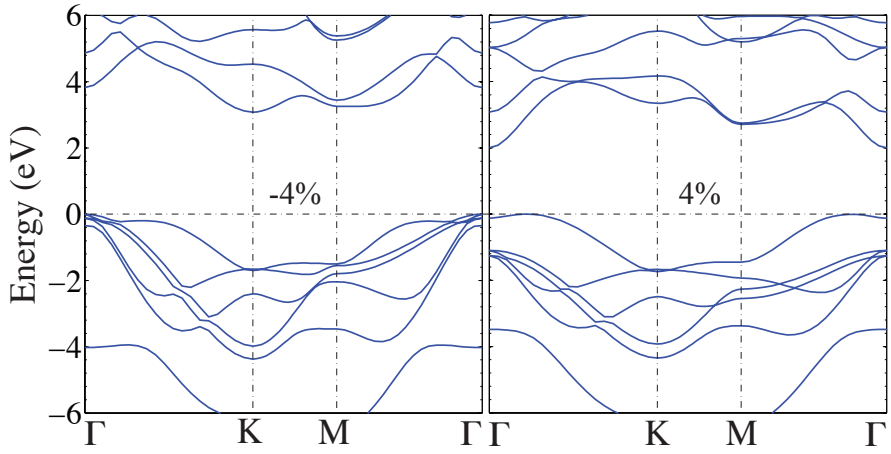

Figure B.3: Band structures of single-layer GaSe at the strains of −4% and +4%.

the energy of associated ions by calculating the energies of cation/anion pairs solvated using the SMD model. The enthalpy of solvation is given by the sum of the cohesive energy ΔE_{coh} and the enthalpy of hydration ΔH_{hyd}.

APPENDIX C

APPENDIX OF CHAPTER 8

Using single-layer SnS_2 as an example, this appendix describes the four steps of calculations used to solve the Bethe-Salpeter Equation (BSE) as implemented in VASP. The main output of these calculations is the optical spectrum shown in Fig. 8.5.

Within all the four steps, three common files including **KPOINTS**, **POSCAR**, and **POTCAR** are used. The input tags in these three files are shown below:

KPOINTS

SnS_2

0

Gamma

18 18 1

POSCAR

SnS2

1.00000000000000

3.2011845345179681 -1.8482047527296159 0.0000000000000000

0.0000000000000000 3.6964095054592310 0.0000000000000000

0.0000000000000000 0.0000000000000000 18.0000000000000000

S Sn

2 1

Direct

0.6666666666666643 0.3333333333333357 0.9178119550298831

0.3333333333333357 0.6666666666666643 0.0821880449701169

0.0000000000000000 0.0000000000000000 0.0000000000000000

POTCAR

The S_GW and Sn_d_GW pseudopotential files are used in the calculations

However, the **INCAR** files are slightly different in each step. Step 1 is a standard self-consistent DFT calculation using the PBE functional. The corresponding **INCAR** file contains the following tags:

INCAR

ENCUT = 400

PREC = ACCURATE

IBRION = -1

EDIFF = 1.0E-6

ISMEAR = 0

SIGMA = 0.05

NPAR = 4

Step 2 aims to obtain wavefunction derivatives by the density functional perturbation theory. The corresponding **INCAR** file is as follows:

INCAR

ENCUT = 400

PREC = ACCURATE

NBANDS = 192

IBRION = -1

ISMEAR = 0

SIGMA = 0.05

NEDOS = 2000

ALGO = Exact

LOPTICS = .TRUE.

Step 2 contains a new parameter **NBANDS**. A G_0W_0 calculation requires a large amount of vacant bands. Although there is no direct convergence criterion of selecting **NBANDS**, a general rule is to push the computer limit, i.e. using as many vacant bands as possible. Note that step 2 is a time-consuming process, as the eigenvalue problem is solved exactly.

Step 3 provides quasiparticle energies through a G_0W_0 calculation. The **INCAR** file is shown below:

INCAR

ENCUT = 400

PREC = ACCURATE

NBANDS = 192

IBRION = -1

ISMEAR = 0

SIGMA = 0.05

ALGO = GW0

ENCUTGW = 200

NOMEGA = 128

The key parameters in Step 3 are **ENCUTGW** and **NOMEGA**. The former parameter specifies the energy cutoff for response function while the latter one specifies the number of frequency grid points. These parameters have been checked so that the quasiparticle bandgap is within an accuracy of five meV as opposed to the one using smaller values.

Step 4 is the last step of solving the BSE. After this step, the information of the dielectric constant can be found in the output file named vasp.xml. The **INCAR** file for this step reads as:

INCAR

ENCUT = 400

PREC = ACCURATE

NBANDS = 192

IBRION = -1

ISMEAR = 0

SIGMA = 0.05

CSHIFT = 0.05

ENCUTGW = 200

NOMEGA = 128

ALGO = BSE

LBSE = .TRUE.

NBANDSO = 12

NBANDSV = 16

NEDOS = 3000

Three important parameters are involved Step 4. They are **NBANDSO**, **NBANDSV**, and **CSHIFT**, respectively. **NBANDSO** and **NBANDSV** represent the number of occupied and unoccupied bands considered for solving the BSE. The criterion of choosing **NBANDSO** and **NBANDSV** is that the optical absorption peak positions must be almost identical to the peak obtained from using different values of these two parameters. **CSHIFT** is a broadening parameter normally ranging from 0.025 to 0.1 eV. Smaller values of **CSHIFT** will make the absorption peak position sharper. Larger ones will broaden the absorption peak. However, the peak positions are not affected by the settings of **CSHIFT**.

APPENDIX D

APPENDIX OF CHAPTER 9

K-meshes. K-meshes used for optimizing the $\sqrt{3}a \times a$, $2a \times 2a$, $\sqrt{3}a \times \sqrt{3}a$, and $2H$ and $1T'$ heterostructure are $32 \times 48 \times 1$, $24 \times 24 \times 1$, $32 \times 32 \times 1$, and $1 \times 18 \times 1$, respectively. The k-meshes for the calculations of the density of states for the four structures are $32 \times 48 \times 9$, $24 \times 24 \times 9$, $32 \times 32 \times 9$, and $4 \times 36 \times 1$, respectively.

Band structure of 2H MoS_2. Figure D.1a shows the band structure of $2H$ single-layer MoS_2. As can be seen, $2H$ MoS_2 presents a PBE bandgap of 1.67 eV, consistent with previous calculations and a slight underestimation of the experimental optical bandgap of 1.90 eV [160, 86]. Including the spin-orbit coupling results in the band structure shown in Figure D.1b. We observe that the splitting magnitude of the valence band maximum at the K point is 0.149 eV, agreeing well with a reported value of 0.146 eV [194].

Density of states of 1T MoS_2. Figure D.2 shows the total and projected density of states of single-layer $1T$ MoS_2. Clearly, the total density of states (TDOS) of single-layer $1T$ MoS_2 is dominated by the Mo $3d$ and S $4p$ states.

Phonon spectrum of 2H MoS_2. Figure D.3 shows the phonon spectrum of $2H$ single-layer MoS_2. No imaginary frequencies are observed, confirming the dynamical stability of $2H$ MoS_2.

Density of states of single-layer MoS_2 with various CDW structures. Consistent with the band structures shown in the text, the density of states shown in Fig.D.4 confirms that the $\sqrt{3}a \times a$ structure has a Dirac cone, while the $2a \times 2a$ and $\sqrt{3}a \times \sqrt{3}a$ structures are semiconductors.

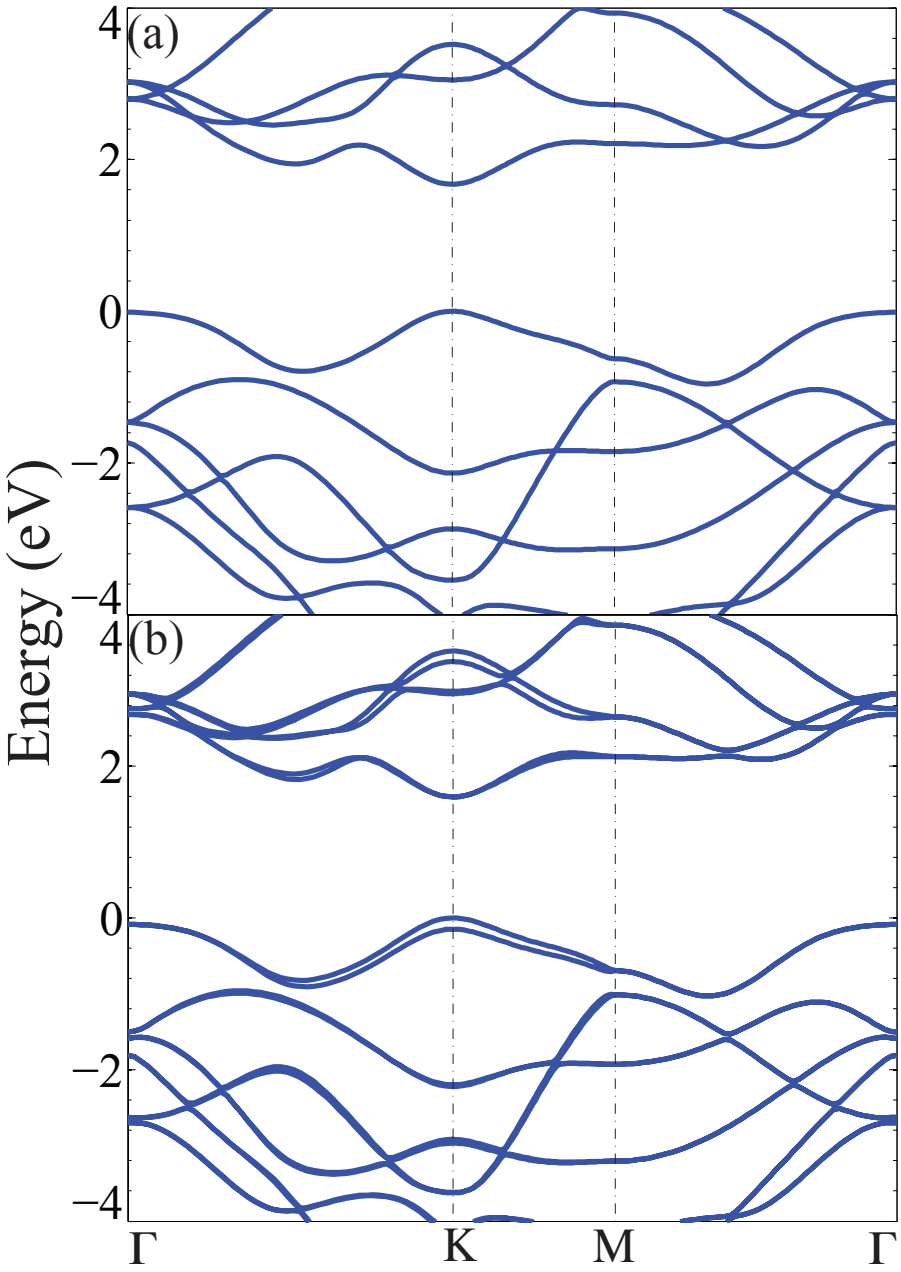

Figure D.1: Band structures of single-layer MoS_2 with the 2*H* structure calculated (a) with and (b) without the spin-orbit coupling.

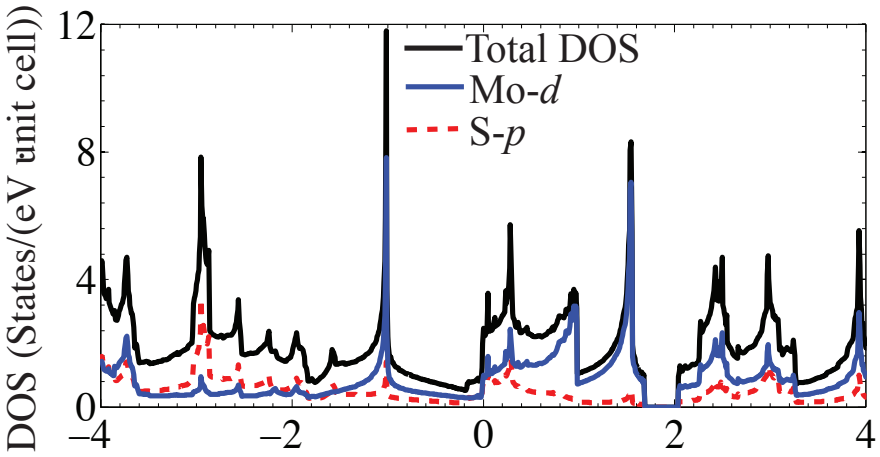

Figure D.2: Density of states of single-layer MoS_2 with the 1*T* structure.

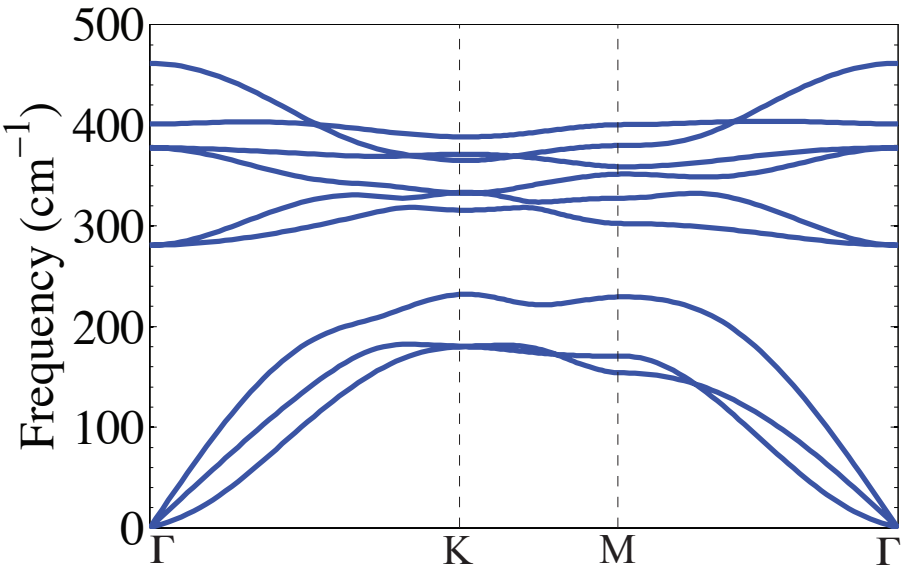

Figure D.3: Phonon spectrum of single-layer MoS_2 with the 2*H* structure.

The imaginary part of the electric susceptibility. The nesting function, which is the imaginary part of the electric susceptibility at ω=0, $\chi''(\mathbf{q})$, is calculated according to the following equation [196],

$$\lim_{\omega\to 0}\chi''(\mathbf{q},\omega)/\omega = \sum_{\mathbf{k}} \delta(\varepsilon_{\mathbf{k}} - \varepsilon_F)\delta(\varepsilon_{\mathbf{k}+\mathbf{q}} - \varepsilon_F), \tag{D.1}$$

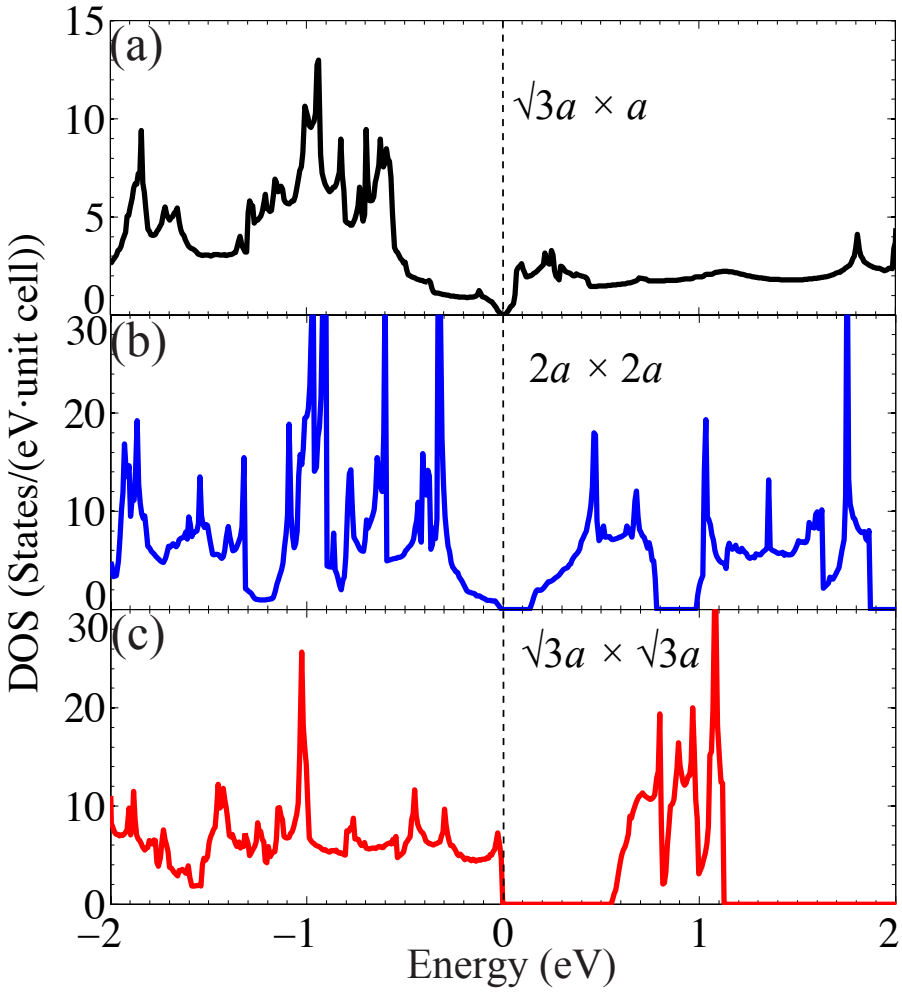

Figure D.4: Total density of states of single-layer MoS_2 with different reconstructed structures.

where ε_F is the Fermi energy. A $100 \times 100 \times 1$ k-mesh is used to calculate both the real and imaginary parts of susceptibility, resulting in 10000 k points in the primitive cell of the reciprocal lattice.

2H/1T′ heterostructure. Figure D.6 illustrates the interface structure after the geometry optimizations with a force tolerance of 0.025 eV/Å. Similar to the definition of grain boundary energy of single-layer MoS_2 [198], we define the

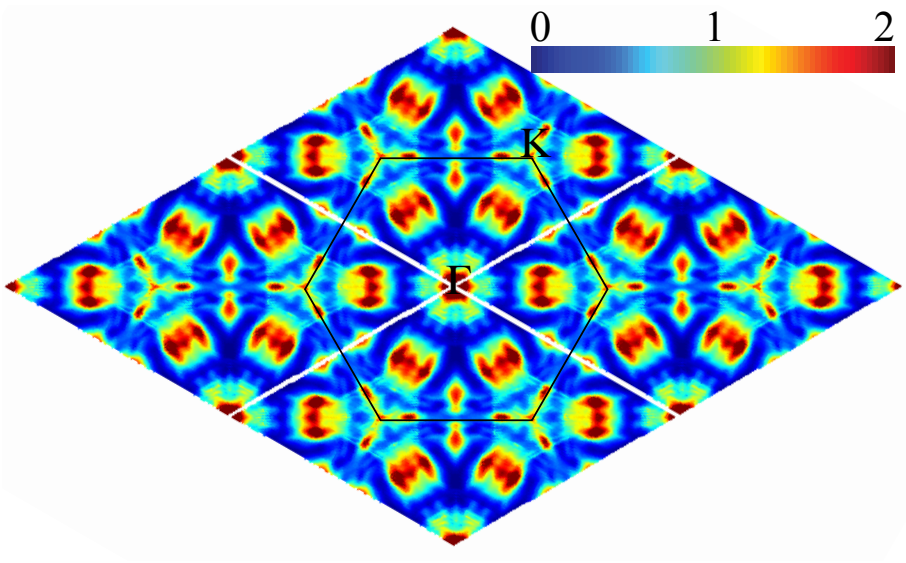

Figure D.5: The imaginary part of susceptibility of $1T$ single-layer MoS_2.

interface energy E_{int} as,

$$E_{int} = \frac{E_{2H/1T'} - 1/2(E_{2H} + E_{1T'})}{2l_0}, \tag{D.2}$$

where $E_{2H/1T'}$, E_{2H}, and $E_{1T'}$ are the total energies of the heterostructure, the $2H$ structure, and the $1T'$ structure, respectively. l_0 is the interface length in the simulation supercell. All energies are calculated with 18 rectangular cells, two of which are illustrated in Fig. D.6.

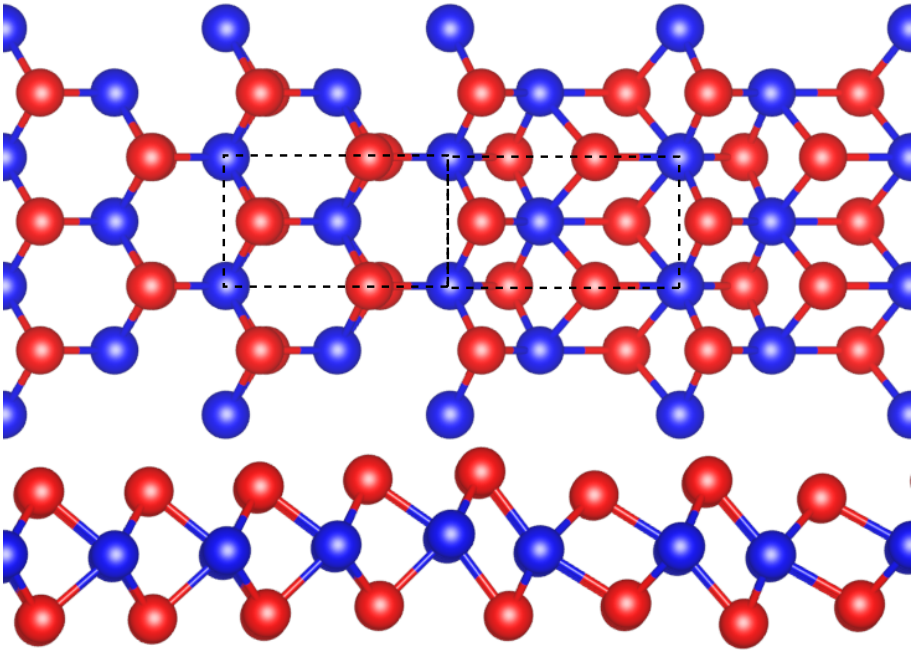

Figure D.6: Top view and side view of the $2H/1T'$ heterostructure after geometry optimizations. Rectangular cells of $2H$ and $1T'$ structures are illustrated by enclosed dashed lines.

BIBLIOGRAPHY

[1] H. Zhong, G. Yang, H. Song, Q. Liao, H. Cui, P. Shen, and C.-X. Wang. Vertically aligned graphene-like SnS_2 ultrathin nanosheet arrays: excellent energy storage, catalysis, photoconduction, and field-emitting performances. *J. Phys. Chem. C*, 116(16):9319–9326, 2012.

[2] H. L. Zhuang and R. G. Hennig. Single-layer group-III monochalcogenide photocatalysts for water splitting. *Chem. Mater.*, 25(15):3232–3238, 2013.

[3] B. Radisavljevic, A. Radenovic, J. Brivio, V. Giacometti, and A. Kis. Single-layer MoS_2 transistors. *Nature Nanotech.*, 6(3):147–150, 2011.

[4] Y. Wang, Z. Shi, Y. Huang, Y. Ma, C. Wang, M. Chen, and Y. Chen. Supercapacitor devices based on graphene materials. *J Phys. Chem. C*, 113(30):13103–13107, 2009.

[5] W. S. Yun, S. W. Han, S. C. Hong, I. G. Kim, and J. D. Lee. Thickness and strain effects on electronic structures of transition metal dichalcogenides: 2H-MX_2 semiconductors (M = Mo, W; X = S, Se, Te). *Phys. Rev. B*, 85(3):033305, 2012.

[6] P. Yang and J.-M. Tarascon. Towards systems materials engineering. *Nature Mater.*, 11(7):560–563, 2012.

[7] M. Xu, T. Liang, M. Shi, and H. Chen. Graphene-like two-dimensional materials. *Chem. Rev.*, 113(5):3766–3798, 2013.

[8] S. Z. Butler, S. M. Hollen, L. Cao, Y. Cui, J. A. Gupta, H. R. Gutiérrez, T. F. Heinz, S. S. Hong, J. Huang, A. F. Ismach, E. Johnston-Halperin, M. Kuno, V. V. Plashnitsa, R. D. Robinson, R. S. Ruoff, S. Salahuddin, J. Shan, L. Shi, M. G. Spencer, M. Terrones, W. Windl, and J. E. Goldberger. Progress, challenges, and opportunities in two-dimensional materials beyond graphene. *ACS Nano*, 7(4):2898–2926, 2013.

[9] R. Mas-Balleste, C. Gomez-Navarro, J. Gomez-Herrero, and F. Zamora. 2D materials: to graphene and beyond. *Nanoscale*, 3(1):20–30, 2011.

[10] Y. Sun, Q. Wu, and G. Shi. Graphene based new energy materials. *Energy Environ. Sci.*, 4(4):1113–1132, 2011.

[11] J. Liu, Y. Xue, M. Zhang, and L. Dai. Graphene-based materials for energy applications. *MRS Bulletin*, 37(12):1265–1272, 12 2012.

[12] H. S. Shin, G. Eda, L.-J. Li, K. P. Loh, and H. Zhang. The chemistry of two-dimensional layered transition metal dichalcogenide nanosheets. *Nature Chem.*, 5(4):263–275, 2013.

[13] K. S. Novoselov, A. K. Geim, S. V. Morozov, D. Jiang, Y. Zhang, S. V. Dubonos, I. V. Grigorieva, and A. A. Firsov. Electric field effect in atomically thin carbon films. *Science*, 306(5696):666–669, 2004.

[14] N. Alem, R. Erni, C. Kisielowski, M. D. Rossell, W. Gannett, and A. Zettl. Atomically thin hexagonal boron nitride probed by ultrahigh-resolution transmission electron microscopy. *Phys. Rev. B*, 80(15):155425, 2009.

[15] C. Tusche, H. L. Meyerheim, and J. Kirschner. Observation of depolarized ZnO(0001) monolayers: Formation of unreconstructed planar sheets. *Phys. Rev. Lett.*, 99(2):026102, 2007.

[16] P. Vogt, P. De Padova, C. Quaresima, J. Avila, E. Frantzeskakis, M. C. Asensio, A. Resta, B. Ealet, and G. Le Lay. Silicene: compelling experimental evidence for graphenelike two-dimensional silicon. *Phys. Rev. Lett.*, 108(15):155501, 2012.

[17] Y. Sun, Z. Sun, S. Gao, H. Cheng, Q. Liu, F. Lei, S. Wei, and Y. Xie. All-surface-atomic-metal chalcogenide sheets for high-efficiency visible-light photoelectrochemical water splitting. *Adv. Energy Mater.*, 2013.

[18] S. Tan, Y. Zhang, M. Xia, Z. Ye, F. Chen, X. Xie, R. Peng, D. Xu, Q. Fan, H. Xu, et al. Interface-induced superconductivity and strain-dependent spin density waves in FeSe/$SrTiO_3$ thin films. *Nature Mater.*, 12(7):634–640, 2013.

[19] H. L. Zhuang, A. K. Singh, and R. G. Hennig. Computational discovery of single-layer III-V materials. *Phys. Rev. B*, 87(16):165415, 2013.

[20] A. K. Singh and R. G. Hennig. Scaling relation for thermal ripples in single and multilayer graphene. *Phys. Rev. B*, 87(9):094112, 2013.

[21] J. C. Meyer, A. K. Geim, M. I. Katsnelson, K. S. Novoselov, T. J. Booth, and S. Roth. The structure of suspended graphene sheets. *Nature*, 446(7131), 2007.

[22] A. Fasolino, J. H. Los, and M. I. Katsnelson. Intrinsic ripples in graphene. *Nature Mater.*, 6(11):858–861, 2007.

[23] J. Brivio, D. T. L. Alexander, and A. Kis. Ripples and layers in ultrathin MoS_2 membranes. *Nano Letter.*, 11(12):5148–5153, 2011.

[24] P. Y. Huang, C. S. Ruiz-Vargas, A. M van der Zande, W. S. Whitney, M. P. Levendorf, J. W. Kevek, S. Garg, J. S. Alden, C. J. Hustedt, Y. Zhu, et al. Grains and grain boundaries in single-layer graphene atomic patchwork quilts. *Nature*, 469(7330):389–392, 2011.

[25] A. M. van der Zande, P. Y. Huang, D. A. Chenet, T. C. Berkelbach, Y. M. You, G.-H. Lee, T. F. Heinz, D. R. Reichman, D. A. Muller, and J. C. Hone. Grains and grain boundaries in highly crystalline monolayer molybdenum disulphide. *Nature Mater.*, 12(6):554–561, 2013.

[26] H. Liu, Y. Liu, and D. Zhu. Chemical doping of graphene. *J. Mater. Chem.*, 21(10):3335–3345, 2011.

[27] O. V. Yazyev and S. G. Louie. Topological defects in graphene: Dislocations and grain boundaries. *Phys. Rev. B*, 81(19):195420, 2010.

[28] J. H. Warner, E. R. Margine, M. Mukai, A. W. Robertson, F. Giustino, and A. I. Kirkland. Dislocation-driven deformations in graphene. *Science*, 337(6091):209–212, 2012.

[29] C. S. Ruiz-Vargas, H. L. Zhuang, P. Y. Huang, A. M. van der Zande, S. Garg, P. L. McEuen, D. A. Muller, R. G. Hennig, and J. Park. Softened elastic response and unzipping in chemical vapor deposition graphene membranes. *Nano Letter.*, 11(6):2259–2263, 2011.

[30] C. Lee, X. Wei, J. W. Kysar, and J. Hone. Measurement of the elastic properties and intrinsic strength of monolayer graphene. *Science*, 321(5887):385–388, 2008.

[31] A. H. Castro Neto, F. Guinea, N. M. R. Peres, K. S. Novoselov, and A. K. Geim. The electronic properties of graphene. *Rev. Mod. Phys.*, 81(1):109–162, 2009.

[32] Q. H. Wang, K.-Z. Kourosh, A. Andras, J. N. Coleman, and M. S. Strano. Electronics and optoelectronics of two-dimensional transition metal dichalcogenides. *Nature Nanotech.*, 7(11):699–712, 2012.

[33] L. Britnell, R. M. Ribeiro, A. Eckmann, R. Jalil, B. D. Belle, A. Mishchenko, Y.-J. Kim, R. V. Gorbachev, T. Georgiou, S. V. Morozov, A. N. Grigorenko, A. K. Geim, C. Casiraghi, A. H. Castro Neto, and K. S. Novoselov. Strong light-matter interactions in heterostructures of atomically thin films. *Science*, 340(6138):1311–1314, 2013.

[34] A. A. Balandin, S. Ghosh, W. Bao, I. Calizo, D. Teweldebrhan, F. Miao, and C. N. Lau. Superior thermal conductivity of single-layer graphene. *Nano Letter.*, 8(3):902–907, 2008.

[35] Karel-Alexander N. Duerloo, Mitchell T. Ong, and Evan J. Reed. Intrinsic piezoelectricity in two-dimensional materials. *J. Phys. Chem. Lett.*, 3(19):2871–2876, 2012.

[36] H. L. Zhuang and R. G. Hennig. Theoretical perspective of photocatalytic properties of single-layer SnS_2. *Phys. Rev. B*, 88(11):115314, 2013.

[37] F. Bonaccorso, A. Lombardo, T. Hasan, Z. Sun, L. Colombo, and A. C. Ferrari. Production and processing of graphene and 2D crystals. *Mater. Today*, 15(12):564–589, 2012.

[38] K. S. Novoselov, D. Jiang, F. Schedin, T. J. Booth, V. V. Khotkevich, S. V. Morozov, and A. K. Geim. Two-dimensional atomic crystals. *Proc. Nat. Acad. Sci.*, 102(30):10451–10453, 2005.

[39] A. W. Tsen, L. Brown, R. W. Havener, and J. Park. Polycrystallinity and stacking in CVD graphene. *Acc. Chem. Res.*, 46(10):2286–2296, 2013.

[40] V. Nicolosi, M. Chhowalla, M. G. Kanatzidis, M. S. Strano, and J. N. Coleman. Liquid exfoliation of layered materials. *Science*, 340(6139), 2013.

[41] H. Li, G. Lu, Y. Wang, Z. Yin, C. Cong, Q. He, L. Wang, F. Ding, T. Yu, and H. Zhang. Mechanical exfoliation and characterization of single- and few-layer nanosheets of WSe_2, TaS_2, and $TaSe_2$. *Small*, 9(11):1974–1981, 2013.

[42] Y. Sun, H. Cheng, S. Gao, Q. Liu, Z. Sun, C. Xiao, C. Wu, S. Wei, and Y. Xie. Atomically thick bismuth selenide freestanding single layers achieving enhanced thermoelectric energy harvesting. *J. Am. Chem. Soc.*, 134(50):20294–20297, 2012.

[43] J. Park, W. C. Mitchel, L. Grazulis, H. E. Smith, K. G. Eyink, J. J. Boeckl,

D. H. Tomich, S. D. Pacley, and J. E. Hoelscher. Epitaxial graphene growth by carbon molecular beam epitaxy (CMBE). *Adv. Mater.*, 22(37):4140–4145, 2010.

[44] L. Britnell, R. V. Gorbachev, R. Jalil, B. D. Belle, F. Schedin, A. Mishchenko, T. Georgiou, M. I. Katsnelson, L. Eaves, S. V. Morozov, N. M. R. Peres, J. Leist, A. K. Geim, K. S. Novoselov, and L. A. Ponomarenko. Field-effect tunneling transistor based on vertical graphene heterostructures. *Science*, 335(6071):947–950, 2012.

[45] Y. F. Sun, H. Cheng, S. Gao, Z. Sun, Q. Liu, Q. Liu, F. Lei, T. Yao, J. He, S. Wei, and Y. Xie. Freestanding tin disulfide single-layers realizing efficient visible-light water splitting. *Angew. Chem. Int. Edit.*, 51(35):8727–8731, 2012.

[46] M. S. Fuhrer and J. Hone. Measurement of mobility in dual-gated MoS_2 transistors. *Nature Nanotech.*, 8(3):146–147, 2013.

[47] S. Bertolazzi, J. Brivio, and A. Kis. Stretching and breaking of ultrathin MoS_2. *ACS Nano*, 5(12):9703–9709, 2011.

[48] M. Winter and R. J. Brodd. What are batteries, fuel cells, and supercapacitors? *Chem. Rev.*, 104(10):4245–4270, 2004.

[49] S. Lebègue, T. Björkman, M. Klintenberg, R. M. Nieminen, and O. Eriksson. Two-dimensional materials from data filtering and *ab initio* calculations. *Phys. Rev. X*, 3(3):031002, 2013.

[50] C. Ataca, H. Sahin, and S. Ciraci. Stable, single-layer MX_2 transition-metal oxides and dichalcogenides in a honeycomb-like structure. *J. Phys. Chem. C*, 116(16):8983–8999, 2012.

[51] H. Sahin, S. Cahangirov, M. Topsakal, E. Bekaroglu, E. Akturk, R. Senger, and S. Ciraci. Monolayer honeycomb structures of group-IV elements and III-V binary compounds: first-principles calculations. *Phys. Rev. B*, 80(15):155453, 2009.

[52] S. Cahangirov, M. Topsakal, E. Aktürk, H. Şahin, and S. Ciraci. Two- and one-dimensional honeycomb structures of silicon and germanium. *Phys. Rev. Lett.*, 102(23):236804, 2009.

[53] H. L. Zhuang, M. D. Johannes, M. N. Blonsky, and R. G. Hennig. Compu-

tational prediction and characterization of single-layer CrS_2. *submitted to Appl. Phys. Lett.*, 2013.

[54] H. L. Zhuang and R. G. Hennig. Computational identification of single-layer CdO for electronic and optical applications. *Appl. Phys. Lett.*, 103(21):212102, 2013.

[55] H. L. Zhuang and R. G. Hennig. Electronic structures of single-layer boron pnictides. *Appl. Phys. Lett.*, 101(15):153109, 2012.

[56] H. L. Zhuang and R. G. Hennig. Computational search for single-layer transition-metal dichalcogenide photocatalysts. *J. Phys. Chem. C*, 117(40):20440–20445, 2013.

[57] S. Baroni, S. de Gironcoli, A. Dal Corso, and P. Giannozzi. Phonons and related crystal properties from density-functional perturbation theory. *Rev. Mod. Phys.*, 73(2):515–562, 2001.

[58] P. Giannozzi, S. Baroni, N. Bonini, M. Calandra, R. Car, C. Cavazzoni, D. Ceresoli, G. L. Chiarotti, M. Cococcioni, I. Dabo, A. Dal Corso, S. de Gironcoli, S. Fabris, G. Fratesi, R. Gebauer, U. Gerstmann, C. Gougoussis, A. Kokalj, M. Lazzeri, L. Martin-Samos, N. Marzari, F. Mauri, R. Mazzarello, S. Paolini, A. Pasquarello, L. Paulatto, C. Sbraccia, S. Scandolo, G. Sclauzero, A. P. Seitsonen, A. Smogunov, P. Umari, and R. M. Wentzcovitch. QUANTUM ESPRESSO: a modular and open-source software project for quantum simulations of materials. *J. Phys.: Cond. Matt.*, 21(39):395502, 2009.

[59] G. Kresse and J. Furthmüller. Efficient iterative schemes for *ab initio* total-energy calculations using a plane-wave basis set. *Phys. Rev. B*, 54(16):11169–11186, 1996.

[60] M. J. Frisch, G. W. Trucks, H. B. Schlegel, G. E. Scuseria, M. A. Robb, J. R. Cheeseman, G. Scalmani, V. Barone, B. Mennucci, G. A. Petersson, H. Nakatsuji, M. Caricato, X. Li, H. P. Hratchian, A. F. Izmaylov, J. Bloino, G. Zheng, J. L. Sonnenberg, M. Hada, M. Ehara, K. Toyota, R. Fukuda, J. Hasegawa, M. Ishida, T. Nakajima, Y. Honda, O. Kitao, H. Nakai, T. Vreven, J. A. Montgomery, Jr., J. E. Peralta, F. Ogliaro, M. Bearpark, J. J. Heyd, E. Brothers, K. N. Kudin, V. N. Staroverov, R. Kobayashi, J. Normand, K. Raghavachari, A. Rendell, J. C. Burant, S. S. Iyengar, J. Tomasi, M. Cossi, N. Rega, J. M. Millam, M. Klene, J. E. Knox, J. B. Cross, V. Bakken, C. Adamo, J. Jaramillo, R. Gomperts, R. E. Stratmann,

O. Yazyev, A. J. Austin, R. Cammi, C. Pomelli, J. W. Ochterski, R. L. Martin, K. Morokuma, V. G. Zakrzewski, G. A. Voth, P. Salvador, J. J. Dannenberg, S. Dapprich, A. D. Daniels, . Farkas, J. B. Foresman, J. V. Ortiz, J. Cioslowski, and D. J. Fox. Gaussian 09 Revision A.1. Gaussian Inc. Wallingford CT 2009.

[61] J. P. Perdew, K. Burke, and M. Ernzerhof. Generalized gradient approximation made simple. *Phys. Rev. Lett.*, 77(18):3865–3868, 1996.

[62] J. P. Perdew, R. G. Parr, M. Levy, and J. L. Balduz. Density-functional theory for fractional particle number: Derivative discontinuities of the energy. *Phys. Rev. Lett.*, 49(23):1691–1694, 1982.

[63] J. Heyd, G. E. Scuseria, and M. Ernzerhof. Hybrid functionals based on a screened Coulomb potential. *J. Chem. Phys.*, 118(18):8207, 2003.

[64] G. Onida, L. Reining, and A. Rubio. Electronic excitations: density-functional versus many-body Green's-function approaches. *Rev. Mod. Phys.*, 74(2):601–659, 2002.

[65] C. Rödl and F. Bechstedt. Optical and energy-loss spectra of the antiferromagnetic transition metal oxides MnO, FeO, CoO, and NiO including quasiparticle and excitonic effects. *Phys. Rev. B*, 86(23):235122, 2012.

[66] P. Rinke, A. Schleife, E. Kioupakis, A. Janotti, C. Rödl, F. Bechstedt, M. Scheffler, and C. G. Van de Walle. First-principles optical spectra for f centers in MgO. *Phys. Rev. Lett.*, 108(12):126404, 2012.

[67] J. Hwang, M. Kim, D. Campbell, H. A. Alsalman, J. Y. Kwak, S. Shivaraman, A. R. Woll, A. K. Singh, R. G. Hennig, S. Gorantla, M. H. Rümmeli, and Michael G. Spencer. van der waals epitaxial growth of graphene on sapphire by chemical vapor deposition without a metal catalyst. *ACS Nano*, 7(1):385–395, 2013.

[68] Y. Yoon, K. Ganapathi, and S. Salahuddin. How good can monolayer MoS_2 transistors be? *Nano Letter.*, 11(9):3768–3773, 2011.

[69] F. Ortmann, F. Bechstedt, and K. Hannewald. Charge transport in organic crystals: theory and modelling. *physica status solidi (b)*, 248(3):511–525, 2011.

[70] B. Radisavljevic and A. Kis. Mobility engineering and a metal-insulator transition in monolayer MoS_2. *Nature Mater.*, 12(9):815–820, 2013.

[71] D. Malko, C. Neiss, F. Viñes, and A. Görling. Competition for graphene: graphynes with direction-dependent Dirac cones. *Phys. Rev. Lett.*, 108(8):086804, 2012.

[72] Y. Zhang, Y.-W. Tan, H. L. Stormer, and P. Kim. Experimental observation of the quantum Hall effect and Berry's phase in graphene. *Nature*, 438(7065):201–204, 2005.

[73] F. Schwierz. Graphene transistors. *Nature Nanotech.*, 5(7):487–496, 2010.

[74] R. Balog, B. Jørgensen, L. Nilsson, M. Andersen, E. Rienks, M. Bianchi, M. Fanetti, E. Lgsgaard, A. Baraldi, S. Lizzit, Z. Sljivancanin, F. Besenbacher, B. Hammer, T. G. Pedersen, P. Hofmann, and L. Hornekr. Bandgap opening in graphene induced by patterned hydrogen adsorption. *Nature Mater.*, 9(4):315–319, 2010.

[75] K. J. Jeon, Z. Lee, E. Pollak, L. Moreschini, A. Bostwick, C. M. Park, R. Mendelsberg, V. Radmilovic, R. Kostecki, T. J. Richardson, and E. Rotenberg. Fluorographene: a wide bandgap semiconductor with ultraviolet luminescence. *ACS Nano*, 5(2):1042–1046, 2011.

[76] M. Y. Han, B. Özyilmaz, Y. Zhang, and P. Kim. Energy band-gap engineering of graphene nanoribbons. *Phys. Rev. Lett.*, 98(20):206805, 2007.

[77] P. E. Blöchl. Projector augmented-wave method. *Phys. Rev. B*, 50(24):17953–17979, 1994.

[78] G. Kresse and D. Joubert. From ultrasoft pseudopotentials to the projector augmented-wave method. *Phys. Rev. B*, 59(3):1758–1775, 1999.

[79] J. P. Perdew and A. Zunger. Self-interaction correction to density-functional approximations for many-electron systems. *Phys. Rev. B*, 23(10):5048–5079, 1981.

[80] E. S. Jochen, H.and Gustavo and E. Matthias. Hybrid functionals based on a screened coulomb potential. *J. Chem. Phys.*, 118(18):8207, 2003.

[81] H. J. Monkhorst and J. D. Pack. Special points for Brillouin-zone integrations. *Phys. Rev. B*, 13(12):5188–5192, 1976.

[82] K. Watanabe, T. Taniguchi, and H. Kanda. Direct-bandgap properties and evidence for ultraviolet lasing of hexagonal boron nitride single crystal. *Nature Mater.*, 3(6):404–409, 2004.

[83] C. Ataca and S. Ciraci. Functionalization of single-layer MoS_2 honeycomb structures. *J. Phys. Chem. C*, 115(27):13303–13311, 2011.

[84] R. J. Archer, R. Y. Koyama, E. E. Loebner, and R. C. Lucas. Optical absorption, electroluminescence, and the band gap of BP. *Phys. Rev. Lett.*, 12(19):538–540, 1964.

[85] G. L. W. Hart and A. Zunger. Electronic structure of BAs and boride III-V alloys. *Phys. Rev. B*, 62(20):13522–13537, 2000.

[86] K. F. Mak, C. Lee, J. Hone, J. Shan, and T. F. Heinz. Atomically thin MoS_2: A new direct-gap semiconductor. *Phys. Rev. Lett.*, 105(13):136805, 2010.

[87] R. Saito, M. S. Dresselhaus, and G. Dresselhaus. *Physical Properties of Carbon Nanotubes*. World Scientific Publishing Company, 1998.

[88] L. Pauling. *The nature of the chemical bond and the structure of molecules and crystals*. Cornell University Press, 1960.

[89] W. Tang, E. Sanville, and G. Henkelman. A grid-based bader analysis algorithm without lattice bias. *J. Phys.: Condens. Matter*, 21(8):084204, 2009.

[90] M. Peressi, N. Binggeli, and A. Baldereschi. Band engineering at interfaces: theory and numerical experiments. *J. Phys. D: Appl. Phys.*, 31(11):1273–1299, 1998.

[91] P. W. Sutter, J.-I. Flege, and E. A. Sutter. Epitaxial graphene on ruthenium. *Nature Mater.*, 7(5):406–411, 2008.

[92] C. L. Freeman, F. Claeyssens, N. L. Allan, and J. H. Harding. Graphitic nanofilms as precursors to wurtzite films: theory. *Phys. Rev. Lett.*, 96(6):066102, 2006.

[93] D. Wu, M. G. Lagally, and F. Liu. Stabilizing graphitic thin films of wurtzite materials by epitaxial strain. *Phys. Rev. Lett.*, 107(23):236101, 2011.

[94] S. S. Lin. Light-emitting two-dimensional ultrathin silicon carbide. *J. Phys. Chem. C*, 116(6):3951–3955, 2012.

[95] C. Jin, F. Lin, K. Suenaga, and S. Iijima. Fabrication of a freestanding boron nitride single layer and its defect assignments. *Phys. Rev. Lett.*, 102(19):195505, 2009.

[96] H. Şahin, S. Cahangirov, M. Topsakal, E. Bekaroglu, E. Akturk, R. T. Senger, and S. Ciraci. Monolayer honeycomb structures of group-IV elements and III-V binary compounds: First-principles calculations. *Phys. Rev. B*, 80(15):155453, 2009.

[97] J. Heyd, J. E. Peralta, G. E. Scuseria, and R. L. Martin. Energy band gaps and lattice parameters evaluated with the Heyd-Scuseria-Ernzerhof screened hybrid functional. *J. Chem. Phys.*, 123(17):174101, 2005.

[98] L. Hedin. New method for calculating the one-particle Green's function with application to the electron-gas problem. *Phys. Rev.*, 139(3A):A796–A823, 1965.

[99] W. G. Aulbur, L. Jönsson, and J. W. Wilkins. Quasiparticle calculations in solids. *Solid State Physics*, 54:1–218, 1999.

[100] G. Bergerhoff and I. D. Brown. Inorganic crystal structure database. In *Crystallographic Databases*. International Union of Crystallography, Chester, 1987.

[101] M. Gajdoš, K. Hummer, G. Kresse, J. Furthmüller, and F. Bechstedt. Linear optical properties in the projector-augmented wave methodology. *Phys. Rev. B*, 73(4):045112, 2006.

[102] G. Grosso and G. P. Parravicini. *Solid State Physics*. Academic, San Diego, 2000.

[103] E. V. Anslyn and D. A. Dougherty. *Modern Physical Organic Chemistry*. University Science Books, Sausalito, California, 2006.

[104] S. Nosé. A unified formulation of the constant temperature molecular dynamics methods. *J. Chem. Phys.*, 81(1):511–519, 1984.

[105] O. Madelung. *Semiconductors: Data Handbook*. Springer, 2004.

[106] H. Yamashita, K. Fukui, S. Misawa, and S. Yoshida. Optical properties of AlN epitaxial thin films in the vacuum ultraviolet region. *J. Appl. Phys.*, 50(2):896–898, 1979.

[107] R. N. Dexter, Benjamin Lax, A. F. Kip, and G. Dresselhaus. Effective masses of electrons in silicon. *Phys. Rev.*, 96(1):222–223, 1954.

[108] S. Tongay, J. Zhou, C. Ataca, K. Lo, T. S. Matthews, J. Li, J. C. Grossman, and J. Wu. Thermally driven crossover from indirect toward direct bandgap in 2D semiconductors: $MoSe_2$ versus MoS_2. *Nano Letter.*, 12(11):5576–5580, 2012.

[109] Z. C. Tu and X. Hu. Elasticity and piezoelectricity of zinc oxide crystals, single layers, and possible single-walled nanotubes. *Phys. Rev. B*, 74(3):035434, 2006.

[110] M. Grätzel. Photoelectrochemical cells. *Nature*, 414(6861):338–344, 2001.

[111] M. Lei, J. H. Yum, J. Price, T. W. Hudnall, C. W. Bielawski, S. K. Banerjee, P. S. Lysaght, G. Bersuker, and M. C. Downer. Spectroscopic evaluation of band alignment of atomic layer deposited BeO on Si(100). *Appl. Phys. Lett.*, 100(12):122906, 2012.

[112] A. Wang, J. R. Babcock, N. L. Edleman, A. W. Metz, M. A. Lane, R. Asahi, V. P. Dravid, C. R. Kannewurf, A. J. Freeman, and T. J. Marks. Indium-cadmium-oxide films having exceptional electrical conductivity and optical transparency: clues for optimizing transparent conductors. *Proc. Natl. Acad. Sci.*, 98(13):7113–7116, 2001.

[113] G. Choudhary, V. Raykar, S. Tiwari, A. Dashora, and B. L. Ahuja. Electronic structure and compton profiles of CdO and HgO. *physica status solidi (b)*, 248(1):212–219, 2011.

[114] P. H. Jefferson, S. A. Hatfield, T. D. Veal, P. D. C. King, C. F. McConville, J. Zú nigaPérez, and V. Mu nozSanjosé. Bandgap and effective mass of epitaxial cadmium oxide. *Appl. Phys. Lett.*, 92(2):022101, 2008.

[115] B. Rakshit and P. Mahadevan. Stability of the bulk phase of layered zno. *Phys. Rev. Lett.*, 107(8):085508, 2011.

[116] Z. C. Tu. First-principles study on physical properties of a single

ZnO monolayer with graphene-like structure. *J. Comput. Theor. Nanos.*, 7(6):1182–1186, 2010.

[117] A. Togo, F. Oba, and I. Tanaka. First-principles calculations of the ferroelastic transition between rutile-type and $CaCl_2$-type SiO_2 at high pressures. *Phys. Rev. B*, 78(13):134106, 2008.

[118] A. Bosak, M. Krisch, M. Mohr, J. Maultzsch, and C. Thomsen. Elasticity of single-crystalline graphite: Inelastic x-ray scattering study. *Phys. Rev. B*, 75(15):153408, 2007.

[119] Q. Peng, A. R. Zamiri, W. Ji, and S. De. Elastic properties of hybrid graphene/boron nitride monolayer. *Acta Mech.*, 223(12):2591–2596, 2012.

[120] J. Klimeš, D. R. Bowler, and A. Michaelides. Van der waals density functionals applied to solids. *Phys. Rev. B*, 83(19):195131, 2011.

[121] D. Sánchez-Portal, E. Artacho, J. M. Soler, A. Rubio, and P. Ordejón. *Ab initio* structural, elastic, and vibrational properties of carbon nanotubes. *Phys. Rev. B*, 59(19):12678–12688, 1999.

[122] D. Sánchez-Portal and E. Hernández. Vibrational properties of single-wall nanotubes and monolayers of hexagonal BN. *Phys. Rev. B*, 66(23):235415, 2002.

[123] L. Yang, J. Deslippe, C.-H. Park, M. L. Cohen, and S. G. Louie. Excitonic effects on the optical response of graphene and bilayer graphene. *Phys. Rev. Lett.*, 103(18):186802, 2009.

[124] R. R. Nair, P. Blake, A. N. Grigorenko, K. S. Novoselov, T. J. Booth, T. Stauber, N. M. R. Peres, and A. K. Geim. Fine structure constant defines visual transparency of graphene. *Science*, 320(5881):1308, 2008.

[125] L. Britnell, R. V. Gorbachev, R. Jalil, B. D. Belle, F. Schedin, M. I. Katsnelson, L. Eaves, S. V. Morozov, A. S. Mayorov, N. M. R. Peres, A. H. Castro Neto, J. Leist, Geim A. K., L. A. Ponomarenko, and Novoselov K. S. Electron tunneling through ultrathin boron nitride crystalline barriers. *Nano Letter.*, 12(3):1707–1710, 2012.

[126] C. G. Van de Walle and J. Neugebauer. First-principles calculations for defects and impurities: Applications to III-nitrides. *J. Appl. Phys.*, 95(8):3851–3879, 2004.

[127] A. Aruchamy. *Photoelectrochemistry and Photovoltaics of Layered Semiconductors*. Springer, New York, 1992.

[128] J. Martinez-Pastor, A. Segura, J. L. Valdes, and A. Chevy. Electrical and photovoltaic properties of indium-tin-oxide/*p*-InSe/Au solar cells. *J. Appl. Phys.*, 62(4):1477–1483, 1987.

[129] P. Hu, L. Wang, M. Yoon, J. Zhang, W. Feng, X. Wang, Z. Wen, J. C. Idrobo, Y. Miyamoto, D. B. Geohegan, and K. Xiao. Highly responsive ultrathin gas nanosheet photodetectors on rigid and flexible substrates. *Nano Letter.*, 13(4):1649–1654, 2013.

[130] P. Hu, Z. Wen, L. Wang, P. Tan, and K. Xiao. Synthesis of few-layer gase nanosheets for high performance photodetectors. *ACS Nano*, 6(7):5988–5994, 2012.

[131] D. J. Late, B. Liu, H. S. S. R. Matte, C. N. R. Rao, and V. P. Dravid. Rapid characterization of ultrathin layers of chalcogenides on SiO_2/Si substrates. *Adv. Funct. Mater.*, 22(9):1894–1905, 2012.

[132] A. Splendiani, L. Sun, Y. Zhang, T. Li, J. Kim, C.-Y. Chim, G. Galli, and F. Wang. Emerging photoluminescence in monolayer MoS_2. *Nano Letter.*, 10(4):1271–1275, 2010.

[133] J. Feng, X.H. Qian, C.-W. Huang, and J. Li. Strain-engineered artificial atom as a broad-spectrum solar energy funnel. *Nature Photonics*, 6(12):866–872, 2012.

[134] A. Kudo and Y. Miseki. Heterogeneous photocatalyst materials for water splitting. *Chem. Soc. Rev.*, 38(1):253–278, 2009.

[135] S. Chen and L.-W. Wang. Thermodynamic oxidation and reduction potentials of photocatalytic semiconductors in aqueous solution. *Chem. Mater.*, 24(18):3659–3666, 2012.

[136] M. C. Toroker, D. K. Kanan, N. Alidoust, L. Y. Isseroff, P. Liao, and E. A. Carter. First principles scheme to evaluate band edge positions in potential transition metal oxide photocatalysts and photoelectrodes. *Phys. Chem. Chem. Phys.*, 13(37):16644–16654, 2011.

[137] V. Chakrapani, J. C. Angus, A. B. Anderson, S. D. Wolter, B. R. Stoner, and G. U. Sumanasekera. Charge transfer equilibria between diamond and an

aqueous oxygen electrochemical redox couple. *Science*, 318(5855):1424–1430, 2007.

[138] A. J. Nozik. Photoelectrochemistry: Applications to solar energy conversion. *Ann. Rev. Phys. Chem.*, 29(1):189–222, 1978.

[139] W. Jaegermann and H. Tributsch. Interfacial properties of semiconducting transition metal chalcogenides. *Prog. Surf. Sci.*, 29(1-2):1–167, 1988.

[140] L. Matthes, P. Gori, O. Pulci, and F. Bechstedt. Universal infrared absorbance of two-dimensional honeycomb group-IV crystals. *Phys. Rev. B*, 87(3):035438, 2013.

[141] T. Köhler, T. Frauenheim, Z. Hajnal, and G. Seifert. Tubular structures of gas. *Phys. Rev. B*, 69(19):193403, 2004.

[142] R. G. Hennig, A. Wadehra, K. P. Driver, W. D. Parker, C. J. Umrigar, and J. W. Wilkins. Phase transformation in Si from semiconducting diamond to metallic β-Sn phase in QMC and DFT under hydrostatic and anisotropic stress. *Phys. Rev. B*, 82(1):014101, 2010.

[143] J. Kang, S. Tongay, J. Zhou, J. Li, and J. Wu. Band offsets and heterostructures of two-dimensional semiconductors. *Appl. Phys. Lett.*, 102(1):012111, 2013.

[144] J. A. Wilson and A. D. Yoffe. The transition metal dichalcogenides discussion and interpretation of the observed optical, electrical and structural properties. *Adv. Phys.*, 18(73):193–335, 1969.

[145] W. A. Harrison. *Electronic Structure and the Properties of Solids: The Physics of the Chemical Bond*. Dover Publications, New York, 1989.

[146] J. P. Perdew. Density functional theory and the band gap problem. *Int. J. Quant. Chem.*, 30(3):451–451, 1986.

[147] K. E. Jason, J. L. Melissa, and E. S. Gustavo. The indirect to direct band gap transition in multilayered MoS_2 as predicted by screened hybrid density functional theory. *Appl. Phys. Lett.*, 99(26):261908, 2011.

[148] R. Asahi, T. Morikawa, T. Ohwaki, K. Aoki, and Y. Taga. Visible-light photocatalysis in nitrogen-doped titanium oxides. *Science*, 293(5528):269–271, 2001.

[149] R. van de Krol, Y. Liang, and J. Schoonman. Solar hydrogen production with nanostructured metal oxides. *J. Mater. Chem.*, 18(20):2311–2320, 2008.

[150] D. P. Lide, editor. *CRC Handbook of Chemistry and Physics*. CRC PRESS, 93rd edition, 2012.

[151] W. E. Dasent, editor. *Inorganic Energetics: An Introduction*. Cambridge University Press, 2nd edition, 1982.

[152] W. Earle Waghorne. Solubilities of the silver halides in aqueous mixtures of methanol, acetonitrile, and dimethylsulfoxide. *Monatshefte für Chemie / Chemical Monthly*, 134(5):655–667, 2003.

[153] S. Ghatak, A. N. Pal, and A. Ghosh. Nature of electronic states in atomically thin MoS_2 field-effect transistors. *ACS Nano*, 5(10):7707–7712, 2011.

[154] N. Singh, G. Jabbour, and U. Schwingenschlögl. Optical and photocatalytic properties of two-dimensional MoS_2. *Eur. Phys. J. B*, 85(11):392, 2012.

[155] M. G. Walter, E. L. Warren, J. R. McKone, S. W. Boettcher, Q. Mi, E. A. Santori, and N. S. Lewis. Solar water splitting cells. *Chem. Rev.*, 110(11):6446–6473, 2010.

[156] D. Feller. The role of databases in support of computational chemistry calculations. *J. Comp. Chem.*, 17(13):1571–1586, 1996.

[157] K. L. Schuchardt, B. T. Didier, T. Elsethagen, L. Sun, V. Gurumoorthi, J. Chase, J. Li, and T. L. Windus. Basis set exchange: A community database for computational sciences. *J. Chem. Inf. Model.*, 47(3):1045–1052, 2007.

[158] A. V. Marenich, C. J. Cramer, and D. G. Truhlar. Universal solvation model based on solute electron density and on a continuum model of the solvent defined by the bulk dielectric constant and atomic surface tensions. *J. Phys. Chem. B*, 113(18):6378–6396, 2009.

[159] G. Eda, T. Fujita, H. Yamaguchi, D. Voiry, M. Chen, and M. Chhowalla. Coherent atomic and electronic heterostructures of single-layer MoS_2. *ACS Nano*, 6(8):7311–7317, 2012.

[160] H. Shi, H. Pan, Y.-W. Zhang, and B. I. Yakobson. Quasiparticle band struc-

tures and optical properties of strained monolayer MoS_2 and WS_2. *Phys. Rev. B*, 87(15):155304, 2013.

[161] G. Y. Guo and W. Y. Liang. The electronic structures of platinum dichalcogenides: PtS_2 , $PtSe_2$ and $PtTe_2$. *J. Phys. C*, 19(7):995–1008, 1986.

[162] J. Heyd, G. E. Scuseria, and M. Ernzerhof. Erratum: "hybrid functionals based on a screened coulomb potential" [J. Chem. Phys. **118**, 8207 (2003)]. *J Chem. Phys.*, 124(21):219906, 2006.

[163] K. J. Laidler, J. H. Meiser, and B. C. Sanctuary, editors. *Physical Chemistry*. Cengage Learning, 4th edition, 2002.

[164] T. Bak, J. Nowotny, M. Rekas, and C. C. Sorrell. Photo-electrochemical hydrogen generation from water using solar energy. materials-related aspects. *Int. J. Hydrogen Energy*, 27(10):991–1022, 2002.

[165] J. M. Ziman. *Principles of the Theory of Solids*. Cambridge University Press, Cambridge, 1979.

[166] F. A. S. Al-Alamy, A. A. Balchin, and M. White. The expansivities and the thermal degradation of some layer compounds. *J. Mater. Sci.*, 12(10):2037–2042, 1977.

[167] A. J. Smith, P. E. Meek, and W. Y. Liang. Raman scattering studies of SnS_2 and $SnSe_2$. *J. Phys. C*, 10(8):1321, 1977.

[168] R. van de Krol and M. Gratzel. *Photoelectrochemical Hydrogen Production*. Springer, 2012.

[169] Y. Bertrand, G. Leveque, J. Robin, and R. Mamy. Optical transitions from d core levels in tin dichalcogenides. *Physica B+C*, 99:287–290, 1980.

[170] T. Cheiwchanchamnangij and W. R. L. Lambrecht. Quasiparticle band structure calculation of monolayer, bilayer, and bulk MoS_2. *Phys. Rev. B*, 85(20):205302, 2012.

[171] A. Sihvola. *Electromagnetic Mixing Formulae and Applications*. The Institution of Engineering and Technology, 2000.

[172] H. Jiang. Electronic band structures of molybdenum and tungsten

dichalcogenides by the GW approach. *J. Phys. Chem. C*, 116(14):7664–7671, 2012.

[173] J. J. Liu, X. L. Fu, S. F. Chen, and Y. F. Zhu. Electronic structure and optical properties of Ag_3PO_4 photocatalyst calculated by hybrid density functional method. *Appl. Phys. Lett.*, 99(19):191903, 2011.

[174] A. H. Nethercot. Prediction of Fermi energies and photoelectric thresholds based on electronegativity concepts. *Phys. Rev. Lett.*, 33(18):1088–1091, 1974.

[175] S. S. Kocha and J. A. Turner. Displacement of the band edges of $GaInP_2$ in aqueous electrolytes induced by surface modification. *J. Electrochem. Soc.*, 142(8):2625–2630, 1995.

[176] M. A. Lukowski, A. S. Daniel, F. Meng, A. Forticaux, L. Li, and S. Jin. Enhanced hydrogen evolution catalysis from chemically exfoliated metallic MoS_2 nanosheets. *J. .Am. Chem. Soc.*, 135(28):10274–10277, 2013.

[177] J. A. Wilson, F. J. Di Salvo, and S. Mahajan. Charge-density waves in metallic, layered, transition-metal dichalcogenides. *Phys. Rev. Lett.*, 32:882–885, 1974.

[178] C. Si, W. Duan, Z. Liu, and F. Liu. Electronic strengthening of graphene by charge doping. *Phys. Rev. Lett.*, 109(22):226802, 2012.

[179] P. Ruiz-Diaz, T. R. Dasa, and V. S. Stepanyuk. Tuning magnetic anisotropy in metallic multilayers by surface charging: An *ab initio* study. *Phys. Rev. Lett.*, 110(26):267203, 2013.

[180] A. K. Geim and Grigorieva I. V. Van der Waals heterostructure. *Nature*, 499(7459):419–425, 2013.

[181] G. Mills, H. Jonsson, and G. K. Schenter. Reversible work transition state theory: application to dissociative adsorption of hydrogen. *Surf. Sci.*, 324(23):305 – 337, 1995.

[182] B. J. Berne, D. F. Coker, and G. Cicotti. *Classical and Quantum Dynamics in Condensed Phase Simulations*. World Scientific Publishing Company, 1998.

[183] D. Voiry, H. Yamaguchi, J. Li, R. Silva, D. C. B. Alves, T. Fujita, M. Chen, T. Asefa, V. B. Shenoy, G. Eda, and M. Chhowalla. Enhanced catalytic

activity in strained chemically exfoliated WS_2 nanosheets for hydrogen evolution. *Nature Mater.*, 12(9):850–855, 2013.

[184] R. G. Hennig, D. R. Trinkle, J. Bouchet, S. G. Srinivasan, R. C. Albers, and J. W. Wilkins. Impurities block the α to ω martensitic transformation in titanium. *Nature Mater.*, 4(2):129–133, 2005.

[185] A. N. Enyashin, L. Yadgarov, L. Houben, I. Popov, M. Weidenbach, R. Tenne, M. Bar-Sadan, and G. Seifert. New route for stabilization of 1T-WS_2 and MoS_2 phases. *J. Phys. Chem. C*, 115(50):24586–24591, 2011.

[186] Y.-C. Lin, M. O. Dumcenco, Y.-S. Huang, and K. Suenaga. Atomic mechanism of phase transition between metallic and semiconducting MoS_2 single-layers. *arXiv:1310.2363*, 2013.

[187] E. Canadell and M. H. Whangbo. Conceptual aspects of structure-property correlations and electronic instabilities, with applications to low-dimensional transition-metal oxides. *Chem. Rev.*, 91(5):965–1034, 1991.

[188] M. H. Whangbo and E. Canadell. Analogies between the concepts of molecular chemistry and solid-state physics concerning structural instabilities. electronic origin of the structural modulations in layered transition metal dichalcogenides. *J. Am. Chem. Soc.*, 114(24):9587–9600, 1992.

[189] J. Heising and M. G. Kanatzidis. Structure of restacked MoS_2 and WS_2 elucidated by electron crystallography. *J. Am. Chem. Soc.*, 121(4):638–643, 1999.

[190] D. Yang, S. Jiménez Sandoval, W. M. R. Divigalpitiya, J. C. Irwin, and R. F. Frindt. Structure of single-molecular-layer MoS_2. *Phys. Rev. B*, 43(14):12053–12056, 1991.

[191] F. Wypych, T. Weber, and R. Prins. Scanning tunneling microscopic investigation of 1T-MoS_2. *Chem. Mater.*, 10(3):723–727, 1998.

[192] F. Wypych and R. Schollhorn. 1T-MoS_2, a new metallic modification of molybdenum disulfide. *J. Chem. Soc. Chem. Commun.*, 19:1386–1388, 1992.

[193] H. T. Stokes and D. M. Hatch. *FINDSYM*: program for identifying the space-group symmetry of a crystal. *J. Appl. Crystallography*, 38(1):237–238, 2005.

[194] A. Ramasubramaniam. Large excitonic effects in monolayers of molybdenum and tungsten dichalcogenides. *Phys. Rev. B*, 86(11):115409, 2012.

[195] Z. F. Wang, Z Liu, and F. Liu. Organic topological insulators in organometallic lattices. *Nature Commun.*, 4:1471, 2013.

[196] M. D. Johannes and I. I. Mazin. Fermi surface nesting and the origin of charge density waves in metals. *Phys. Rev. B*, 77(16):165135, 2008.

[197] D. Lamago, M. Hoesch, M. Krisch, R. Heid, K.-P. Bohnen, P. Boni, and D. Reznik. Measurement of strong phonon softening in Cr with and without fermi-surface nesting by inelastic x-ray scattering. *Phys. Rev. B*, 82(19):195121, 2010.

[198] X. Zou, Y. Liu, and B. I. Yakobson. Predicting dislocations and grain boundaries in two-dimensional metal-disulfides from the first principles. *Nano Letter.*, 13(1):253–258, 2013.

[199] F. Fuchs, J. Furthmüller, F. Bechstedt, M. Shishkin, and G. Kresse. Quasiparticle band structure based on a generalized Kohn-Sham scheme. *Phys. Rev. B*, 76(11):115109, 2007.

[200] P. Villars, H. Okamoto, and K. Cenzual. A-B-C phase diagram. In *ASM Alloy Phase Diagram Center*. ASM International, Materials Park, Ohio, 2006.

[201] A. Lafond, C. Deudon, and A. Meerschaut. X-ray structure determination and magnetic properties of a new misfit layered compound: yttrium chromium sulfide; $(Y_{0.93}[\,]_{0.07}S)_{1.28}CrS_2$. *Eur. J. Solid State Inorg. Chem.*, 1994.

[202] Y. Qi and L. G. Hector. Planar stacking effect on elastic stability of hexagonal boron nitride. *Appl. Phys. Lett.*, 90(8):081922, 2007.

[203] T. Cao, G. Wang, W. Han, H. Ye, C. Zhu, J. Shi, Q. Niu, P. Tan, E. Wang, B. Liu, and J. Feng. Valley-selective circular dichroism of monolayer molybdenum disulphide. *Nature Commun.*, 3:887, 2012.

[204] W. Yao, D. Xiao, and Q. Niu. Valley-dependent optoelectronics from inversion symmetry breaking. *Phys. Rev. B*, 77(23):235406, 2008.

[205] W. Shockley and H. J. Queisser. Detailed balance limit of efficiency of *p-n* junction solar cells. *J. Appl. Phys.*, 32(3):510–519, 1961.

[206] M. Bernardi, M. Palummo, and J. C. Grossman. Extraordinary sunlight absorption and one nanometer thick photovoltaics using two-dimensional monolayer materials. *Nano Letters*, 13(8):3664–3670, 2013.

[207] R. D. King-Smith and D. Vanderbilt. Theory of polarization of crystalline solids. *Phys. Rev. B*, 47(3):1651–1654, 1993.

[208] W. W. Tipton, C. R. Bealing, K. Mathew, and R. G. Hennig. Structures, phase stabilities, and electrical potentials of Li-Si battery anode materials. *Phys. Rev. B*, 87(18):184114, 2013.

[209] M. Topsakal, S. Cahangirov, E. Bekaroglu, and S. Ciraci. First-principles study of zinc oxide honeycomb structures. *Phys. Rev. B*, 80(23):235119, 2009.